Title	Phase estimation receiver for full-field detection: a novel receiver structure for electronic dispersion compensation of metropolitan area networks
Authors	McCarthy, Mary E.
Publication date	2009-10
Original Citation	McCarthy, M. E. 2009. Phase estimation receiver for full-field detection: a novel receiver structure for electronic dispersion compensation of metropolitan area networks. PhD Thesis, University College Cork.
Type of publication	Doctoral thesis
Link to publisher's version	http://library.ucc.ie/record=b1998527~S0
Rights	© 2009, Mary E. McCarthy - http://creativecommons.org/licenses/by-nc-nd/3.0/
Download date	2024-05-08 00:18:43
Item downloaded from	https://hdl.handle.net/10468/831

PHASE ESTIMATION RECEIVER FOR FULL-FIELD DETECTION:
A NOVEL RECEIVER STRUCTURE FOR ELECTRONIC DISPERSION COMPENSATION OF METROPOLITAN AREA NETWORKS

by

Mary Elizabeth McCarthy

A thesis submitted to University College Cork
for the degree of Doctor of Philosophy

Tyndall National Institute
Department of Physics

October 2009

Research Supervisor: Dr Andrew D. Ellis

Head of Department: Prof John McInerney

UCC
Coláiste na hOllscoile Corcaigh, Éire
University College Cork, Ireland

Abstract

The development of ultra high speed (~20 Gsamples/s) analogue to digital converters (ADCs), and the delayed deployment of 40 Gbit/s transmission due to the economic downturn, has stimulated the investigation of digital signal processing (DSP) techniques for compensation of optical transmission impairments. In the future, DSP will offer an entire suite of tools to compensate for optical impairments and facilitate the use of advanced modulation formats. Chromatic dispersion is a very significant impairment for high speed optical transmission. This thesis investigates a novel electronic method of dispersion compensation which allows for cost-effective accurate detection of the amplitude and phase of the optical field into the radio frequency domain. The first electronic dispersion compensation (EDC) schemes accessed only the amplitude information using square law detection and achieved an increase in transmission distances. This thesis presents a method by using a frequency sensitive filter to estimate the phase of the received optical field and, in conjunction with the amplitude information, the entire field can be digitised using ADCs. This allows DSP technologies to take the next step in optical communications without requiring complex coherent detection. This is of particular of interest in metropolitan area networks. The full-field receiver investigated requires only an additional asymmetrical Mach-Zehnder interferometer and balanced photodiode to achieve a 50% increase in EDC reach compared to amplitude only detection.

Statement of Originality

Except where indicated in the acknowledgements section or by references, all the work presented in this thesis is solely attributed to the author. The author planned and participated in the design and implementation of all experiments except where explicitly indicated. Precise details of collaborators may be ascertained from the lists of co-authors in Appendix A.

I   Table of contents

II   Acknowledgements

No person or no work is the product of one person alone so I would like to thank all those who have influenced and helped me through PhD work and getting me through it. I would like to thank Dr Andrew Ellis, my supervisor, who has provided me with excellent teaching and has made me into a competent and confident experimentalist. To Dr Fatima Gunning thank you for explaining how physicists think and to Dr Rod Webb who had the unfortunate job of proof reading many of my papers. And many thanks to other founding members of the Photonic Systems Group, Prof. David Cotter, Prof. Paul Townsend and Dr. Bob Manning for providing an exception working environment and much encouragement. A special thanks to Dr. Jian Zhao who works tirelessly on this project, helped give it direction and extend my understanding of the optical simulation practices. Also, I would like to extend my gratitude to Science Foundation Ireland through whose funding this work was supported.

A warm thanks to Dr. Paul Gunning for helping with the BT fibre access and explaining how awful writing a thesis is. I'd also like to gratefully acknowledge the support of BT Ireland, particularly John Coleman, Mark Conroy, William McAuliffe, Richie O'Regan and Mark O'Reilly, in providing access to the Cork-Clonakilty optical fibre link used for some of the experimental work. It has been of immense benefit to me in allowing me to conduct many experiments I would not have otherwise been able to.

I would like to thank my friends for my sanity – to Eimear, Tadhg and Robin as the old airport crew, especially to Tadhg for the long lunches when everything was going

III   List of Abbreviations

AC	Alternating Current
ADC	Analogue-Digital Converter
AM	Amplitude Modulation
AMZI	Asymmetric Mach Zehnder Interferometer
AOM	Acousto-optic Modulator
APC	Angled Polished Connector
ASE	Amplified Spontaneous Emission
ASIC	Application Specific Integrated Circuit
ATD	Adaptive Threshold Detection
AWG	Arrayed Waveguide Grating
AWGN	Additive White Gaussian Noise
BER	Bit Error Rate
BERT	Bit Error Rate Test set
BT	British Telecom
CIP	Centre for Integrated Photonics
CML	Chirp Managed Laser
CW	Continuous Wave
DAC	Digital-Analogue Converter
DC	Direct Current
DCF	Dispersion Compensating Fibre
DCM	Dispersion Compensating Module
DD-MLSE	Direct Detection MLSE
DFB	Distributed Feed-back Laser
DFF	D-Flip Flop
DGE	Dynamic Gain Equaliser
DPSK	Differential Phase Shift Keying
DSP	Digital Signal Processing
DST	Dispersion Supported Transmission
DTD	Differential Time Delay
EAM	Electro-Absorption Modulator
EDC	Electronic Dispersion Compensation
EDFA	Erbium Doped Fibre Amplifier
EF	Electrical Filter
FC	Ferrule Connector
FD	Field Detection MLSE
FEC	Forward Error Correction
FFT	Fast Fourier Transform
FIR	Finite Impulse Response
FSR	Free Spectral Range
FWM	Four Wave Mixing
GVD	Group Velocity Dispersion
IFFT	Inverse Fourier Transform

IIR	Infinite Impulse Response
LASER	Light amplification by stimulated emission of radiation
LO	Local Oscillator
MAN	Metropolitan Area Network
MLSE	Maximum Likelihood Sequence Estimation
MSSI	Mid Span Spectral Inversion
MZM	Mach-Zehnder Modulator
NEL	NTT Electronics Corporation
NEP	Normalized Error Probability
NRZ	Non-Return to Zero
OBPF	Optical Band Pass Filter
OFDM	Optical Frequency Division Multiplexing
OOK	On-Off Keying
OPC	Optical Phase Conjugation
OSNR	Optical Signal to Noise Ratio
OTDR	Optical Time Domain Reflectometer
PC	Personal Computer
PMD	Polarisation Mode Dispersion
POL	Polarisation Scrambler
PRBS	Pseudo Random Bit Sequence
RF	Radio Frequency
SC	Subscriber Connector
(S)SMF	(Standard) Single Mode Fibre
SOA	Semiconductor Optical Amplifier
SPM	Self Phase Modulation
ULL	Ultra Low Loss Fibre
VOA	Variable Optical Attenuator
VPI	Virtual Photonics Incorporated
WDM	Wavelength Division Multiplexing
XR	Extinction Ratio

1 Motivation and State of the Art

1.1 Historical Perspective

Optical communication has come a long way since fibre was first proposed as a medium for confined light propagation with reasonable loss ~20 dB/km [1-2]. It offers high bandwidth, low loss and increased reach compared to telegraph or coaxial systems. This has led to the development of a large research area in optical components and photonic networks. Optical fibre has become a widely accepted technology for high speed networks for internet and telephony.

From the development of the ruby laser in the 1950's [3], there have been a number of salient advancements which have made photonics systems the work horse of the high-speed, long reach telecommunications industry. The first important change was moving from 0.8 μm to 1.3 μm transmission wavelength in the 1970's to combat fibre loss [4]. The development of single mode fibres in 1981 resulted in a major increase in allowable bandwidth by reducing the effect of dispersion facilitated 2 Gbit/s transmission [5]. The transmission was still loss-limited to repeater spacings of ~100 km even when the transmission wavelength was moved to 1.55 μm where fibre loss is at a minimum. In order to extend this reach, more sensitive receivers were investigated using coherent detection [6]. These were overtaken by the development of optical amplification technology [7] and this, coupled with the advent of broadband optical components with low loss, paved the way for practical wavelength division multiplexed systems (WDM) [8]. This led to a rapid increase in the bandwidth capacity per fibre and these systems have been widely installed. To extend

the range of wavelengths that can be used and also to increase the total amplification per span, Raman amplification [9] has become increasingly used in dense long-haul WDM. Due to its wideband nature it can be used to extend optical communications into the short *'S'* and long *'L'* wavelength bands around the *'C'* band (1.53-1.57 μm). There has also been a drive to increase the bitrate per channel from 2.5 Gbit/s as the commercial norm in 1990.

40 Gbit/s systems are commercially available today and there is a significant research effort to move to 100G Ethernet. The widespread installation of 40 Gbit/s systems was delayed by the bursting of the "dot com" bubble in 2002. This has allowed for a complimentary technology to develop due to available electronics gaining pace on 10 Gbit/s systems. This allowed for years of research in digital signal processing to be applied as appropriate to optical networks. The first useful technology which was employed successfully and allows for extended reach and dramatic relaxation of required link performance is forward error correction coding (Section 1.3). This allows for bit error rates up to 10^{-2} to be corrected up to 10^{-16}. A further extension of this has been the development of electronic dispersion compensation technology. This was first proposed in 1990 [10] and revived in 2000 [11-12] has gained pace as a research interest since pioneering work in 2005 [13-20].

1.2 Metropolitan Area Networks

Modern networks are generally subdivided into three areas which differ in terms of the number of users that the resources will be shared by and, consequently, by how cost sensitive they are. A schematic diagram in shown in Figure 1 illustrates each network type.

- Core networks connect major population centres and countries. They are

12

shared by many millions of users and travel long distances and hence, high speed, complex, high performance technologies can be justified on these links.

- Access networks are the other end of the scale. These are the networks to the home or small business. These are generally short, <100 km, and are extremely cost sensitive. These are run at a lower bit rate than metropolitan or core networks and usually inherit tried and tested technology as it becomes cheaper to implement.

- Metropolitan Area Networks (MAN) are usually within a city or major population centre. They are often switched ring or mesh networks. MANs connect Core and Access networks. Technology used in MANs is shared by more users than in an Access network but less than a Core network, so fiscal constraints are still extremely tight. They have a reach which is beyond the dispersion limit so compensation is required. Also MANs must be quickly adaptable to enable dynamic bandwidth allocation or repair faults. This leads to the need to consider redundant paths which makes the reach indeterminate *a priori*.

In Figure 1, two metro ports are labelled. The figure illustrates how different pulses may be transmitted (Port A) along different paths to the same receiver node (Port B). These will result in the pulses undergoing different dispersions and losses. This is shown schematically by the different coloured pulses. The general length of metropolitan links is 40-100 km and a typical MAN consists of 4-7 nodes. In this thesis, the aim is to develop a electronic dispersion compensation of reasonable cost with a reach suitable for metropolitan networks.
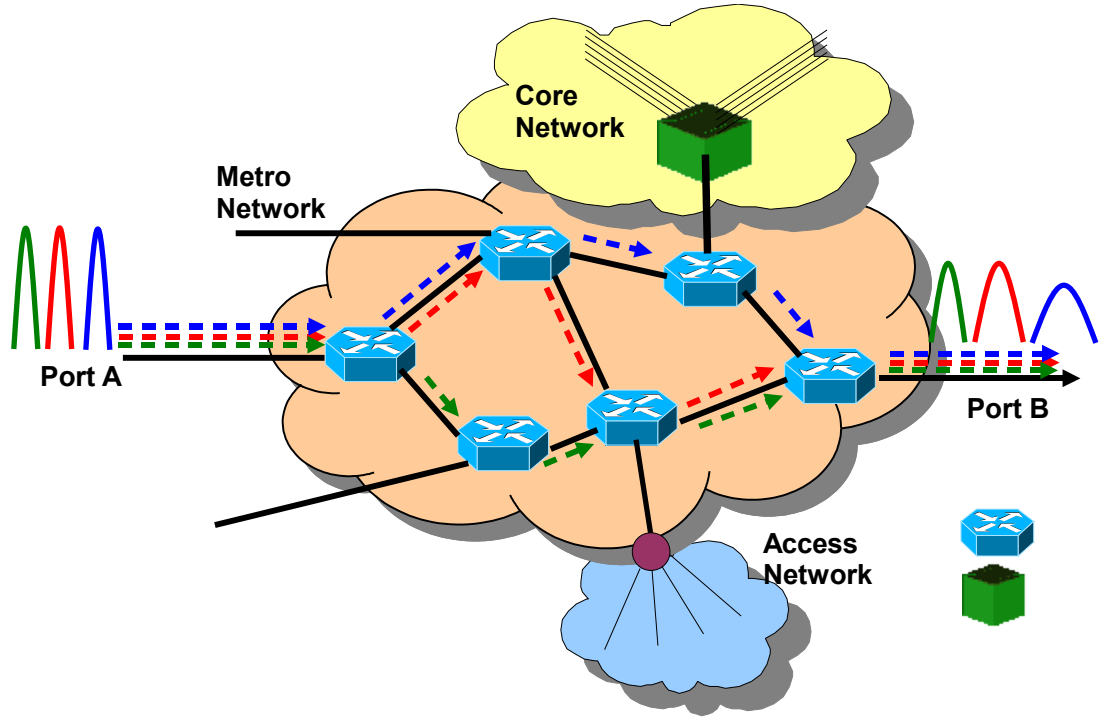
Figure 1: Schematic representation of a metropolitan area network.

1.3 Forward Error Correction Codes

The use of forward error correction (FEC) codes is standard in RF technologies and they have found application in optical technology [21-22]. It has been an important stepping stone to allow current digital signal processing, as it introduced the idea of high speed electronic pre and post processing to the optical community. FEC coding was first suggested in [23] without any indication of how the code would be implemented. The first error correcting code was developed by Richard Hamming [24]. A wide range of codes have been implemented for optical systems from Reed-Solomon codes [25] to concatenated codes. The current generation of codes, such as block turbo codes [26-27] and low density parity check codes [28], allow for error correction from error rates as high as 1×10^{-3}. FEC allows for relaxed system performance requirements. Generally, its' use allows for reduced launch powers

which reduce the impact of fibre nonlinearity or rephrase. This work will assume an FEC limit – a bit error rate which can be corrected to sufficient performance – of 1×10^{-3}. (fix formatting of this using an equation editor)

1.4 Traditional Dispersion Compensation

Critical limits in metropolitan distances are OSNR and group velocity dispersion (GVD). The physical origin of GVD and its effect on transmission will be described in detail in Chapter 2. In order to compensate for GVD, dispersion compensation methods are used which will be described in the following sections. Dispersion compensation is any method that can mitigate the transfer function of the optical fibre and allows for the signal to be recovered at the receiver. It can be implemented at the transmitter, in-line or at the receiver.

1.4.1   Dispersion Compensating Fibres

Dispersion compensating fibres (DCF) were first suggested in the1980's [29]but it was not until the 1990's [30-32] that they became a practical commodity. They work on the principle that, for two consecutive fibre sections which have opposite dispersion slopes [33], the overall accumulative dispersion is zero. DCFs exhibit relatively high losses because of increased bending loss if manufactured using depressed cladding. This results in a need to compensate for the DCF insertion loss which results in enhanced ASE noise and a depressed OSNR. They can also result in enhanced non-linear effects due to the small mode diameter (~20 μm^2).

Many of these problems have been alleviated in recent times with the advent of two-mode fibre designs [34-36]. These have losses that are comparable to those of SMF but they do require a mode converter to allow all fibre, broadband and polarisation

insensitive connectivity. There has also been efforts made to reduce the bulk of the dispersion compensation modules (DCM) [37] allowing for easier installation. DCFs have many advantages; in particular their broadband operation has made them a widespread accepted technology [33]. They do still, however, require precise provisioning which is an expensive process especially where link lengths can vary greatly. Also, once they are installed, they are expensive to change if links are spliced or some other factor causes dispersion changes. This allows for competing technologies to be proposed.

1.4.2   Bragg Gratings

A Fibre Bragg grating is an optical filter [38] which has a stop band, i.e. a frequency region where most of the incident light rephrase

$$\lambda_b = 2 \bar{n} \Lambda \tag{1}$$

where Λ is the grating period and $\bar{n}$ is the average mode index. It provides a frequency dependent reflectivity to the incident bandwidth determined by the grating strength. Uniform gratings have been used for dispersion compensation but they have a narrow stop band and this limits their useful bandwidth. In [39], chirped Bragg gratings are introduced such that the Bragg wavelength changes over the length of the grating. This gives a wider stop band and can be used at higher frequencies and longer distances up to 500 km for on-off keying at 10 Gbit/s and 700 km for duobinary signals [39-43]. A main limitation of Bragg gratings is that they are reflective filters and, therefore, the input and output must be separated – using a 3 dB coupler results in a 6 dB loss and ,even using a circulator, a 1 dB loss results. Also, the grating reflectivity must be <1 , otherwise there will be rippling in the output

power. This ripple limits the range of the Bragg gratings. They have a filtering effect which can be used for pulse reshaping [44] but limits the number of grating modules which can be concatenated.

1.4.3　　　　Optical Phase Conjugation

Midspan Optical Phase Conjugation (OPC) is a non-linear technique where the phase of the signal is inverted and then the remaining transmission fibre is used to undo the dispersion from the first half of the link [45]. Many techniques are used to induce this phase reversal [46-54]. It can be used on multiple wavelengths simultaneously, for high bit rates (>10 Gbit/s) and distances of up to 6000 km for 10 Gbit/s in simulation. Its performance depends on the efficiency of the FWM process, amplifier spacing, input power and operating wavelength but its main drawback is that the operation occurs midspan and the signal is not accessible at any other point along the link.

1.5 Analogue Dispersion Compensation

The seeds of the current interest in EDC compensation are found in work done using analogue electronics at lower bit rates which allowed for approximately 200% increase in the reach. These techniques are explained below.

1.5.1　　　　Pre-Distortion Technique

Pre-Distortion techniques use knowledge of the the transfer function of the fibre and the target transmission length to generate a transmitted signal which will unfold into the desired signal at the receiver due to the effects of fibre dispersion [41,47-48]. Various techniques are used to generate the pre-chirp technique from SOAs [49] non-

linear fibre [50], and electrical transmission lines [51-52]. Pre-distortion techniques suffers from a number of disadvantages – they require a complex transmitter (at least one dual drive MZM) and *a priori* knowledge of the dispersion of the link. They have the advantage that they are not noise limited. In section 1.6.2 , pre-distortion using DSP will be discussed.

1.5.2   Post-Detection Compensation

If the transmission along the fibre can be considered linear, then the dispersion can be compensated in the electrical domain. By converting the signal into a microwave signal preserving both the phase and amplitude information, an electrical band pass filter of may be used to compensate for dispersion. In the early 90's, a number of demonstrations of this using coherent detection and microstrip lines where reported which allowed for uncompensated transmission distances of up to 202 km [51-52,54]. Due to the advent of the EDFA, the need for increased receiver sensitivity was reduced which led to coherent detection research being suspended. In this thesis, a technique which does not require coherent detection to allow for a microwave image of the signal to be generated will be presented.

Receiver side direct detection electronic compensation was also examined, but due to the loss of the phase information arising from square law detection, compensating dispersion for a bit which has spread outside its bit slot is not linear. Several non-linear equalization techniques were developed to help recover dispersed signal e.g. adaptive threshold detection [10,55]. These techniques required high speed electronic circuits to operate and in the early 1990's such technology was not mature enough. Today renewed interest in such technology is possible though challenging.

1.6 Digital Enhanced Dispersion Compensation Methods

Due to the delay in deploying 40 Gbit/s systems due to the downturn in the optics industry in the early 2000s, electronic integrated technology has had a chance to gain pace with installed 10 Gbit/s systems. The first sign of this was the widespread acceptance of FEC technology (Section 1.3). In the last 4 years, the development of EDC technology has allowed the analogue electronic dispersion compensation methods to be implemented using the power of digital signal processing algorithms. These have been well developed in the satellite and mobile phone industries. The key components which are required for this are the implementation of Digital to Analogue (DAC) and Analogue to Digital Converters (ADC).

1.6.1 High Speed DACs and ADCs

High speed ADCs were first generally available in high end, real-time oscilloscopes [56-57] which allowed DSP algorithms to be tested in burst data collection and off line processing (Section 2.5). There has been a large effort in developing DACs and ADC chips suitable for EDC applications [19,58-61]. Over the last few years, the technology has reached the stage where 50 Gs/s ADCs are becoming commercially available on boards with FPGAs on which the algorithms that have been developed and tested using burst mode oscilloscopes can be demonstrated real-time. A number of companies already have products on the market which use high speed ADC [62-63]. Some research groups have already implemented DACs from individual components [64]. An ADC has not been demonstrated using individual components as it is very difficult to implement due to component variability, precise time alignment and stability of the overall systems with respect to environmental

conditions.

1.6.2   Pre-Distortion Dispersion Compensation

Pre-distortion techniques using DSP were first proposed in 2004 where 800 km transmission distance was simulated and a product was marketed by Nortel [15-16,65] which demonstrated 3840 km at 10 Gbit/s in 2006. There has been some queries about pre-distortion technique especially in wavelength division multiplex network. It can result in enhanced non-linear effects [66-67]. This is true for any electronic dispersion compensation method which allows for the build up of dispersion in long links and its effect must be considered. Any modulation format can be implemented using the pre-distortion technique. This technique offers large reach and the simple receiver. Pre-distortion uses knowledge of the fibre length to construct the required signal at a target dispersion. In practise this means that feedback is required from the receiver to the transmitter regarding system performance to establish the target dispersion. This can result in disruption in performance if the link changes suddenly and is not very suitable for switched networks. It also means that at any other point along the link the signal is inaccessible. This makes it unsuitable for multi-broadcast networks. In addition, the transmitted signal is multi-level and requires a sophisticated optical transmitter. This makes it less attractive for cost sensitive applications. It offers excellent distance and performance for point-to-point long distance links, e.g. sub-sea links.

1.6.3   Direct Detection Methods – Transverse Filters and MLSE

If one considers the simplest receiver side EDC, no modification of the detector is involved. Square law detection does not retain the phase information of the signal.

This results in a limitation in the maximum amount of dispersion that can be compensated as the link dispersion can no longer be considered a linear impairment. Despite this, a number of quite successful techniques have been demonstrated to provide dispersion compensation. The simplest of these are transverse filters [Finite Impulse Response (FIR) and Infinite Impulse Response (IIR)] which are linear filters [68-69]. Another technique used is Maximum Likelihood Sequence Estimation (MLSE) [70-71] which will be described in detail in Chapter 5. MLSE is a statistical technique which estimates the most likely received sequence using a series of observations rather than making a decision about a single bit. This offers improved performance with respect to the transverse filters. Transmission over 700 km of standard fibre at 10 Gbit/s was simulated, achieving a penalty of only about 3 dB with respect to 0 km transmission. However, a 8192 state trellis Viterbi decoder is required to implement the MLSE and this is significantly more complex than current technological capabilities. Experimentally, a distance of 600 km was shown using off-line processing and a similar number of states [72-74]. A practical receiver was demonstrated in 2004 [70-71] which has a 4 state Viterbi decoder and an uncompensated reach of 140 km. An interesting combination of the above was presented for long-haul applications where a FIR was used for coarse dispersion compensation followed by an MLSE for dispersion trimming [15]. This allowed for a reach of 5120 km but would require a complex optimisation of the operational parameters of the filter and MLSE. It does, however, give an example of how these techniques can be picked and mixed depending on the specific application. All of the compensation techniques described in this section are limited in their performance abilities by the loss of phase information in the receiver. Their reach could all be

dramatically improved if they had access to the amplitude and phase information of the signal.

1.6.4   Coherent Detection

To extend the effectiveness of electronic dispersion compensation, it has become necessary to convert the full received field into the electronic domain. The traditional method of doing this was to use coherent detection. Due to the development of the EDFA, dense WDM and as a result of the complexity of transmitters and receivers required for coherent detection, the widespread commercial deployment of coherent detection was delayed. Digital coherent detection has made great strides in regaining its place at the pinnacle of transmission research both for dispersion compensation and advanced modulation formats and will be addressed in Chapter 7. In this section, a brief introduction to coherent detection is presented and the state of the technology at the beginning of this thesis work is outlined.

The basic concept of coherent detection (see Section 10.1.1 in [53]) is the combination of the optical signal coherently with a continuous-wave (CW) optical field before it falls on a detector. The CW signal is a narrow linewidth laser located at the receiver and is referred to as the local oscillator (LO). Coherent detection can be homodyne or hetrodyne - the LO wavelength is equal or not equal to the receiver wavelength, respectively. For hetrodyne detection, the frequency difference is chosen to be in the microwave domain so that detection is possible. This relaxes the wavelength tracking required. Heterodyne detection operates at a maximum baud rate of half that of the bandwidth of the receivers. For high speed applications, homodyne receivers are more practical. However, this requires carrier phase estimation in the receiver. While this is still a complex problem, it is significantly

easier electronically rather than optically but it is still a challenging task. It allows for access to the full field but a number of degradations must be considered.

photo-diodes
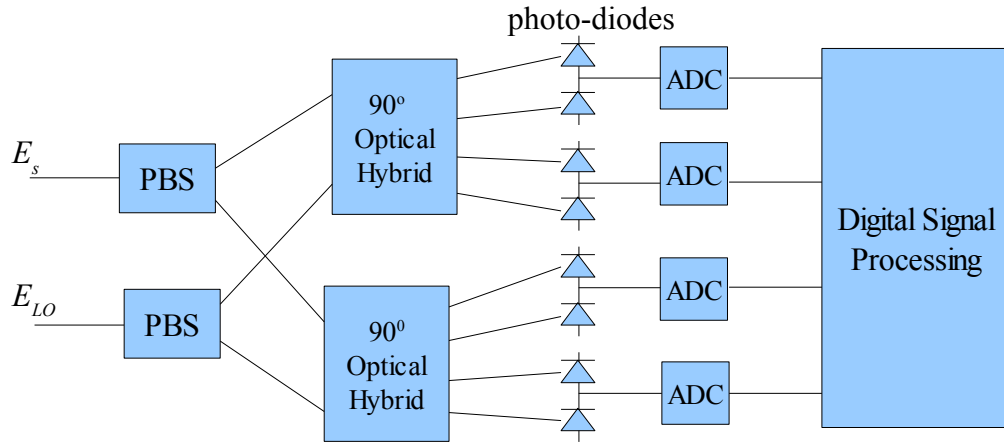
Figure 2: Schematic of a Phase and Polarisation diversity coherent receiver (PBS Polarisation Beam Splitters; ADC Analogue to digital converters).

The above assumes perfect components. In reality a number of impairments must be compensated for such as phase noise, intensity noise, polarisation and phase mismatch and wavelength tracking. Polarisation and phase mismatch can be alleviated by using an polarisation and phase diverse optical hybrid as shown in Figure 2. This combines the LO and the received signal in a number of known polarisation and phase shifts and the entire field can be reconstructed from the four ports. This comes at the expense of using a complex optical component and multiple photodiodes.

Coherent detection has been widely employed [10,51-55,75-77] in the past and there has been renewed interest in this technology since 2004 with the advances in electronic dispersion compensation[7,62,68,77-96].

1.6.5 Phase Estimation Full Field Detection

Section 1.6.4 describes how using coherent detection allows for significant performance enhancement for EDC, but at the cost of greatly increased optical and

electrical complexity. This thesis will present a novel receiver structure that allows for the benefits of having access to the full optical received signal but with a very much simplified single photodetector structure. The concept will be described in detail in Chapter 3. A frequency sensitive filter, an additional photodiode and some relatively simple calculations can be used to allow the full optical field to be reconstructed in the electrical domain and, consequently, allows simple and effective dispersion compensation to be implemented. Today, full-field detection remains a cost effective alternative to digital coherent detection with sufficient distance reach for metro area applications. While at the beginning of this thesis work coherent detection had been demonstrated [77], it had not yet been demonstrated as a viable product. The approach in this thesis was proposed as a practical means to access the field, which is the next step needed to improve electronic dispersion compensation, without the use of coherent detection.

1.7 Scope of the Thesis

In this work, a novel receiver concept is presented that allows for access to the full optical field without the need for coherent detection. It can be used in conjunction with analogue and digital dispersion compensation methods. The aim of this thesis is to provide a thorough theoretical and experimental investigation of full field estimation using phase estimation, with a view to demonstrating its feasibility as a novel, low cost and robust electronic dispersion compensation receiver. Experimentally the ability for the phase to be represented in the electrical domain is demonstrated. An optical transmission test bed was developed so that the potential of this technique is illustrated to enable EDC to be a cost competitive technology in metropolitan area networks. In addition, full-field detection was theoretically

characterised to determine its optimum parameters and its theoretical reach of greater than 2000 km was indicated. Its performance is investigated, theoretically and experimentally, utilising various dispersion compensation structures, such as frequency domain compensation and maximum-likelihood sequence estimation. It is shown that this receiver allows for significantly improved performance compared with amplitude only solutions and, in the target application space, provides an alternative of appropriate complexity compared to coherent detection.

1.7.1   Organisation of Thesis

In Chapter 2, a review of the relevant background theory is presented. The most important impairments in metropolitan area networks are investigated.

Chapter 3 presents the concept of full-field reconstruction. Preliminary simulations of the receiver are demonstrated. These show that this is a relevant technique which merits investigation and should be sufficient for our application.

Experimental demonstrations of the practicality of field detection are presented in Chapter 4. It is shown that it is possible to reconstruct a differential phase shift keying signal (DPSK opto-electro wavelength converter) and it may be used for dispersion compensation using analogue signal processing (mid-span spectral inversion MSSI). Some basic characterisation of the components used is introduced . The transmission system used (re-circulating loop) is described.

Chapter 5 offers detailed simulations of this technique with in-depth analysis of both transmission impairments and receiver parameters. It offers experimental results over field installed fibre (in collaboration with BT Ireland and BT and BT Innovation & Design, UK) using off-line, ideal frequency domain compensation demonstrating that this novel concept allows for dispersion compensation well beyond the

dispersion limit.

In Chapter 6, the adaptation of a popular EDC implementation of MLSE is considered. This offers excellent adaptive dispersion compensation for use with information of the whole received optical field. Theoretical and off-line experimental results are presented to demonstrate this concept and show that it allows for notable performance improvement when compared to amplitude only detection. This work could be considered for use also with coherent detection where one has access to the full optical field through a more more complex receiver.

1.7.2 Contributions of the Thesis

The main technical contributions to the field of optical communications are listed below

i.   The development and characterisation of a novel receiver for electronic dispersion compensated systems, particularly for use in metropolitan area networks where fast adaptation is required and monetary concerns are strict.

ii. A theoretical explanation of phase estimation and full-field reconstruction.

iii. A demonstration of the experimental feasibility of implementing phase estimation to replicate the phase information of a phase modulated signal using off the shelf components.

iv. Analogue dispersion compensation using full-field detection and mid span spectral inversion.

v.   Demonstration and amelioration of the full-field receiver's sensitivity to low frequency amplification due to process of generating the phase information from the integration of the instantaneous frequency by use of a high pass electrical filter and reduced extinction ratio.

vi.   In-depth simulations of FF-EDC using transmission lines for different link configurations, thermal noise limited receivers, different sample rates and showing that for optimum transmission links and performance that a theoretical reach of up to 2000 km is possible.

vii. Experimental results using off-line processing for reaches sufficient for metropolitan area networks using off the shelf components in a test bed in the Photonics Systems Group laboratory in Tyndall National Institute, Cork, Ireland using field-installed optical fibre between the Tyndall National Institute and Clonakilty, Co. Cork, Ireland provided by BT Ireland .

viii. An investigation into the vulnerable transmitted patterns for receiver side EDC – an isolated '1' whose energy had dispersed into surrounding '0'.

ix.   The development of a full-field maximum likelihood sequence estimation structure which utilises the full optical field and offers improved performance compared to amplitude only MLSE. Experimentally demonstrated this using off-line processing for metropolitan area reaches and full-field detection.

x.   Introduced a simplified MLSE algorithm which offers metropolitan area reach at significant reduced complexity compared to (ix) and comparable complexity to amplitude-only MLSE with very little penalty. Experimentally demonstrated same using off-line processing for metropolitan area networks and full-field detection.

1.8 Conclusion

This Chapter has introduced the target area for full field detector presented in this thesis - metropolitan area networks. In metropolitan area networks, the major limits of reach and performance are caused by the optical to signal noise ratio (OSNR)

limitation and group velocity dispersion (GVD), which will be introduced in the next chapter. The over-riding limitation, however, is cost. An outline of the contemporary solutions that were and are currently available to combat chromatic dispersion compensation has been given. Thus, in summary, the aim of this research for this thesis was to present a novel, low-cost electronic dispersion compensation method tested at the extrema of likely OSNR with minimization of terminal optics.

2 Transmission Effects in Metropolitan Area Networks

2.1 Introduction

This Chapter describes the key fibre propagation effects which limit contemporary metropolitan networks. Standard theory from propagation effects in optical transmission is well known and may be found in numerous standard texts such as [53,97-98]. This chapter is restricted to the outstanding issues for metropolitan networks – chromatic dispersion. Other effects, such as polarisation mode dispersion and fibre non-linearity have negligible impact in metropolitan area networks, provided that reasonable quality fibre is available and FEC is used to allow operation at moderate launch powers. In addition, a number of key concepts of this work will be introduced, including the relationship between noise distributions and performance in terms of bit error rate and a convenient normalised parameter – the Q-factor. Finally, a review of the confidence intervals is presented which may be placed on BER estimation from finite sample sizes in included.

2.2 Fibre Propagation

The non-linear Schrödinger equation that governs the propagation of optical pulses (pulse width ≥ 1 ps) inside single-mode fibre is given by

$$i\frac{\partial A}{\partial z}=\frac{-i}{2}\alpha A+\frac{1}{2}\beta_2\frac{\partial^2 A}{\partial T^2}-\gamma|A|^2 A \tag{2}$$

where A is the slowly varying amplitude of the pulse envelope, T is measured within

a frame of reference moving at velocity v_g (the speed at which the pulse envelope moves along the fibre). The terms on the left correspond to fibre loss (α), dispersion (β_2) and non-linear (γ) propagation respectively. Assuming that the power levels launched into the fibre are below the non-linear threshold for single mode fibre, the non-linear term can be neglected. This results in

$$i\frac{\partial A}{\partial z}=\frac{-i}{2}\alpha A+\frac{1}{2}\beta_2\frac{\partial^2 A}{\partial^2 \tau}$$

(3)

A solution can be found and is given by [53]

$$\tilde{A}(z,\omega)=\tilde{A}(0,\omega)\underbrace{\exp(\frac{-\alpha z}{2})}_{loss}\underbrace{\exp(\frac{i}{2}\beta_2\omega^2 z)}_{dispersion}$$

(4)

The loss term will simply decrease the amplitude as distance increases but the dispersion will change the phase of each spectral component of a pulse depending on the frequency and the distance of propagation. This can be used to predict the pulse evolution along a link given a known transmitted pulse. An example is shown in Figure 3. This shows how a 100 ps pulse chain propagates along a typical single mode fibre assuming linear transmission (α = 0.2 dB/km, β_2 = -17 ps/km/nm).

The fundamental explanation behind chromatic dispersion is that when an electromagnetic wave interacts with the bound electrons of a dielectric, the response of the medium depends on the optical frequency, ω. This is why the refractive index (*n*) is frequency dependent. The impact of the wave-guide and the distribution of the field between the core and the cladding of an optical fibre must also be considered for optical transmission. It allows for an effective average refractive index to be used. A propagation constant can be derived from the refractive index, which may be expanded using a Taylor series expansion.
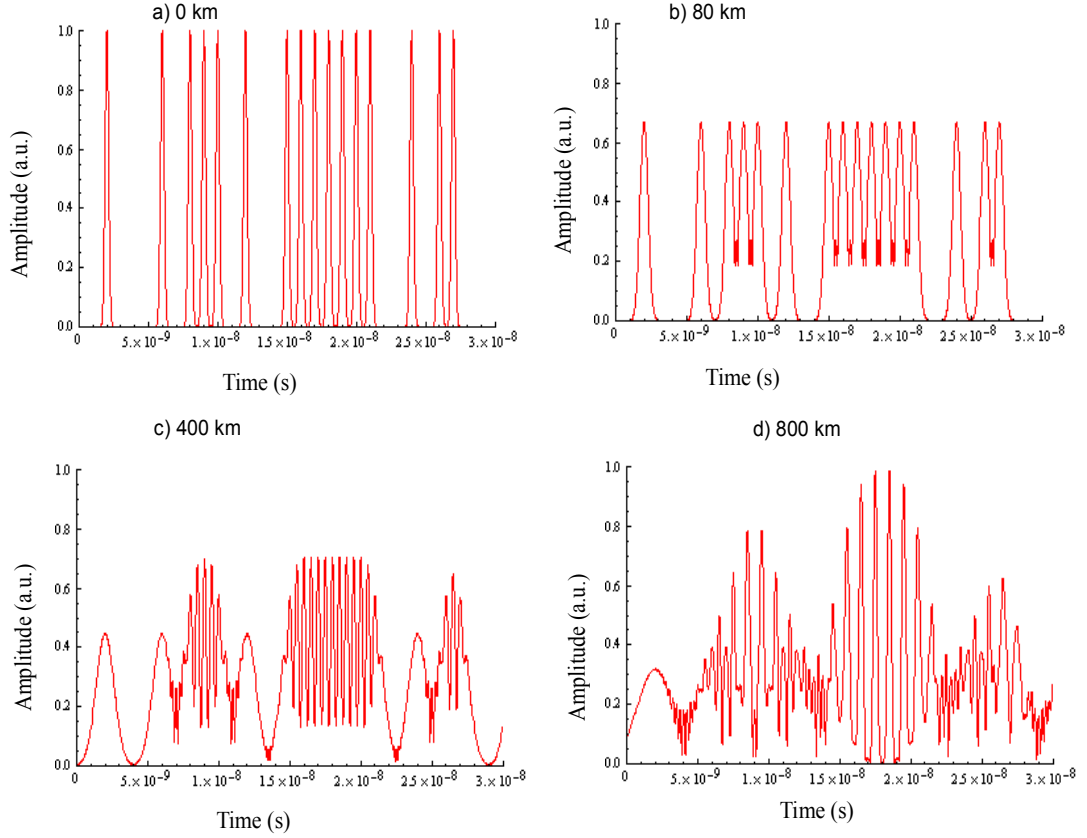
Figure 3: 10 Gb/s pulses transmitted over fibre up to 800 km.

The 1st order term represents the link delay, which is of no practical relevance in this work. Whilst in this thesis, the 3rd order term and higher order terms are sufficiently small to be neglected as the wavelength range considered is away from the zero dispersion wavelength (1300 nm $\leq \lambda_0 \geq$ 1324 nm for G.654 compliant fibre), the dominant dispersion parameter is the 2nd order term, which is given by

$$\beta_2 \approx \frac{\omega}{c} \frac{d^2 n}{d \omega^2} \quad . \tag{5}$$

β_2 is known as the group velocity dispersion parameter and has a typical value of -20 ps^2/km for SSMF. A related engineering factor, the dispersion parameter D, which is very useful for link design is also defined here:

$$D = \frac{d}{(d \lambda)} (\frac{1}{v_g}) = \frac{-2 \pi c}{\lambda^2} \beta_2 \tag{6}$$

D is expressed in units ps/nm/km.

31

The pulse shape and phase change is dominated by the second order term, β_2, and can be modelled using Fourier transforms (Figure 4).
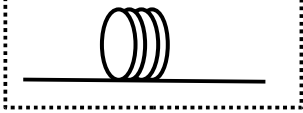
$$\exp(\frac{i}{2}\omega^2\beta_2 z)$$

$$A(0,t) \qquad A(z,t) = \frac{1}{2\pi} \int_{-\infty}^{\infty} \tilde{A}(0,\omega)\exp(\frac{i}{2}\omega^2\beta_2 z)\,d\omega$$

Figure 4: Simple model of dispersive transmission.

By considering a low pass equivalent model for the single mode fibre [98], the amount of pulse broadening is given by

$$\Delta T = \frac{dT}{d\omega}\Delta\omega = \frac{d}{d\omega}(\frac{L}{v_g})\Delta\omega = L\frac{d^2\beta}{d\omega^2}\Delta\omega = L\beta_2\Delta\omega \tag{7}$$

The spread of the spectral components $\Delta\omega$ depends on the range of wavelengths $\Delta\lambda$ emitted by the optical source. By expressing (7) in terms of $\Delta\lambda$,

$$\Delta T = \frac{d}{d\lambda}(\frac{L}{v_g})\Delta\lambda = DL\Delta\lambda \tag{8}$$

is obtained. This pulse broadening results in a penalty due to the overlap of pulses transmitted in different time slots for which the figure of merit , γ, may be defined [75]:

$$\gamma = \frac{1}{\pi}B^2 L D(\lambda)\frac{\lambda^2}{c} \quad , \tag{9}$$

 where B is the transmitted bandwidth and $\gamma = 0.321$ for 2 dB penalty for OOK.

The results of this are plotted in Figure 5 with $\lambda = 1550$ nm and $D = 16$ ps/nm/km. (9) shows that the penalty is proportional to the square of the bandwidth. This indicates that dispersion was not particularly limiting for most links at 2.5 GHz (this is for sources with limited $\Delta\lambda$) but is significant at 10 Gbit/s and is detrimental at 40Gbit/s if not compensated.
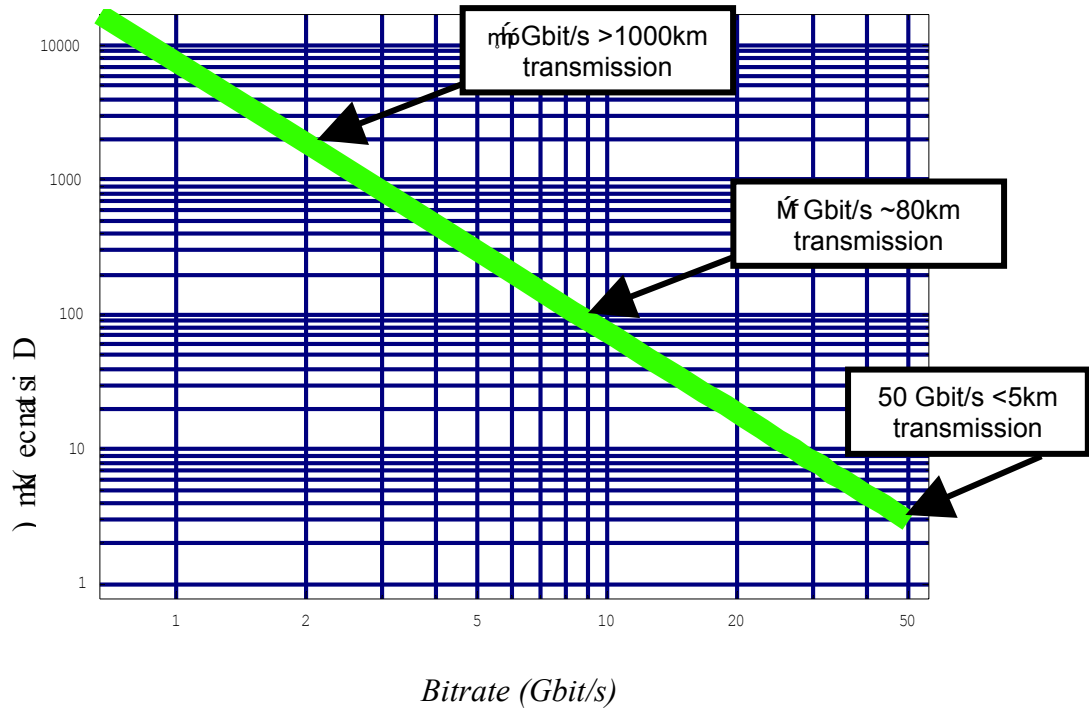
Figure 5: Distance versus Transmitted Bitrate for 2 dB transmission penalty

The effects of dispersion may be demonstrated in a simple VPI model. The FEC enabled transmission distance of 140 km is insufficient for metro applications. The fibre loss is neglected. Looking at the eye diagrams in Figure 6, the effect of pulse broadening and inter-symbol interference can be seen by the change in eye shape. The eye shape is distorted and will eventually close. These are typical shapes for dispersed eye diagrams and cause significant penalties.

The simulated eye diagrams have a limited number of paths as a pseudo random bit sequence of length 2^{11}-1 was used which is a relatively short pattern length. However, this pattern length will be used in this thesis due to the limitations in data processing using offline processing. Section 7.5.1 will mention how longer patterns lengths could be considered.
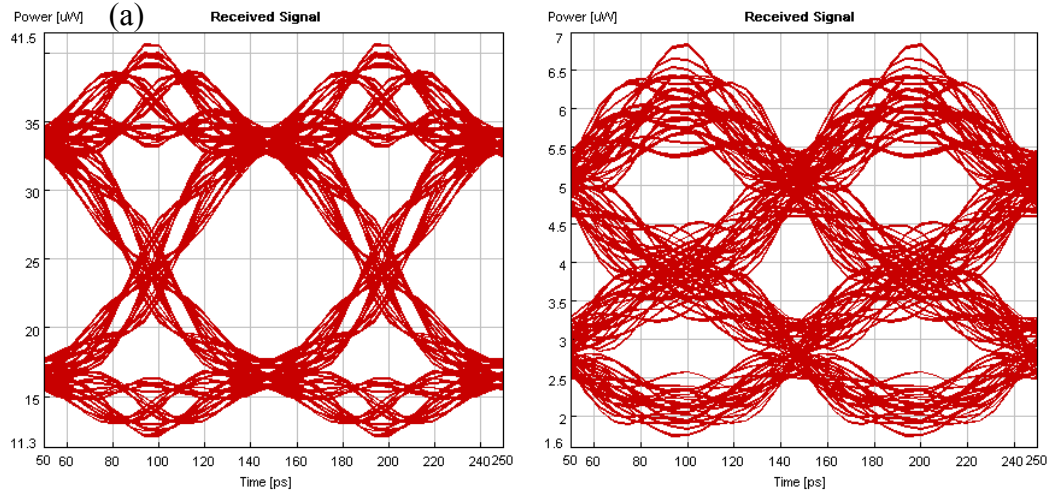
Figure 6: Eye diagrams for single link 0 dB launch power at (a) 80 km and (b) 120 km.

2.3 Bit Error Rate, Quality Factor and Eye Diagrams

Bit errors are the result of an erroneous decision being made in the estimation of transmitted sequence, generally due to the presence of noise. The bit error rate (BER) is given by:

$$BER = \frac{no.\,of\,incorrect\,received\,bits}{no.\,of\,transmitted\,bits} \quad . \tag{10}$$

For the on-off keying (OOK) signal shown below in Figure 7, the BER is given by:

$$BER = \frac{1}{2}[P(0|1) + P(1|0)] \quad , \tag{11}$$

where P(0|1) is the probability of deciding on a '0' when a '1' has been sent and vice versa and assuming '0' or '1' have equal probability of being sent. Using the assumption that noise is Gaussian [99], the BER can be approximated by

$$BER = \frac{1}{4}[erfc(\frac{\mu_1 - y_d}{\sqrt{2}\,\sigma_1}) + erfc(\frac{y_d - \mu_0}{\sqrt{2}\,\sigma_0})] \quad , \tag{12}$$

where μ is the mean of the distribution of '0' and '1', y_d is the optimum decision threshold and σ^2 is the variance of the distributions. From this a common approximation of the optimum decision threshold is given by
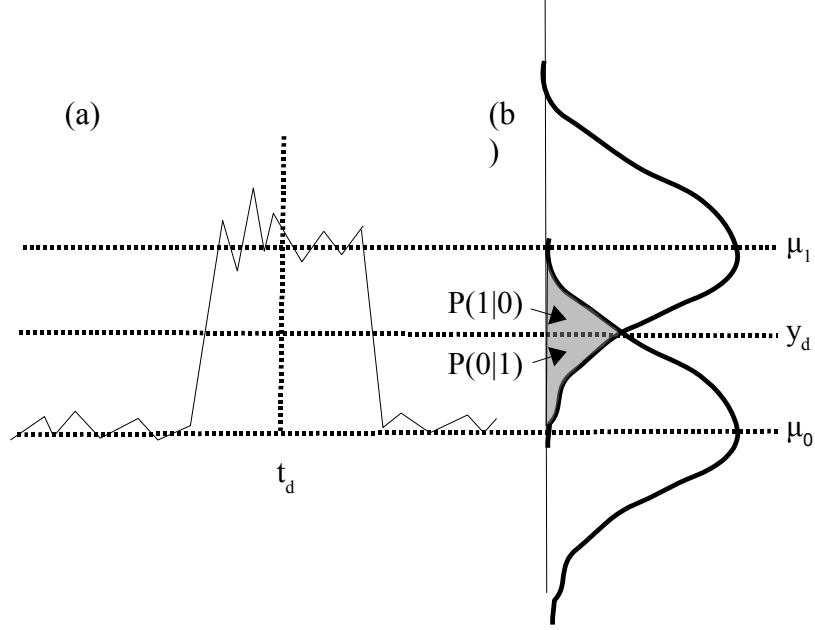
Figure 7: (a) On-Off Key Signal and (b) Error Distributions where t_d and y_d are the optimum decision time and threshold and $\mu_{1,0}$ are the mean of '1' or '0' level respectively.

$$y_d = \frac{\sigma_0 \mu_1 + \sigma_1 \mu_0}{\sigma_0 + \sigma_1} \quad , \tag{13}$$

which allows for the definition of a quality-factor or *Q*-factor by

$$BER = \frac{1}{2} erfc\left(\frac{Q}{\sqrt{2}}\right) \quad , \tag{14}$$

where

$$Q = \frac{\mu_1 - \mu_0}{\sigma_1 - \sigma_0} \quad . \tag{15}$$

Q can be defined for any signal for which mean levels and the noise powers/variance can be sensibly defined. This makes it possible to use in optical systems where the error distribution may not be equal, due to the use of EDFAs, resulting in more noise on the '1' level than the zero level, due to signal dependent signal-spontaneous beat noise.

A common way of representing pulse sequences, especially in optical systems, and to provide a quick and qualitative description of the received signal is called an eye

diagram. An eye diagram is generated by sampling the data repetitively with persistence while the data rate is used to trigger the horizontal sweep on an oscilloscope (Figure 8). The result is the overlapping of all the possible transitions from the levels. The Q-factor measurement may be made directly from the eye diagrams and is a measurement of how open or undistorted the eye is. Many other measurements can be made from the eye diagrams, such as amplitude and jitter measurements which are important for systems diagnostics. In this thesis, many eye diagrams will be presented and used to illustrate system performance and its limiting factors. The Q-factor is used to illustrate general parametric trends. However, from Chapter 4 onwards, performance is assessed through direct error counting except where stated.
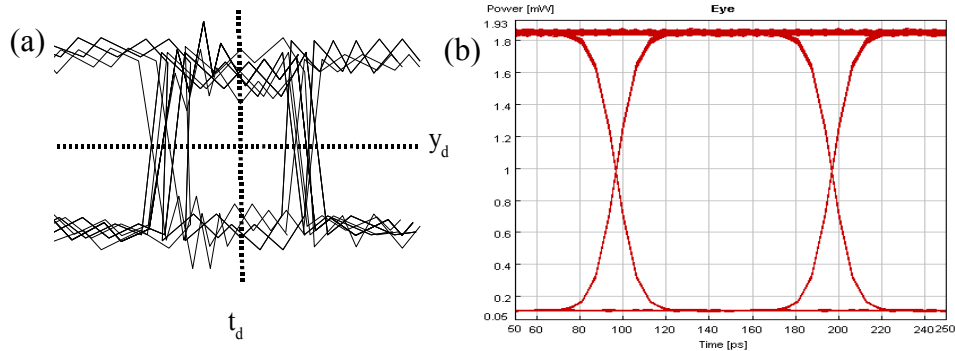
Figure 8: (a) Schematic representation of an eye diagram generated from over lapping pulse patterns (b) An example generated in VPI of a very good, undistorted eye.

2.4 Real Time Sampling Oscilloscope

Due to the difficulty at the time of the experiment in acquiring ADCs of sufficient bandwidth and FPGAs with an adequate number of high speed inputs to allow simultaneous sampling of two signals at greater than 20 Gsamples/sec, an oscilloscope with grab-and-store real time sampling was used. The scope used was a

36

Tektronix DPO70000 series scope. This allows for sampling of four signals simultaneously at multiples of 12.5 Gsamples/sec up to 50 Gsamples/sec. The total analogue bandwidth of the receiver is 16 GHz. In Figure 9, a series of 0 km transmission eye diagrams are shown. 9(a) and 9(b) are screen shots from the DPO and show the effect of limited sampling. 9(c) shows the familiar sampling/equivalent time oscilloscope screen shot as reference to compare with the real time sampling pictures and 9(d) shows the eye diagram which has been reconstructed using off-line processing(see section 2.5). By using 50 Gsamples/sec, which is 2.5 times the Nyquist rate, almost all the information is retained. The eye diagrams are very similar. However, when 25 Gsamples/sec is used as the sampling rate, the eye diagrams becomes much more angular as the higher frequency components of the signal are not recovered. This is still greater than the Nyquist rate so all the data information is present and the eye is visible. Using a sampling rate <20 Gsamples/sec would mean that the eye diagram would not be able to be constructed. The difference between 9(b) and 9(d) is that 9(b) uses sinc interpolation and (d) uses linear interpolation to approximate the path between samples.

The sampling rate that was used in this work is 50 Gsamples/sec. This is because the data rate used is 10 Gbit/s and this allows for an integer number of samples per second to be recorded and the samples will be at the same relative location for adjacent bit periods. The influence of number of sampling points per bit period is discussed in Chapter 5.
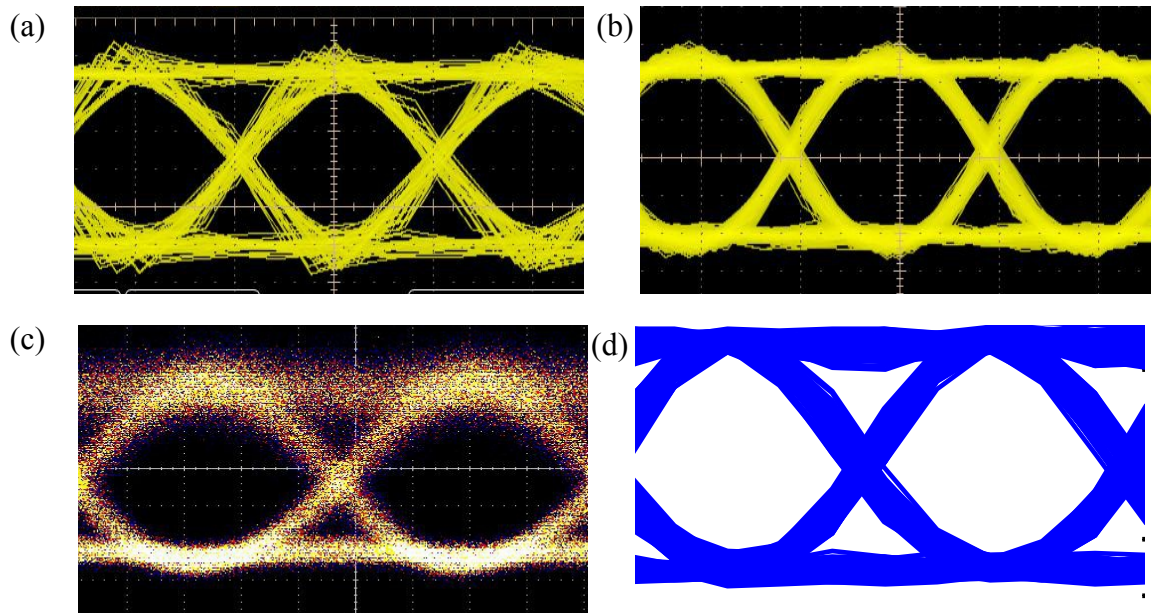
Figure 9: 0 km transmission diagram (a) sampled at 25Gsamples/sec (b) at 50Gsamples/sec (c) using a standard sampling oscilloscope and (d) is (b) reconstructed in MATLAB (horizontal scale 25 ps/div, vertical scale a.u.).

2.5 Off-Line Processing of Data

The scope has a single shot approach to sampling – once triggered the scope will write a *.txt file containing the requested number of samples. This is transferred to a PC where off-line processing is completed using MATLAB programs. This has become a widespread research method for analysing the effectiveness of using high speed DSP in optical communication systems. It has a number of major limitations both in terms of product development and experimental set-up. It does not allow for on-line error rate measurement and the consequences of this are discussed in Section 2.6 . It takes minutes to transfer sufficient samples to the off-line computer and longer to implement digital clock alignment and error counting. This makes it difficult to preform precise system tuning for this technique since the bias of the AMZI and the relative time delay in the lab set between the two sample paths are critical parameters which drift with ambient temperature and must be aligned

38

carefully. Figure 10 shows a screen shot of the two sample channels where the AMZI is slightly biased away from quadrature – the phase eye is open and should be closed for back-to-back modulation. This is obvious when clear eyes are available but virtually impossibly to see from the raw data after transmission as the received eye is closed due to dispersion and this hides any inaccuracies in the experimental set-up. It would only be obvious after processing which takes a significant amount of time. Therefore, in order to fine tune the experimental parameters, it was necessary to design a quasi-real time processing program for the system.

Time (25 ps/div)
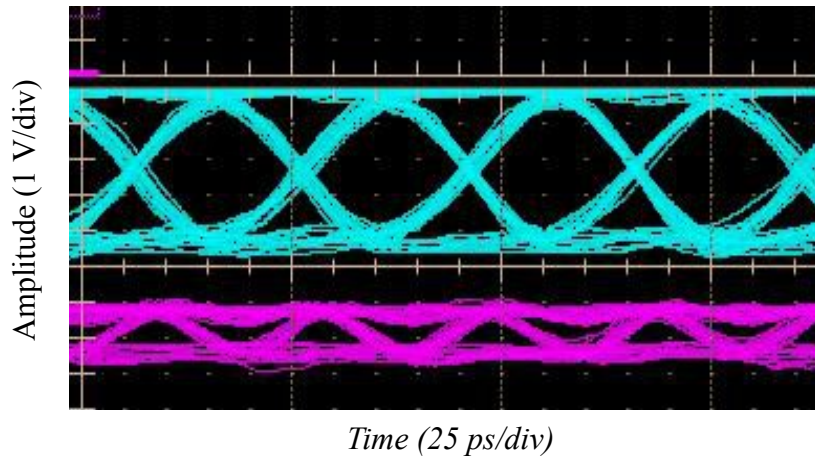
Figure 10: Screen shot of 0 km transmission eye diagrams of amplitude and phase information .

The process which was used to provide a quick indication of current system performance was a LabVIEW program outlined below in Figure 11. The main delay after the file capture time is the system is the Ethernet connection which has a transfer rate of ~6 Mb/s. This gives a refresh rate of ≤3 kHz. This is negligible in terms of the file capture time. The file capture time includes a wait for the trigger, which is a combination state trigger given by the loop trigger and a capture command from the LabVIEW program, and the write time to the slow speed memory. This gives a delay of about 1-10 s depending on instantaneous conditions. This limits the

refresh rate to ≥1 Hz. This is not real time but it is sufficient to allow for system optimisation. Efforts were made to replace the user input parameters by using a metric which qualifies the performance of the system e.g. Q-factor or ideally bit error rate. This, however, slowed down the refresh rate considerably. For error rates the PRBS has to be synchcronised to the incoming data and such small samples sizes do not have the entire PRBS sequence so accurate estimation is difficult at the high BERs which are typically seen in EDC systems. For Q-factor, similarly, a threshold point to separate '0' and '1' levels has to be estimated. In Figure 11, the eye diagram is relatively good. In general, for incorrect parameters, the eye diagram is very collapsed and experience is the most efficient way of tuning the system quickly given such slow electronics. It also illustrates the complexity of tuning EDC techniques in the presence of high dispersion.

In order to give intelligence to the choice of user input parameters, the sensitivity of the system performance to these has been investigated in Section 5.19 . It has been found that three of the parameters (amplitude, phase and delay) are essentially constant for a particular receiver structure and components. This makes tuning in the presence of high dispersion a more manageable task then it appears from this program, which has four degrees of freedom. While this offers a workaround solution to not having a live metric with which to tune the system, it does not replace the need to create a real-time demonstrator using ADCs and FPGAs to allow for on-line error rates to be estimated.

DPO70000 series

To Scope: Ready signal;data file size; capture rate
To Labview : Data ready signal

1k samples

Interal hardrive

amp.txt
phase.txt

Small file size-
Re-capture rate ~10 sec

Transfer to PC
Over Ethernet

MATLAB imbedded in labview
To MATLAB: user paramters
To LabVIEW : finish signal/new data

Transmission line compensation

User interface with number of ajustable
Critical compensation paramter e.g.

comp	-380
amp	1.2
phase	1
delay	15

Field reconstruction

$$V = \sqrt{(amp)} * e^{(\iota \int (phase))}$$

Using amp,phase and delay paramters

Compensation

$$Signal = ifft\left(fft(V).e^{\frac{\iota}{2} Distance * Disp \omega^2}\right)$$
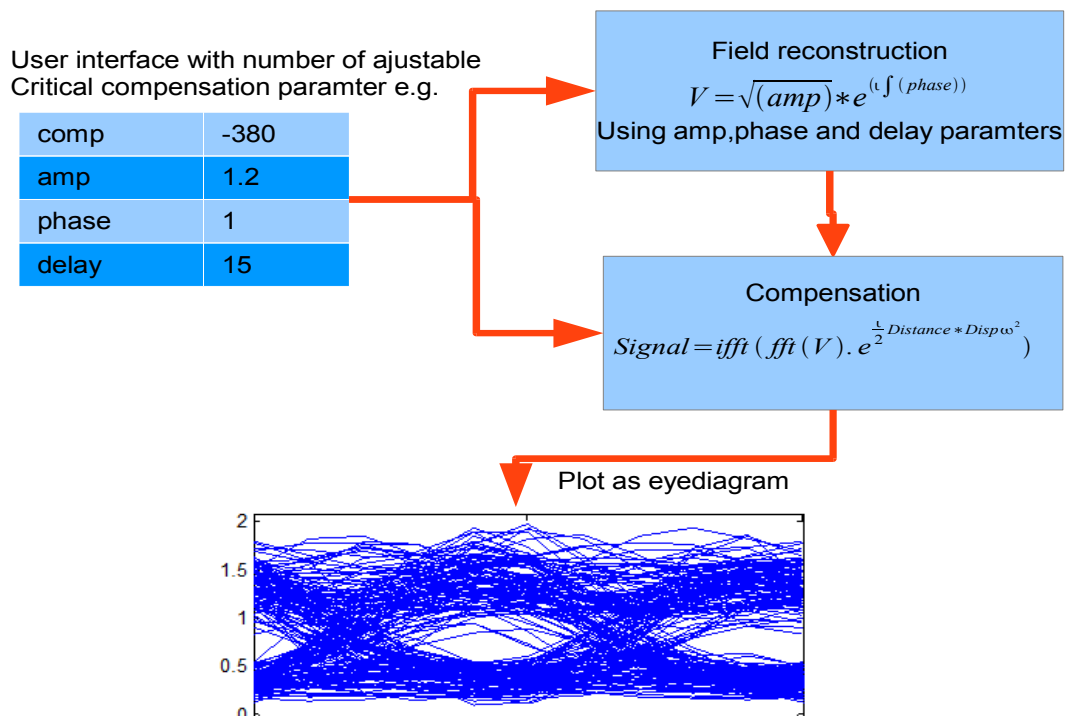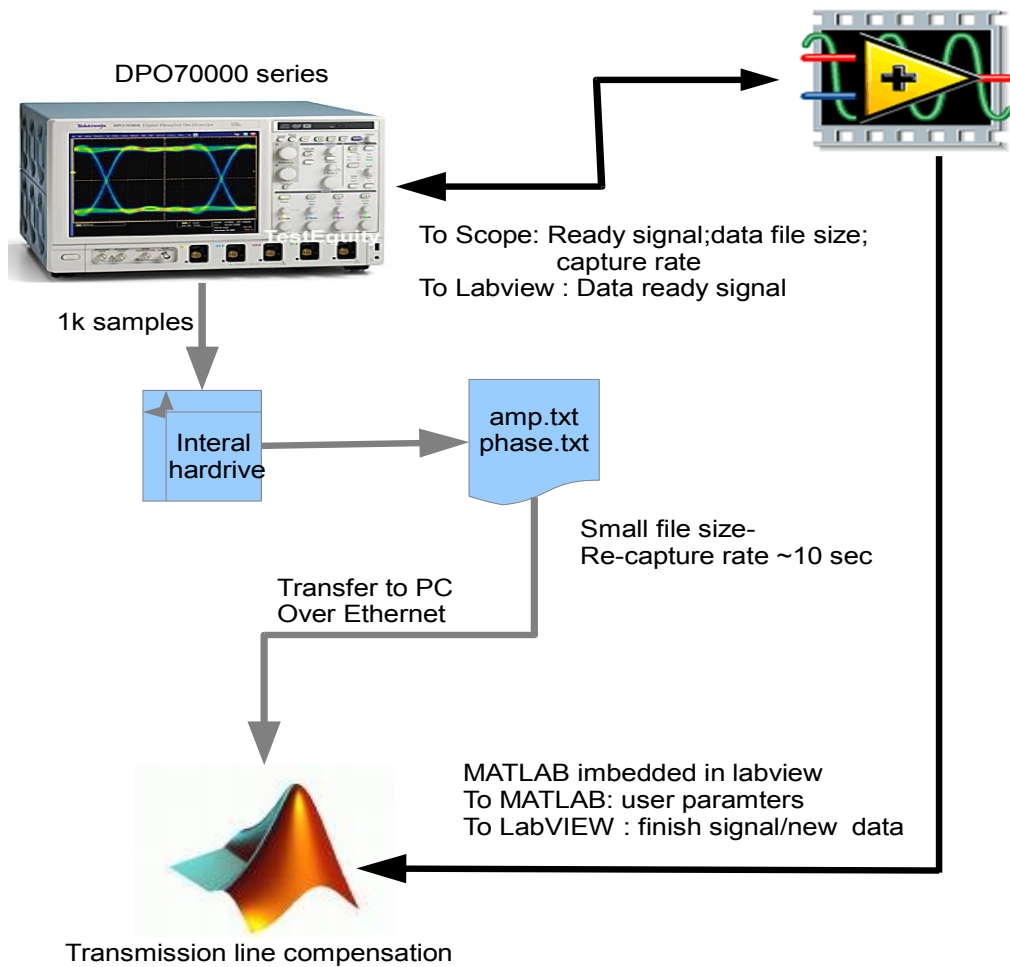
Plot as eyediagram

Figure 11: Data Capture, reconstruction and eye diagram generation.

41

2.6 Sample Size and Error Rate

For off-line sampling for lower error rates $<10^{-5}$, it is important to consider the statistical implications of limited sample size. Statistical analysis differs from real time as computer power limits the number of samples that it is practical to consider and that can be considered concurrently. In order to estimate BER, the confidence intervals that result from the sample size and error rate measured must be considered. An example of the variability of the error rate is shown in Figure 12. This data is taken from results given in section 5.17 at 496 km and an OSNR of 22.2 dB).The data is analysed in subsets of 20,470 bits ($10*2^{11}-1$ PRBS lengths) which is 2.05 μs . This should be shorter than any overall drift in the experiment. Figure 12 shows how the error rate per subset changes over 100 consecutive subsets, taken by sub-dividing the same measurement into 100 bins. Each of these bins contains 20,470 bits. The size of the sample required to describe a particular error rate of 10^{-n} with sufficient confidence is a minimum sample size of $>10^{n+1}$. This is equivalent to the rule of thumb that a minimum of 10 errors is required to ensure a representative error rate.

To carry out a statistical analysis, each bit is considered as a binary trial, with an error representing one of two outcomes. This actual BER is the mean number of errors over the entire message or population of trials. A BER measurement corresponds to taking a sample of this population and the measured BER may be considered the sample mean of the population. This is is a well known statistical problem [105] for discrete binary random events.

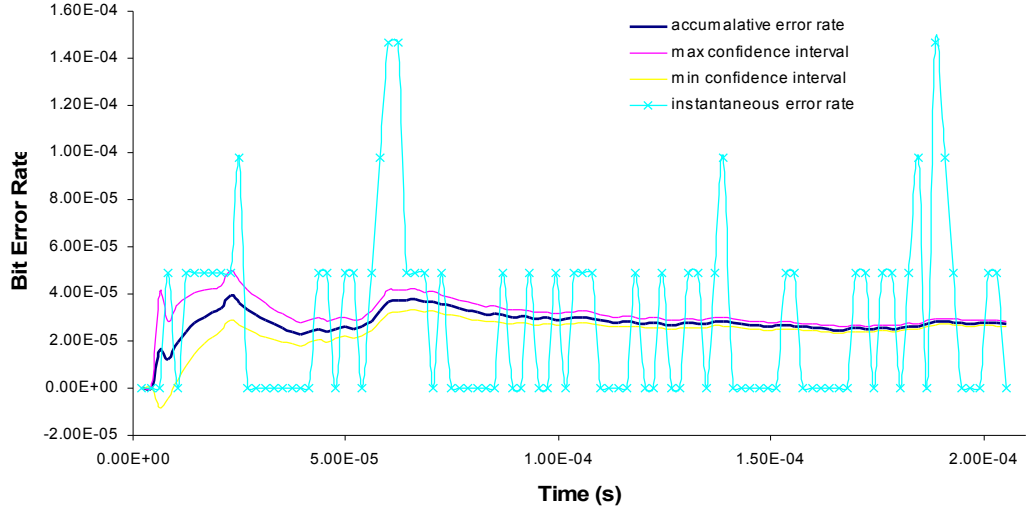*Figure 12: Instantaneous and accumulated bit error rate with 99% confidence intervals.*

The distribution of sample errors is given by Poisson's Distribution

$$P_r(X=x) = \frac{\mu^x e^{-\mu}}{x!} \quad , \tag{16}$$
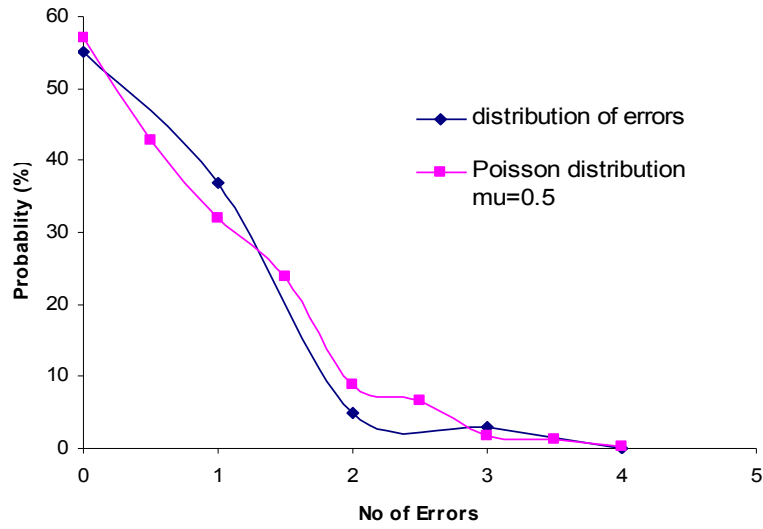
,where μ is the mean value of BER.

Figure 13: Distribution of errors (navy) and Poisson distribution (magenta).

The confidence interval limits are given by

$$limit = \mu \pm z_{0.99} \times \sigma$$

43

where z is the Z-score. This gives the following table for the above error measurement.

Table 1: Statistical properties of error measurement

Number of bits	100* 20470	
mean	56	
std deviation	0.72918939	
99.00%	2.4383919	
max	58.44	$2.85*10^{-5}$
min	53.56	$2.62*10^{-5}$

The total number of observed errors is 56 which indicates a measured sample error rate of $2.74*10^{-5}$ with a 99% confidence interval of $[2.62*10^{-5}, 2.85*10^{-5}]$. If only one sample of 20,470 bits were considered the measured error rate could range from error free to $1.47*10^{-4}$. This illustrates the importance of using sufficient sample sizes. Consequently, in this thesis, for the lowest reported bit error rate (which is the example described here), the sample size is sufficiently large not to be the main source of experimental error.

2.7 Conclusion

This chapter has described the physical nature of the problems resulting from propagation in single mode fibre, specifically for conditions associated with metropolitan area networks. It has been shown how dispersion causes pulse spreading and inter-symbol interference that result in a limited transmission distance unless it is compensated for. It investigates the effect of sample size and accuracy on BER estimation.

3 Principle of Full Field Detection

3.1 Introduction

This thesis presents a novel approach to enabling dispersion compensation over sufficient distances to facilitate deployment in metropolitan area networks. This chapter will explain the basic concept proposed to enable phase estimation and, for the particular implementation investigated in this thesis, the recovery of the frequency and intensity information for the received signal will be demonstrated analytically. It will be shown that, using proof of principle simulation, a transparent reach of 600 km is readily achieved. This will be compared to competing technologies already outlined in Chapter 1. For detailed theoretical calculations of the limits to these alternatives the reader is invited to consult the references in Chapter 1, but they will be summarized briefly here.

Direct-detection systems using MLSE (discussed in detail in Chapter 6) offer transmission reach up to 700 km for complexities unsuitable for volume production. The dispersion compensation capabilities of electronic pre-distortion are theoretically unlimited, but, in practice, are limited by OSNR and available high speed memory. Whilst reported reach of many thousands of kilometres is more than sufficient for today's applications, the signal is only detectable over a range of ~160 km (defined by the underlying modulation format) and so is unsuitable for rapidly varying link configurations. Coherent detection removes the restrictions on signal visibility; however, the high cost associated with these systems enable an opportunity for a lower cost solution – such as the one presented in this thesis.

3.2 Frequency Sensitive Receiver [viii]

As the signal is dispersed, the frequencies that make up the pulses become separated in time as they travel at marginally different speeds along the fibre. A frequency sensitive filter can be used to detect this effect. This allows for the entire optical signal to be reconstructed in the electrical domain. There are many options for highly effective linear dispersion compensation and these will be illustrated later in this work.

A square law detector is used to generate an electrical output proportional to the amplitude. An electrical signal proportional to the frequency shift of the incoming optical signal is generated using an optical device whose output changes linearly with respect to input frequency. It is required to be very sensitive to small changes in frequency shift and also to the direction of frequency shift. An example of one such device is discussed in the next section.

3.3 Asymmetrical Mach-Zehnder as Frequency Sensitive Filter

An asymmetrical Mach-Zehnder interferometer (AZMI) consists of two 50:50 couplers connected by two paths of different lengths and with a differential phase difference between them which may be controlled. A schematic diagram is shown in Figure 14. The method of control depends on the technology used to implement the AMZI. The AMZI used in the experimental part of this thesis is a planar lightwave circuit (PLC) interferometer and the path lengths are adjusted using heaters.
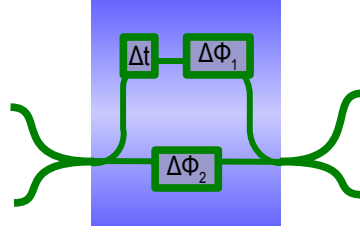
Figure 14: Schematic diagram of an asymmetric Mach Zehnder modulator.

The phase shift difference between the two paths is given by

$$\Delta\phi_1 - \Delta\phi_2 = \Delta\phi' \quad , \tag{17}$$

and this is termed the differential phase difference. Δt is the differential time delay between the two paths through the interferometer. The phase of each arm depends on the physical length, effective refractive index and the signal wavelength. It may, therefore, be anticipated that the frequency response of the AMZI would be sinusoidal with an appropriately scaled axis. This will be verified in Section 3.4 . When the AMZI is biased at quadrature ($\Delta\Phi' = 90°$), it can be viewed as a frequency sensitive filter with a linear transfer function within certain limits.

Figure 15 is an illustration of a pulse spread across multiple frequencies due to transmission. Due to the transfer function of the AMZI shown above these will tend to be separated into blue chirped and the red chirped components at the two outputs of the AMZI.
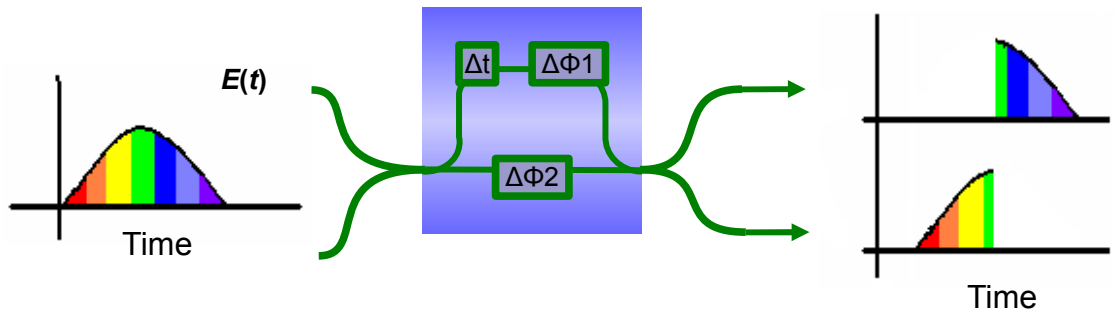

Figure 15: Schematic of a spread pulse being filtered by AMZI as a linear filter

These output signals are detected by square law detection (Figure 16) and result in

47

two voltages, $V_1(t)$ and $V_2(t)$ as indicated. The path of these voltages relative to $\Delta\Phi$ is shown schematically in Figure 17. The yellow dot indicates the output when biased at quadrature and at this point, the two outputs are equal.
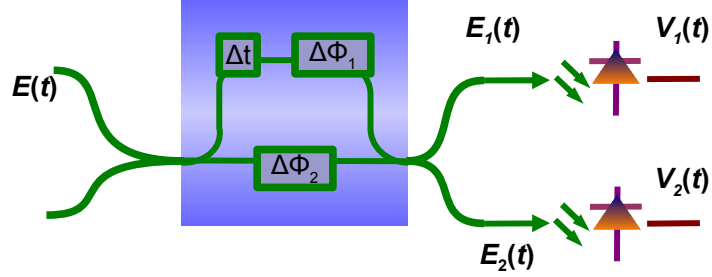
Figure 16: Square law detection of output of AMZI

As $\Delta\Phi$ decreases, V_1 decreases and V_2 increases and vice versa when $\Delta\Phi$ increases. For small changes in $\Delta\Phi$, this occurs approximately linearly. This means that there is a direct correlation between the difference in the relative voltages V_1 and V_2 and the value of $\Delta\Phi$.
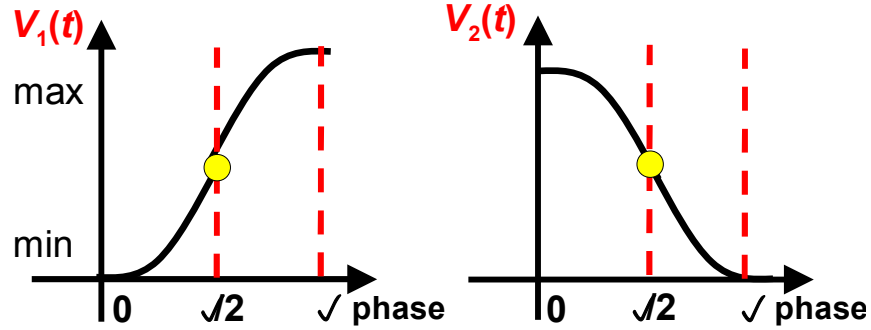
Figure 17: Voltages versus $\Delta\Phi$ of the AMZI

When the AMZI is biased at quadrature for a particular continuous wavelength (CW), the difference in the outputs from the two arms of the AMZI is related to the instantaneous chirp (or instantaneous frequency) of the incoming signal. This can be used to obtain the instantaneous phase. Using a representation of the instantaneous phase and the amplitude of the signal, the signal can be reconstructed in the electrical

domain. The next section will give a mathematical description verifying the functional form of the signal proportional to the amplitude and chirp.

3.4 Simple Description of Theory

Assuming that the input optical field (baseband representation) is $E_0(t)$, the two outputs of the AMZI, $E_{1,2}(t)$, are given by:

$$E_{1,2}(t) = \frac{E_0(t)}{2} (e^{i(\omega t + k z_1 + \phi_1)} \pm e^{i(\omega t + k z_2 + \phi_2)}) \tag{18}$$

where the difference in the phase shift of the two paths is given by $\Delta \phi' = \phi_1 - \phi_2$ where $\phi_2 = 0$. Let z given by $z = z_1 - z_2$ be the path difference between the two asymmetrical paths through the Mach-Zehnder interferometer. This sets the free spectral range of the AMZI and is a constant. Let ΔT be the difference in flight time for a signal propagating along the two arms of the AMZI, such that

$$\Delta T = \frac{k_1 z_1 - k_2 z_2}{\omega} \quad , \tag{19}$$

where

$$k = n \frac{\omega}{c} = \frac{n 2 \pi}{\lambda} \quad . \tag{20}$$

Then

$$E_{1,2} = \frac{E_0(t)}{2} e^{i(kz_1 + \phi_1)} [e^{i \omega t} \pm e^{i(\omega(t - \Delta t) + \Delta \phi')}] \quad . \tag{21}$$

Factorising eqn. (21) using trigonometric identities gives:

$$E_{1,2} = E_0(t) e^{i(\omega(t + \frac{\Delta T}{2}))} e^{i \Theta} \begin{matrix} \cos \\ i \sin \end{matrix} [\frac{\Delta \phi' - \omega T}{2}] \quad , \tag{22}$$

where Θ is a fixed phase offset and may be neglected without loss of generality since the carrier phase offset is unknown. Let

$$-\Delta \phi = \Delta \phi' - \omega_0 \Delta T \tag{23}$$

and

$$\Delta\omega=\omega-\omega_0 \quad, \tag{24}$$

then

$$E_{1,2}=E_0(t)e^{i(\omega(t+\frac{\Delta T}{2}))}\begin{matrix}\cos\\-i\sin\end{matrix}\left[\frac{\Delta\phi+\Delta\omega\Delta T}{2}\right] \tag{25}$$

$E_1(t)$ and $E_2(t)$ are detected by a pair of detectors, electrically amplified, and filtered by electrical filters (EFs) to obtain the voltage signals $V_1(t)$ and $V_2(t)$:

$$V_1=\alpha_1|E_0(t)|^2\cos^2\frac{(\Delta\omega\Delta t+\phi)}{2}$$

$$V_2=\alpha_2|E_0(t)|^2\sin^2\frac{(\Delta\omega\Delta t+\phi)}{2} \tag{26}$$

where $\tilde{\alpha}_1$ and $\tilde{\alpha}_2$ are scaling factors taking into account the responsivities of the detectors and the gains of the electrical amplifiers for the $V_1(t)$ and $V_2(t)$ signal paths. Figure 18 shows how the voltages V_1 and V_2 from equation (26) will change depending on the value of $\Delta\omega\Delta t$. The magnitude of the response will be scaled linearly by $|E_0(t)|^2$.

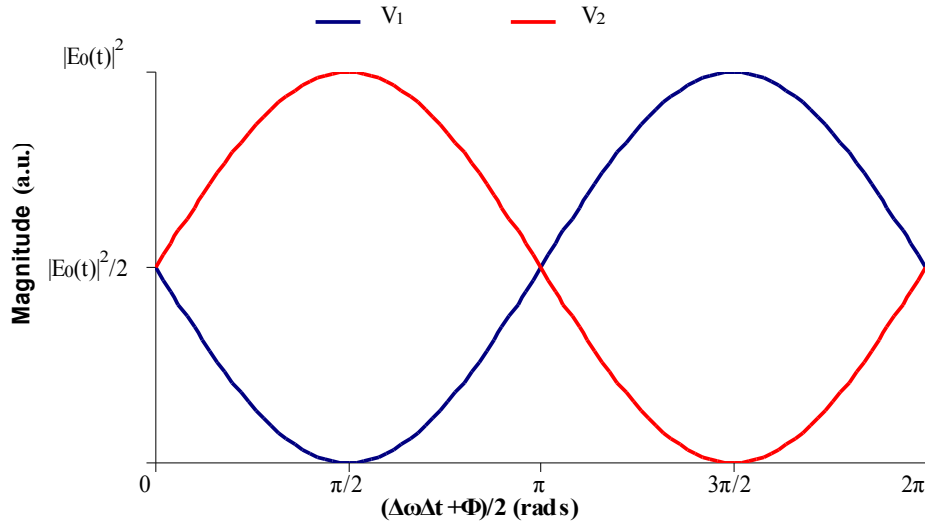Figure 18: V_1 and V_2 as a function of $\Delta\omega\Delta t$. The response will be scaled depending on the instantaneous baseband input voltage $|E_0(t)|^2$ but the shape will remain the same. This assumes $\tilde{\alpha}_1=\tilde{\alpha}_2=1$

For analytical simplicity, $\gamma_1 = \gamma_2 = 1$ is assumed. Signals proportional to the intensity, instantaneous frequency and phase information of the optical fields, $V_A(t)$, $V_f(t)$, and $V_p(t)$, can be extracted by signal processing of $V_1(t)$ and $V_2(t)$ as follows:

$$V_1 + V_2 = E_0(t)^2 \left(\sin^2 \frac{(\Delta \omega \Delta t + \phi)}{2} + \cos^2 \frac{(\Delta \omega \Delta t + \phi)}{2} \right) \quad . \tag{27}$$

Using $\sin^2 A + \cos^2 A = 1$

$$V_1 + V_2 = |E_0(t)|^2 \quad . \tag{28}$$

Thus, the sum of the voltages is proportional to the magnitude of the incoming signal and, from this, the amplitude of the signal can be calculated. This is intuitively pleasing as, regardless of the AMZI bias or instantaneous frequency of the signal, all of the light entering the AMZI will leave through one or other of the ports (minus the insertion loss, of course).

To get the instantaneous frequency we use

$$\frac{V_2 - V_1}{V_1 + V_2} = \frac{|E_0|^2 \left(\sin^2 \frac{(\Delta \omega \Delta t + \phi)}{2} - \cos^2 \frac{(\Delta \omega \Delta t + \phi)}{2} \right)}{|E_0|^2} \quad . \tag{29}$$

Using $\cos 2A = 1 - 2\sin^2 A = 2\cos^2 A - 1$ we have that

$$\frac{V_2 - V_1}{V_1 + V_2} = -\cos(\Delta \omega \Delta t + \phi) \quad . \tag{30}$$

Now, by biasing the MZM at quadrature, i.e. $\phi = \frac{\pi}{2}$, and using

$\cos(A + \frac{\pi}{2}) = -\sin A$ gives that

$$\sin^{-1} \frac{V_2 - V_1}{V_1 + V_2} = \Delta \omega \Delta t \quad . \tag{31}$$

51

Using the assumption that $\Delta\omega\Delta t \to 0$ and the linear approximation from the Taylor series , it is possible to write

$$V_f(t) = \frac{V_2 - V_1}{V_1 + V_2} \approx \Delta\omega\Delta t \quad . \tag{32}$$

The intensity and frequency information is exploited to reconstruct a replica of the optical signal in the radio frequency (RF) range by applying the signals V_A and V_f to amplitude and frequency modulators respectively, allowing for subsequent full optical-field compensation using a dispersive transmission line.

3.5 Proof of Principle Simulations (VPI Transmission Maker Version 6.5)

For this preliminary study, a limited set of simulation tools were employed to establish the general performance limits of the proposed technique [14]. A full simulation investigation using a combination of VPI and MATLAB is reported in Chapter 5.

The scope of this section is confined to proving that (i) sufficient reach (~600 km) can be achieved using this technique to satisfy current metro networks and (ii)it can be suitably robust for European scale metro networks where links can vary from 40 -100 km. This work was completed using VPI transmission maker 6.5.
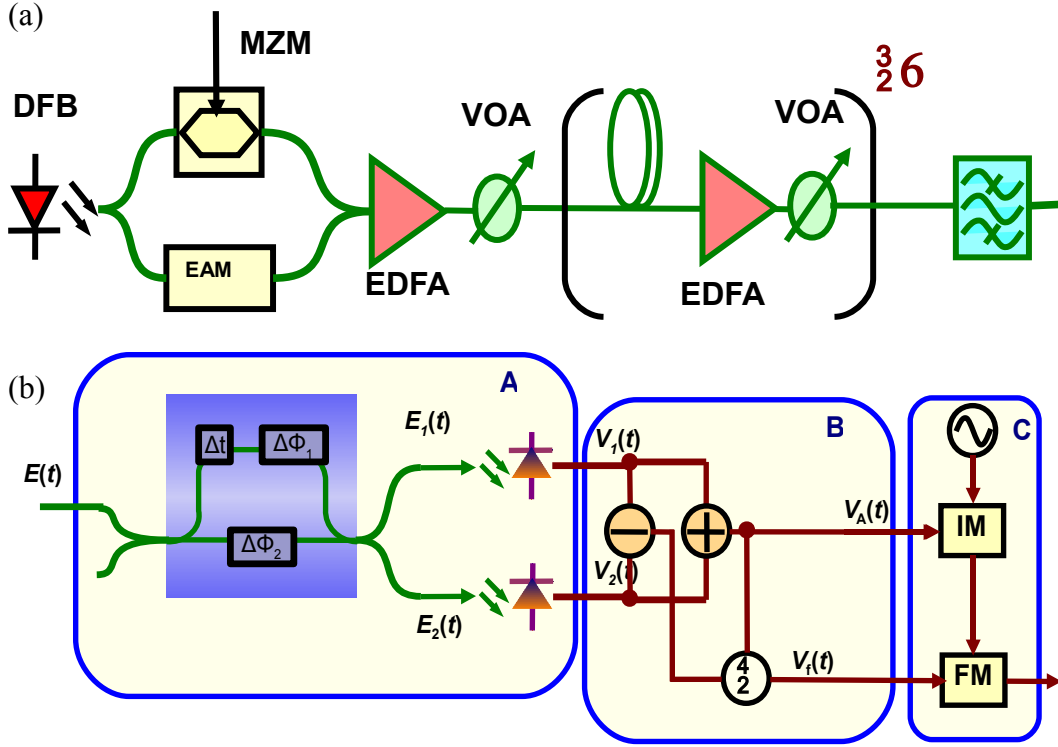
Figure 19: Block Diagram for VPI simulation (a) is the simulated transmitter and transmission link and (b) is the full field receiver structure. The transmitter may be an EAM or MZM. The fibre link is single-mode fibre. The signal is pre-filtered by an optical band pass filter. The receiver consists of an AMZI followed by direct detection of two electrical signals (A) which are processed (B) before a local oscillator is modulated with an image of the received signal E(t) (C)

3.5.1   System Simulation [ix]

The enhanced receiver shown in Figure 19 was simulated using VPI Transmission Maker v6.5. The transmitter encoded a continuous-wave (CW) optical signal with a 512 bit NRZ pseudo-random bit pattern. This study considers two different modulator types selected to emulate existing low cost transponders: an ideal Mach-Zehnder modulator (MZM) and a commercially available electro-absorption modulator (EAM). The MZM was simulated with a 10 dB extinction ratio and an alpha parameter of -1. The EAM was a 10 Gbit/s device designed for short reach applications (CIP-10G-SR-EAM) with measured parameters shown in Figure 20 and

53

21 at 1550 nm.
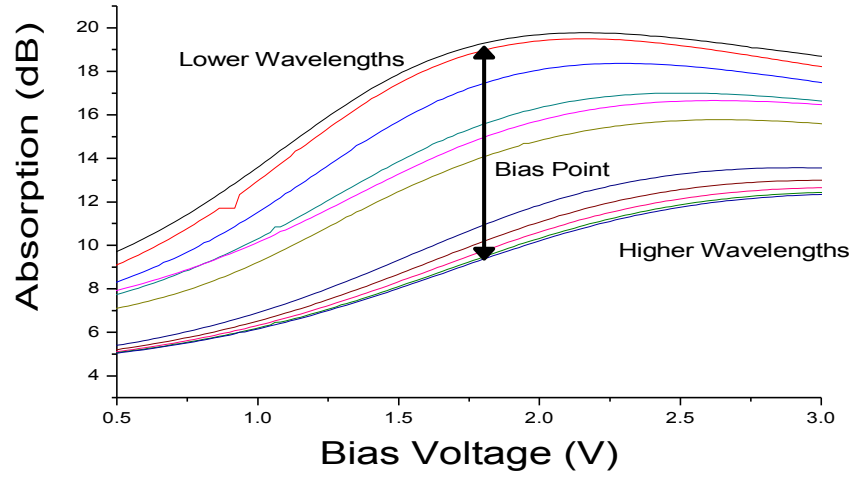
Figure 20: Absorption characteristic of an EAM as it changes with wavelength .
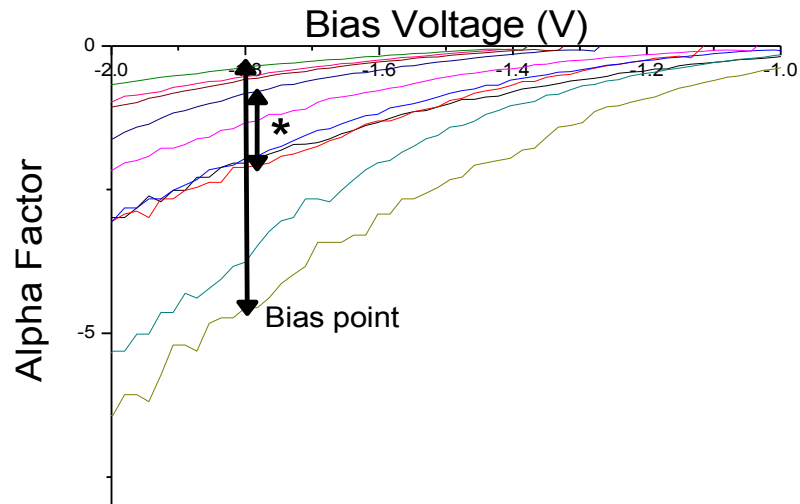
Figure 21: Chirp factor of an EAM versus bias point. The region indicated by the arrow with the star shows the range of chirp values for which the receiver offers less than a 1dB variation from the mean Q-factor.

 The modulated signal was transmitted with a launch power of 0 dBm over six spans of SMF (16 ps/nm/km dispersion, 0.2 dB/km loss). The amplifier in each span had a noise figure of 4.5 dB. Each span length was swept from 0 to 100 km, where a constant span loss of 20 dB using an optical attenuator is maintained. This resulted in

a fixed OSNR at the receiver of 25.3 dB.

Upon entering the receiver, the signal was pre-amplified and filtered using a 42 Ghz-bandwidth, third-order Gaussian optical filter. The amplified signal passed through the optical part of the receiver and the two voltages V_A and V_F were produced in blocks A and B (see Figure 19). Block B consisted of ideal adders and subtracters and Python (a software language) blocks for the more complex operations, such as division. The system was also band-limited to 8 GHz single sided bandwidth using appropriate filters.
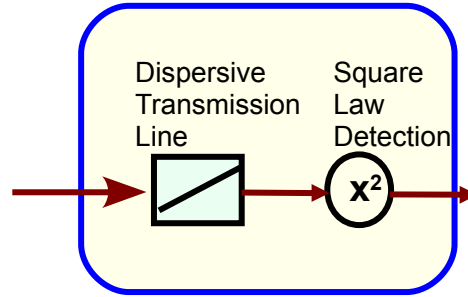
Figure 22: Example of Block D implementation (Linear Dispersion compensation).

Block C consisted of a high frequency oscillator, in this case a laser, which was modulated using ideal power and frequency modulators to generate the re-constructed signal. Linear dispersion was then implemented using an optical fibre module with no non-linearity or loss, the dispersion of which was approximately opposite to that of the transmission link. The resultant compensated signal was then square law detected using a standard photodiode followed by a Q-factor analyser.

3.5.2 Results

Using the approximation of linear AMZI frequency response in equation(32), Figure 23 illustrates the typical performance of the system described above for the two types of transmitter. The fibre transmission of block D is adjusted to 96% and

100% of the in-line dispersion, when using transmitters with the MZM and the EAM respectively.

All of the simulations assumed Enhanced-Forward Error Correction (E-FEC). This allowed for a Q-factor limit of 9.1 dB to allow for an error rate of $1*10^{-15}$ to be recovered. As can be seen in Figure 23, FEC alone extended the reach of the uncompensated modulators to ~140 km. The two types of modulator had a similar performance in the presence of FEC alone. However, after adding the dispersion compensation circuit, the detectable range of both transmitters was significantly extended. It is clear from Figure 23 that the compensator extended the transmission distance to at least 600 km for both transmitters. It appears that transmission distance with the EAM could easily be extended beyond this as the Q factor is still well above the FEC limit. This is 7* the dispersion limit; 4* dispersion limit with FEC and 3x direct detection dispersion reach for commercially available, receiver side dispersion compensation. Thus, it presents itself as a viable contender for EDC metro area applications.
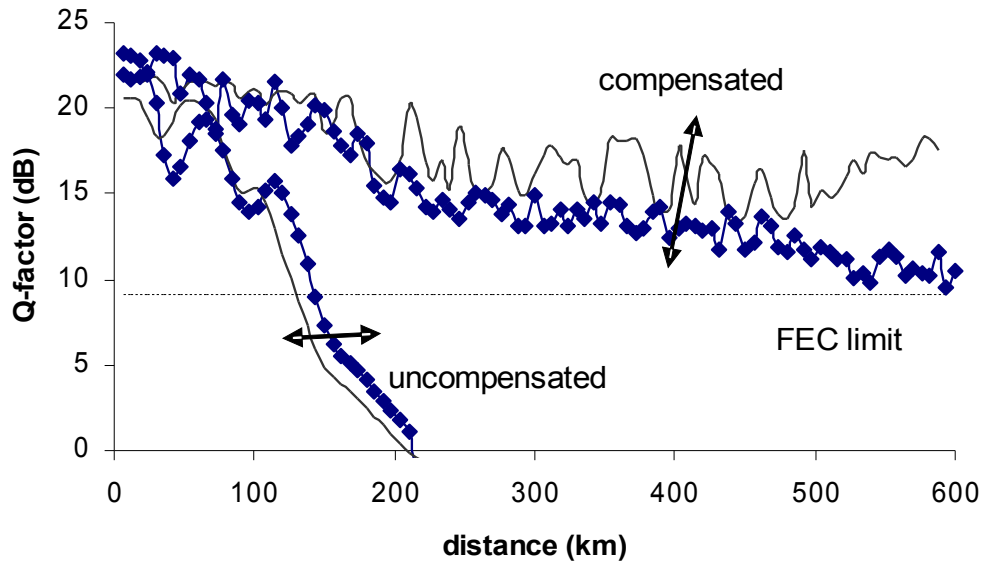
Figure 23: Q factor versus fibre span length without and with compensation for both EAM (line) and MZM (dots) based NRZ transmitters.

Illustrative eye diagrams for the EAM-based system are shown in Figure 24. The main source of distortion of the compensated eye is due to the limited bandwidths of blocks A and D (Figure 19 and 22), 12 and 8 GHz respectively, and the finite OSNR. The limited bandwidth is evident in the increased rise time of the signals and the noise added to the system can be seen in the thickening of the upper level of the eye diagram.
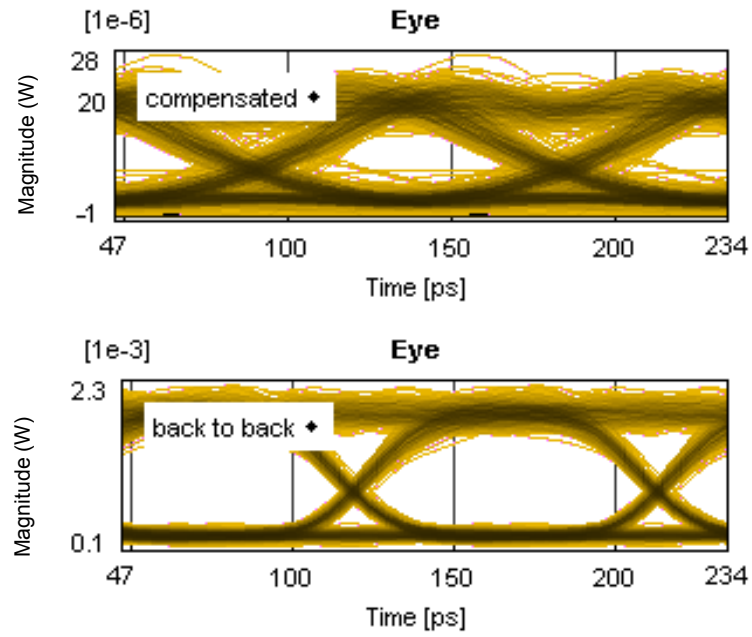
Figure 24: Eye diagrams for EAM based transmitter for 0 km transmission (0 km transmission) and after 600 km transmission of SMF-28 fibre (compensated)

3.5.3 Implementation Options

The main advantage of this technique is that once the signal has been reconstructed in the electrical domain, any linear dispersion compensating technique can be used. For example, transmission lines or an electrical (digital or analogue implementation) all pass filter can be used .
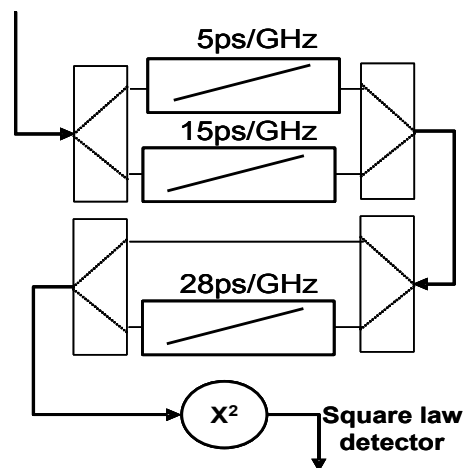
Figure 25: Schematic diagram illustrating fixed length transmission line receiver.

A transmission line is relatively large in size, ~cm, but is passive which saves on power. An all pass filter is small and can be integrated with FEC and other control electronics and it is adaptable, but it uses a lot of power. Transmission lines can be made more adaptable by using a number of transmission lines. An alternative approach to a continuously tunable transmission line is to use two or three fixed length transmissions lines (Figure 25), which can be combined in four different configurations to allow the transmitter to compensate dynamically for the entire range of signal with $0 - 9600$ ps/nm of accumulated dispersion. The Q-factor characteristic of the system is shown in Figure 26. This allows a Q-factor of greater than or equal to 9.1 dB for any span length up to 600 km. In order to introduce a margin to allow for degradation of the signal due to switching nodes etc., three or more transmission lines could be used. The more transmission lines used the greater the amount of overlap and, hence, improved performance. This should not affect the fast adaptability of the receiver if a simple BER monitor is used to flag when a different combination is required and the switches could be transistor based and so respond very quickly and cleanly. This will, however, require power at latching and will result in increased power consumption. Thus, there is a trade off between performance and power consumption.
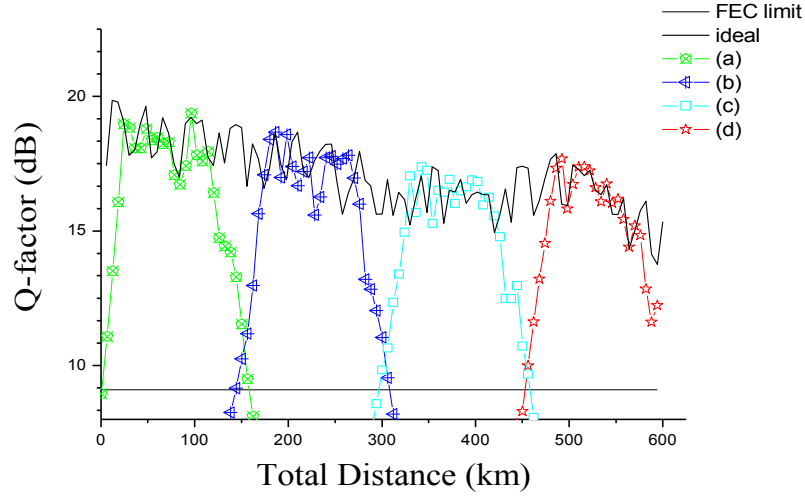
Figure 26: Performance of switched transmission line based compensation: (black) assuming ideal, continuously tunable transmission line, (green) 5 ps/GHz fixed transmission line; (b –dark blue) 5 ps/GHz + 15 ps/GHz transmission line; (c-light blue) 5 ps/GHz + 28 ps/GHz; (d-red) all transmission lines.

In order to implement Block B in either individual or integrated components, such issues as amplifier limitations and the complexity of realisation must be considered. In order to simulate amplifier saturation and limited bandwidth (Figure 27(b)) a cosine term is added to equation (28) and (32):

$$
\begin{aligned}
V_A &\uparrow \cos(V_1 \, \acute{G} \, V_2) \\
V_F &\uparrow \frac{V_2 \, \acute{H} \, V_1}{\cos(V_1 \, \acute{G} \, V_2)}
\end{aligned}
\tag{33}
$$

This causes only a slight degradation of the Q-factor.

The implementation of division in analogue circuits or as an algorithm in a DSP chip may be unstable or arithmetically intensive. This section investigates if the division can be neglected. Hence, the effect of neglecting the division is investigated and the result of these simulations is shown in Figure 27(c):

$$
\begin{aligned}
V_A &\uparrow \cos(V_1 \, \acute{G} \, V_2) \\
V_F &\uparrow V_1 \, \acute{H} \, V_2
\end{aligned}
\tag{34}
$$

This results in Q-factor curve without large fluctuations in degradation with distance.

60

This may have advantages such as allowing a simpler Q-factor eye diagram monitor.
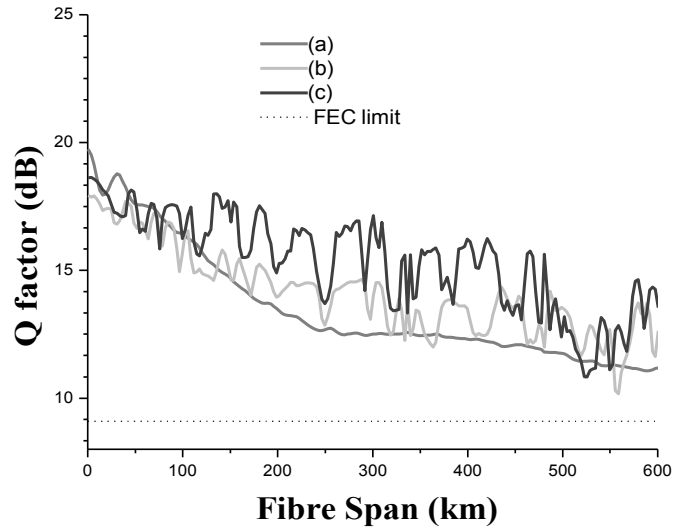
Figure 27: Q factor for simulated implementation of original reconstruction for (a), (b) is considering the effect of amplifier saturation and (c) is neglecting the division in the phase estimation path.

An experimental result of neglecting the division , as proposed here, is shown in Section 5.20 .

3.5.4   Wavelength Dependence Limit [ix]

The wavelength dependency of the link is mainly induced by the characteristics of the transmitter modulator and will be the most severe for an EAM based transmitter. The characteristics of a typical EAM were presented in Section 3.5.1 for a commercially available device and are shown in Figure 21. These characteristics of the 0 km transmission pulse shape and modulation depth of the signal are very significant and so would be expected to have a significant impact on the robustness to transmission impairments. However, the proposed EDC offers some immunity to the effects , as can be seen from Figure 28. The difference from the mean Q-factor at 600 km is still less than 1dB for a range of 17 nm at 1550 nm. At higher

61

wavelengths a penalty is introduced due to reduced absorption by the EAM and, hence, a small modulation depth in the signal. This can be seen from the slopes close to the bias point of the absorption of the EAM in Figure 21. This is consistent with the system being noise limited and the expected 0 km transmission modulation characteristics of the EAM.

The theory of the compensator assumes that the AMZI is a linear filter. The AMZI has in fact a sinusoidal response and, therefore, this is an approximation that will inherently degrade the accuracy of the reproduction of the signal. It was considered that this may make the system very sensitive to the point at which the interferometer is biased. This is a concern in metropolitan networks as these are extremely cost sensitive and, hence, the cheapest possible transmitter is required. This requires higher yield and, therefore, more variations in individual components.
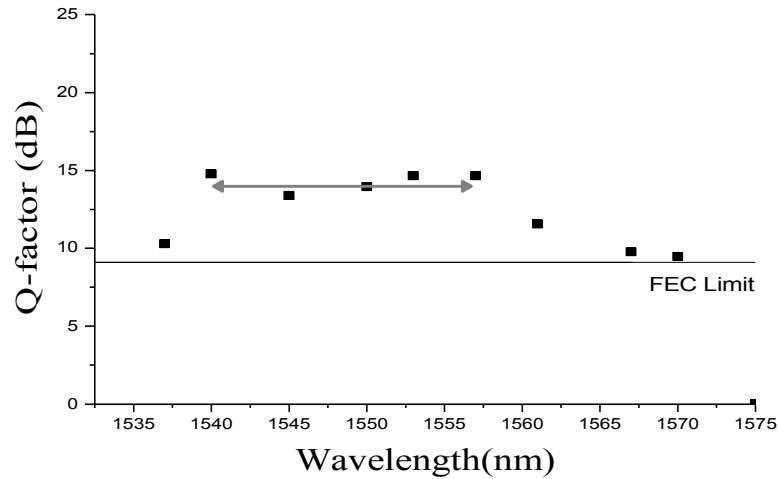
Figure 28 Q-factor after 600 km simulated transmission with respect to wavelength tuneablity. The arrow indicates variation of less than 1 dB for a range of 17nm at 1550nm

Hence, it is a great advantage if the receiver is insensitive to wavelength drift due to temperature change or due to wavelength reuse. By using simulations where the phase offset of one arm of the AMZI is swept through 180 degrees, the stability of

the linear filter assumption is explored. In Figure 29 the Q-factor results are shown. It can be seen that, even for compensating at 600 km, the receiver is very insensitive to the bias point of the interferometer. The Q-factor remains above the EFEC limit for all except the tails of the sweep. This corresponds with the dip and peak of the sinusoidal response where the slope approaches zero and no phase information is recovered. This indicates that the tuning time for the receiver should be almost instantaneous and makes it suitable to use in switched networks where wavelengths may change with transmit node. The compensation parameters were optimised assuming quadrature biasing. This is extremely important to allow EDC technology to compete with optical techniques as these are inherently broadband and, therefore, have the advantage that they can compensate seamlessly from one wavelength to the next if they are transmitted across the same link
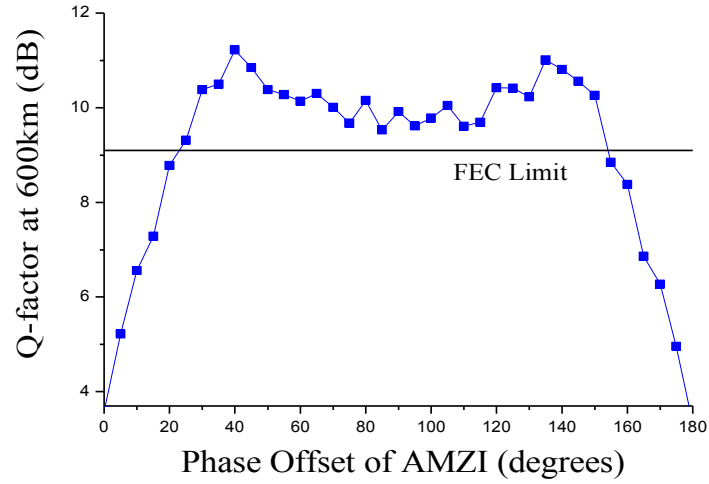
Figure 29: Q-factor plotted against varying φ in one of the arms of the AMZI.

3.6 Conclusion

In this chapter, the feasibility of utilising an AMZI as a frequency sensitive filter to cover the instantaneous frequency of a signal was illustrated. It was shown how this

can be incorporated into a novel and interesting receiver structure that can be used for dispersion compensation. The theoretical proof of principle was presented and preliminary simulation results were shown in order to highlight any major stumbling blocks. This technique will be compatible with existing metropolitan transmitters. It should also give sufficient reach for these applications with fewer electrical components compared to coherent detection. It can be tuned to work across the range of wavelengths without the need for a tunable local oscillator at the receiver as would be required for coherent detection. A possible practical implementation of FF-EDC using analogue components was presented which shows promise of working well beyond any direct detection method as described in Chapter 1. Chapter 5 will investigate, on a more fundamental level, the operation of the receiver and demonstrate it experimentally.

4 Experimental Set-Up and Optical Phase Reconstruction

4.1 Introduction

The characteristics of certain critical components used in the experiments may be expected to have an influence on the overall system performance. This chapter reviews the measurements of the components used in this work. For several component characterisations, such as fibre link, well known standard techniques were used and these are clearly referenced in the appropriate sections. For other components, known techniques proved time-consuming, cumbersome, and, in some cases, inaccurate for extreme parameter values. These include chirp characterisation of electro-absorption modulators, where the know dispersion measurement technique (4.3.1) was adopted to provide efficient and accurate characterisation, even for high values of chirp, in contrast to the small signal measurement [107].

In addition, a preliminary demonstration of field reconstruction is presented, using a high speed DFB laser to emulate a frequency modulator. At the time of writing, direct implementation using analogue RF circuitry was restricted by the low frequency modulation bandwidth of commercially available voltage controlled oscillators and IQ-mixer assemblies.

4.2 BT Link Characteristics

The transmission described in the following chapters is carried over installed SMF-28 fibre [108]. The use of installed fibre ensures that the results more accurately account for the practical fibre impairments likely to be encountered, including PMD, temperature fluctuations (delay and dispersion changes) and the excess losses and

reflections associated with an intermediate exchange. In this case, a fibre length of 124 km was used. The high total loss of the link results in a received OSNR considerably lower than normally encountered (40-80 km links would be considered) ensuring that the test conditions represent a worse case scenario for a metro area network. The fibre runs from the Tyndall National Institute in Prospect Row, Cork City to Clonakilty, West Cork, Ireland where it is doubled back to Cork along another fibre in the same cable. This gives access to six links of 124 km long loops of fibre. Other fibres are used to carry live traffic. The measured total losses using a CW laser at 1550 nm and a power meter ranged from 26 dB to 28 dB with an error margin of ±0.1 dB. The expected minimum loss for SMF is 124 km*0.2 dB/km = 24.8 dB. The length is taken from OTDR traces of the fibre but permission was not given to reproduce these in this thesis for BT Ireland operational reasons. The loss value is the average value for the type of fibre, SMF-28, deployed in this link [108]. The fibre links are terminated using SC flat connectors (subscriber connector) and looped back using patch cords at the remote exchange in Clonaklity. Also in Tyndall, SC to fibre connector-angled polished connector (FC-APC) adapters are used. These connectors account for the majority of the extra losses and affect the maximum achievable OSNR. It was not possible to measure the adaptor losses as the output of these was the agreed Tyndall access point. The fibre link that is used in this work for the recirculating loop described in Section 4.4 is the one with the lowest insertion loss of 26 dB.

4.3 Modulators

In this work two high speed amplitude modulators are used. In this section, the principle of operation of each is described briefly. The two most influential

properties of each are measured (chirp for electro-absorption modulators and extinction ratio for Mach-Zehnder modulators). The understanding and control of these parameters is key to the performance of each as a transmitter for full-field electronic dispersion compensation.

4.3.1 Electro-Absorption Modulator

A commercial electro-absorption modulator (EAM) was used for much of the simulation work presented in Section 4.3.1 . An EAM is manufactured from a material whose refractive index changes when an electrical voltage is applied due to the shift in the absorption edge. The resultant change in absorption can be used to on-off key modulate a CW light source, whilst the change in the real part of the refractive index results in unwanted chirp.

An EAM is a typical modulator used in metro area networks. It is small in size, has a relatively low operating voltage and can be integrated with the laser, factors which lead to a low cost footprint. It, however, has a chirp (α) factor which is non-zero. This factor varies with bias, wavelength and temperature. Chirp is an instantaneous frequency change in the modulated signal and, therefore, depending on its sign and value, it can either help or hinder transmission in SMF. It is, therefore, an important factor to measure. Figures 30 and 31 show how chirp varies with respect to signal wavelength and temperature for a commercially available EAM. These measurements were used to ensure the accuracy and relevance of the simulation results presented in Chapter 3.

(a)   (b)
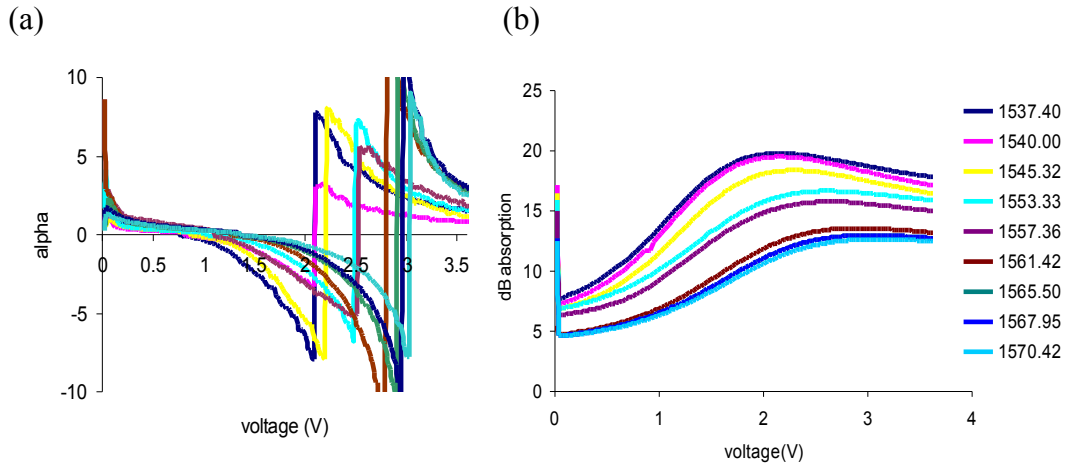
Figure 30: Alpha factor at 25 ° C (a) and absorption (b) vs bias voltage with respect to signal wavelength .

(b)
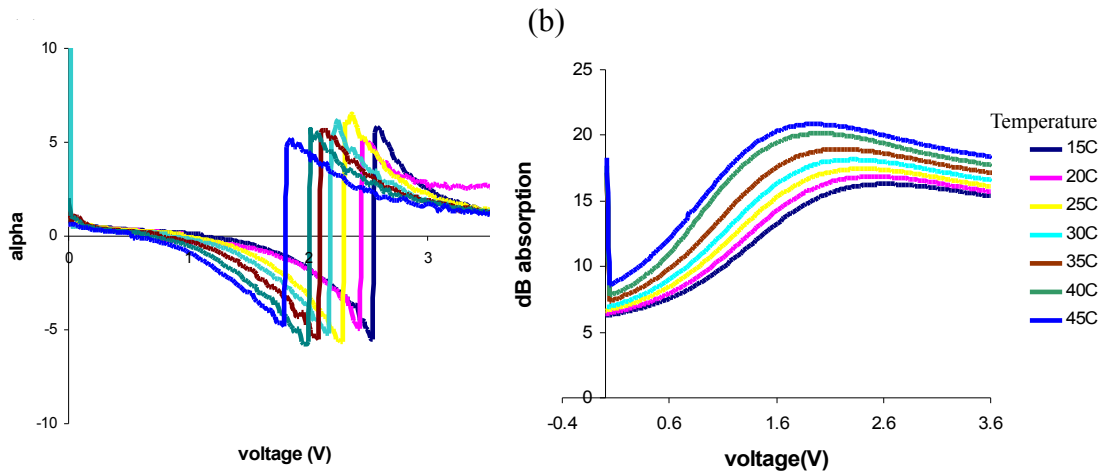
Figure 31: Alpha factor (a) and absorption(b) vs bias voltage with respect to temperature variation of the EAM at wavelength of 1550 nm.

4.3.2   Mach Zehnder Modulator

The operation of an asymmetrical MZI is described already inSection. For data modulation, however, a symmetric MZM is commercially available where the phases of the arms of the MZM are controlled by voltages so that interference at the output results in amplitude modulation. As shall be described in Chapter 5, the optical extinction ratio of the transmitted data is an important parameter in optimal

implementation of full field EDC. In order to experimentally confirm these predictions, it is essential to be able to accurately and simply set, measure and monitor the extinction ratio in the experimental implementation.

The extinction ratio of the MZM modulator can be controlled by manipulating the bias point and the drive voltage of the modulator. The easiest way to manipulate these parameters is to use the gain control voltage (V_{gc}) on the MZM drive amplifier. For low extinction ratios used in this thesis, the modulated signal power has an approximately linear relationship with the amplitude of this voltage. The measurement of extinction ratio is completed using a 43 GHz bandwidth photodiode and a calibrated 70 GHz scope – a sample measurement is shown in Figure 32.

The relationship between the output power and extinction ratio is shown in Figure 33. The measurement technique is not accurate for high extinction ratios due to the limited dynamic range of the oscilloscope. This is why the measured points at the apex do not follow the theoritical predictions (shown in blue dotted line). However, for extinction ratios in the region of <15 dB the relationship is approximately linear and is suffiently accurate for this work. Due to the non-linearity of the gain suppression mechanism of the amplifier, for the low extinction ratio results presented in section 5.4 , a 3 dB external fixed attenuator is used to improve the quality of the drive signal. The corresponding peak to peak voltage (V_{pp}) is applied and the extinction ratio is as expected for the same output power. The modulator is biased at quadrature.
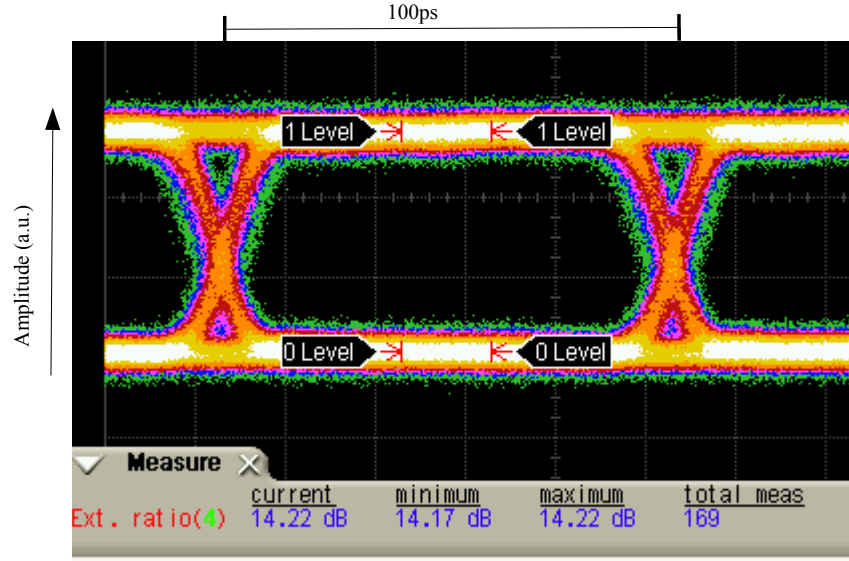
Figure 32: Example of measurement of extinction ratio for gain control voltage , V_{gc} =5.5.
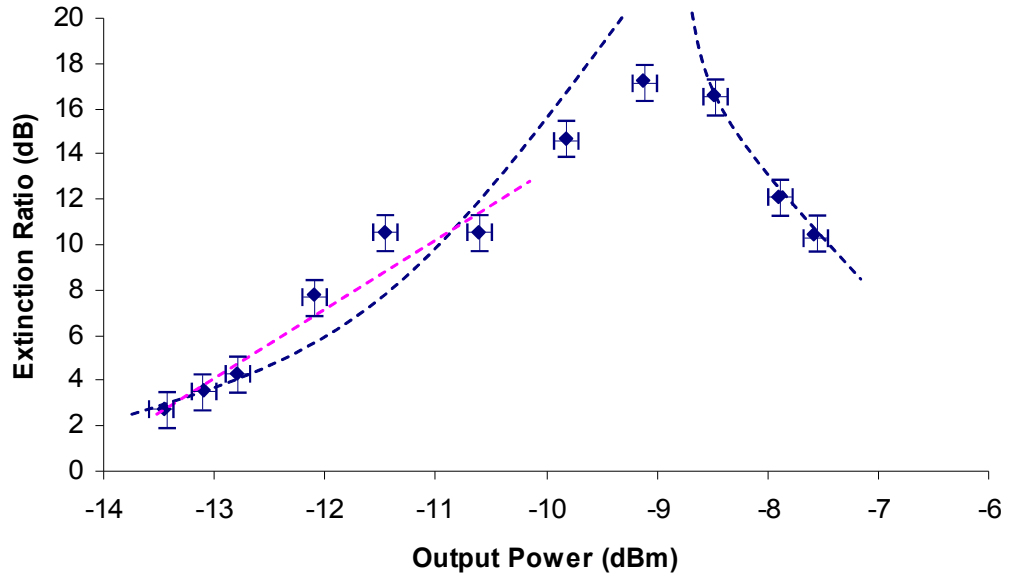
Figure 33: Extinction Ratio of MZM modulated data versus output power monitor (points) measured, (blue dashed) fitted theoretical curve and (pink dashed) linear approximation for region of interest.

The extinction ratio, R, is defined as the power in the zero level (P_0) divided by the power in the one level (P_1). One can consider a typical co-sinusoidal transfer function of the MZM as shown in Figure 34
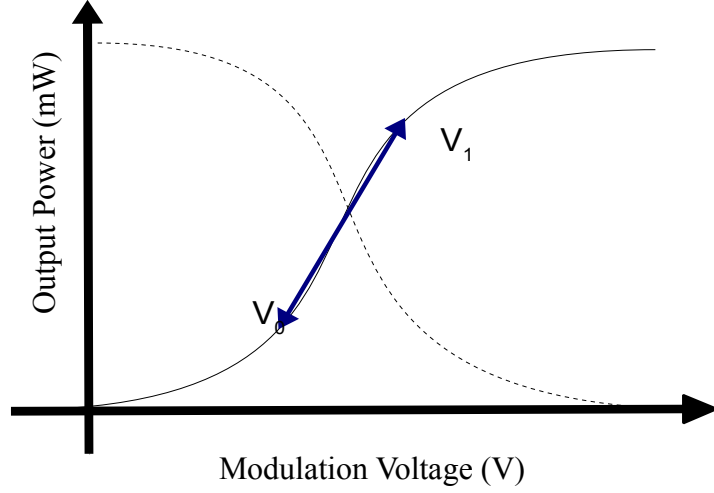
Figure 34: Schematic of MZM transfer function.

It is straightforward to show that

$$R=\frac{P_0}{P_1}=\left(\frac{\cos(V_o-V_{dc})}{\cos(V_1+V_{dc})}\right)^2 \quad , \tag{35}$$

where V_0 and V_1 are the applied voltage for a data logic values of '1' and '0' rephrase

respectively, and V_{dc} is a fixed offset. Defining a peak-peak drive voltage

$V_1-V_0=V_{pp}$, gives

$$\sqrt{R}=\frac{1+\cos(V_{dc}+\frac{V_{pp}}{2})}{1-\cos(V_{dc}+\frac{V_{pp}}{2})} \quad . \tag{36}$$

Assuming that the modulator is biased at quadrature $V_{dc}=\frac{\pi}{2}$ then

$$\sqrt{R}=\frac{1+\sin(\frac{V_{pp}}{2})}{1-\sin(\frac{V_{pp}}{2})} \tag{37}$$

which, at low V_{pp}, may be simplified to

$$\sqrt{R}=\frac{1+\frac{V_{pp}}{2}}{1-\frac{V_{pp}}{2}} \quad . \tag{38}$$

Equation (38) may be further simplified using the Taylor expansion

$$\sqrt{R} \approx \left(1 + \frac{V_{pp}}{2}\right)\left(1 + \frac{V_{pp}}{2} + \left(\frac{V_{pp}}{2}\right)^2 - \ldots\right) \tag{39}$$

$$\Rightarrow \quad \sqrt{R} \approx \left(1 + \frac{V_{pp}}{2}\right)^2 = 1 + V_{pp} + \frac{V_{pp}^2}{4} \approx 1 + V_{pp} \quad . \tag{40}$$

This results in

$$R \approx (1 + V_{pp})^2 = 1 + 2V_{pp} + V_{pp}^2 \quad . \tag{41}$$

Considering the dB value of extinction ratio

$$10\log_{10} R \approx 10\log_{10}(1 + 2V_{pp}) \quad . \tag{42}$$

Thus, if $V_{pp} \ll 1$

$$XR_{dB} \propto V_{pp} \quad , \tag{43}$$

This indicates a linear relationship between the extinction ratio and the peak-to-peak modulation (V_{pp}) for small $V_{p.}$ For small V_{pp}, the modulated power output is also directly related to the amount of modulation. This relationship is illustrated by the pink line shown in Figure 33.

4.4 Loop Configuration

In order to demonstrate dispersion compensation over a distance sufficient for electronic dispersion compensation for metro area networks, a link of greater than 120 km is required. Due to the limited number of available optical amplifiers, a recirculating loop was employed in these experiments. Recirculating loops have been used to emulate long distance transmission since the early 1990's [109-114]. The schematic diagram of the set-up used for this work is shown in Figure 35.
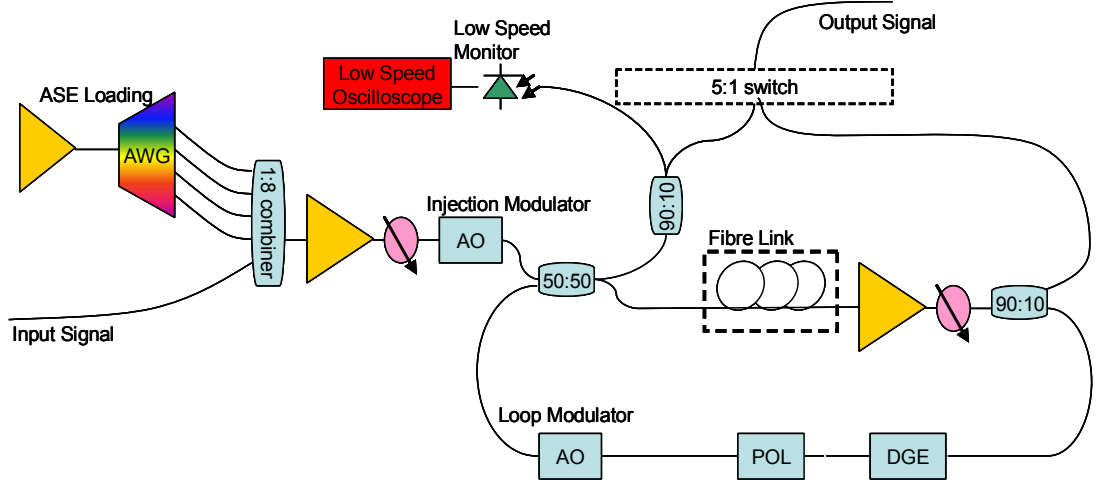
Figure 35: Schematic Diagram of Recirculating Loop Set-up (ASE amplified spontaneous emission, AWG arrayed wave-guide grating, AO acousto-optical modulator, POL polarisation scrambler, DGE dynamic gain equaliser).

The basic elements of a recirculating loop are a pair of acousto-optic modulators (AOM) and a 50:50 coupler. One modulator is the injection modulator, which is 'open' or set to low attenuation to allow fresh data into the loop for a time period. This time must be greater than the flight time of the fibre (600 μs for 120 km of fibre) to prevent dead times where there is no data present at the input to the loop amplifier. This would result in amplifier power transients. The loop modulator is conversely set to high loss at this stage to clear the loop of the previous data. The injection modulator is then in a 'closed'/high attenuation state to prevent new data entering the loop as this would interfere with the circulating signal. Simultaneously, the loop modulator is set to 'open'/low attenuation to allow the data to circulate around the loop. Acousto-optical modulators (AOMs) are chosen because of their fast response (~200 ns), deep absorption (extinction ratio in the order of 60-70 dB) state, low polarisation dependence (<0.1 dB) and low insertion loss (3 dB) [114]. The number of times that the data is allowed to circulate around the loop depends on the length of time that loop modulator remains open. In this work, it is generally set to

seven, which is equivalent to $7*124\text{km} = 868\text{km}$. This allows for various reaches to be investigated using the same loop parameters. The inject time was set to $6.18*10^{-6}$ s. Therefore, the number of circulations which have occurred is given by

$$
\begin{aligned}
No\ of\ circulations &= floor\left(\frac{(delay\,time - inject\,time)}{flight\,time}\right) \\
&= floor\left(\frac{(delay - 6.18*10^{-4})}{6*10^{-4}}\right)
\end{aligned}
\tag{44}
$$

The power evolution of the signal as it circulates is monitored by a low speed monitor consisting of a low speed photo diode and a low speed real time sampling oscilloscope. It is important to keep the power levels as consistent as possible to (a) keep the launch power for each span the same and (b) prevent very high powers at certain reaches as this would result in non-linear effects and component damage. This is done by balancing the amount of total launched power using the loop amplifier and variable optical attenuator (VOA) pair.

Note that, in loop operation, the natural state of the EDFA is constant power mode; therefore, the total power after each circulation is capped. Amplified spontaneous emission (ASE) is accumulated with each circulation and, as a result, available power to the signal will gradually be reduced. A dynamic gain equaliser (DGE) is employed to prevent the ASE accumulation. This is a programmable wideband filter which filters out-of-band ASE. These are often used in real systems, especially in WDM systems, to compensate for amplifier tilt. The DGE profile used here is of a constant minimum attenuation and wide enough that it does not affect the signal and co-propagating signals even after several passes. Figure 36 shows the 0 km transmission signal in 0.1 nm resolution, a signal after one pass through the fibre and DGE with the profile too narrow (notice the tight filtering of the ASE signal) and

74

then a signal after two passes which does not affect the propagated signal. If the DGE is too narrow, an OSNR penalty will be introduced by filter concatenation effects. If the DGE is too wide, too much ASE will be allowed to propagate in the loop and this will also result in poor performance by leaching power away from the signal.
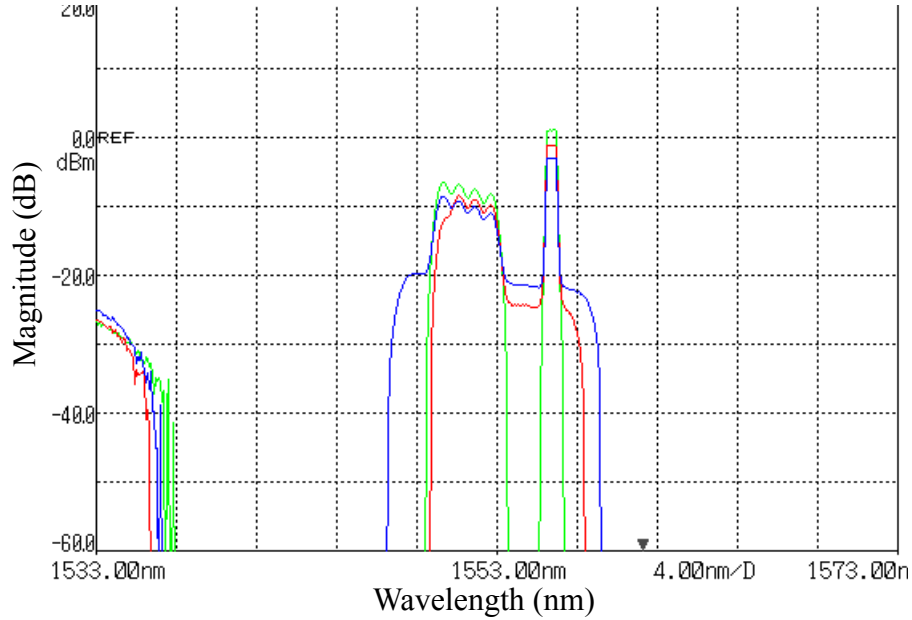
Figure 36: Signal and co-propagating ASE (green), 0 km transmission(red), 1 loop DGE too narrow, and (blue) 2 loops with DGE profile from above.

The EDFAs used in the loop are designed to have sufficient gain to amplify a fully populated C-band WDM transmission with a span loss of 20 dB and output power of 23 dBm. It is important that the gain of the loop is less than unity at all wavelengths to prevent the loop lasing at this wavelength. Hence, they are far too powerful for our application although a small degree of amplifier saturation is beneficial to maintain loop stability. As the link length is so long, our transmission is expected to be OSNR limited. It is not practical to reduce the EDFA gain by reducing the pump current as this would result in an amplifier noise penalty. In order to achieve the maximum OSNR in these conditions, it is necessary to populate the EDFA with dummy channels to achieve the desired saturation gain. This experiment co-propagates

simulated channels along with our signal of interest. For simplicity, bands of ASE were propagated with the signal. The output of an EDFA is passed through a 100 GHz AWG (Figure 37) andthis allows control of the amount of co-propagating signal. 3.5 nm of ASE are propagated along with the signal and the overall spectrum in illustrated in Figure 38.
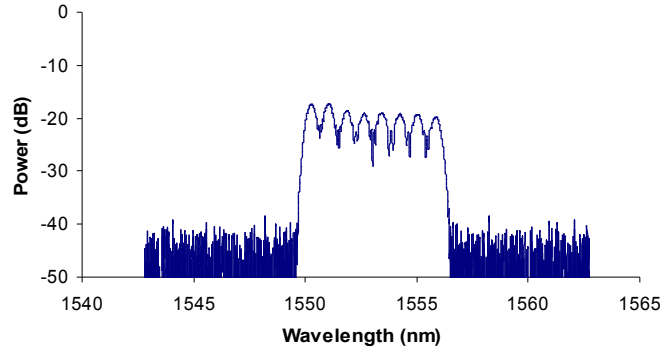
Figure 37: Output of AWG showing bands of ASE.

In order to view eye diagrams, take error rates, or capture data, a trigger signal, which corresponds to the time delay from the loop injection point to the required circulation, must be generated. The devices must be set to respond to a gated trigger. The width of this trigger is also important. If it is too narrow, it will result in insufficient data being acknowledged by the oscilloscope or error rate system.
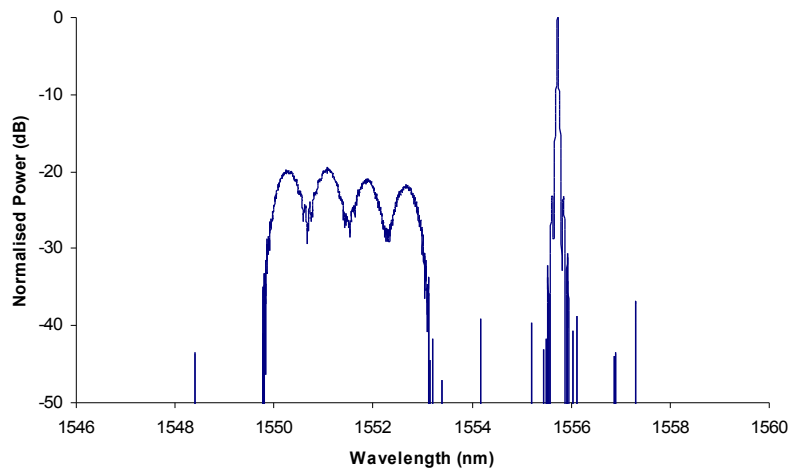
Figure 38: Signal and co-propagating band of ASE.

76

One of the known difficulties when using recirculating loops is to randomise polarisation. It is important to have the polarisation changing randomly and for this purpose a a polarisation scrambler (POL) is used. It would, however, be difficult to generate a trigger pulse which corresponded to each circulation, so the polarisation rotation is changed for every injection such that the progression around the Poincaré sphere is identical from circulation to circulation, but different paths around the sphere are considered for each injection. This is not ideal as, in a real system, the polarisation rotation of each link would be different. It does, however, mean that for each measurement the polarisation is changed and random. This is beneficial to ensure that the PMD distribution is approximately Maxwellian, as expected from point-to-point link.

4.5 Optical Phase Estimation [ii]

This chapter describe the various optical components and the primary experimental set-up which will be utilised in this work. This section describes preliminary tests of the overall concept presented in this thesis. The practicality of phase estimation in the presence of device imperfection and signal noise is tested. It is demonstrated that it is possible to reconstruct the instantaneous frequency from the output of a frequency sensitivity filter – an AMZI. In addition, the experiments reported here demonstrate a novel opto-electronic wavelength converter for phase modulated signals. To simplify the system, a differential phase shift keying (DPSK) signal is used, i.e. the phase is modulated and the amplitude remains constant, allowing for the omission of amplitude detection and the necessity for the division operation .

The experimental set-up is shown in Figure 39. The 10.7 Gbit/s DPSK signal is generated using a wideband phase modulator and a tunable laser. The OSNR of the

signal was degraded by attenuating the input to a fixed output power fibre amplifier. The input stage of the converter comprised a 0.8 nm channel selection filter and a planar silica AMZI with a free spectral range of 85.2 GHz , followed by a balanced detector with a 42 GHz bandwidth.
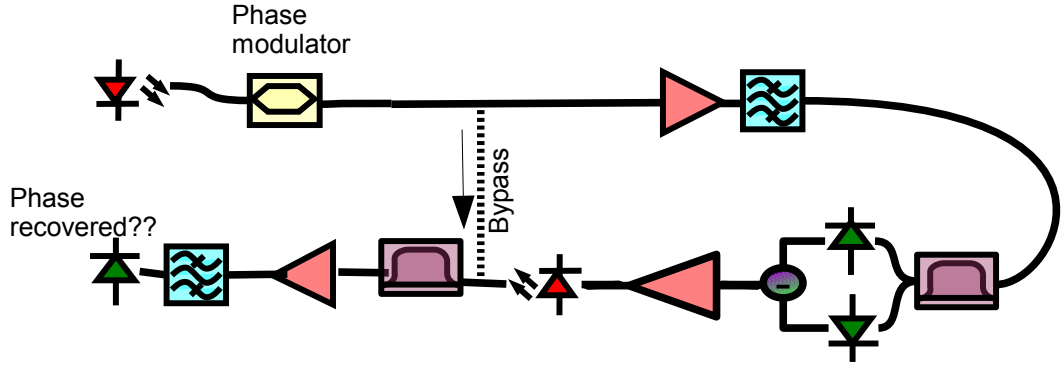
Figure 39: Optical phase estimator demonstrator.

This is followed by a linear electrical amplifier chain which directly drives a commercially available 1551 nm DFB laser with an 18 GHz bandwidth. The output of the electrical amplifier chain is shown as an eye diagram Figure 40(c) and a pulse pattern in Figure 40 (d), which shows positive (negative) going pulses corresponding to transitions from a phase of zero to π (π to zero), and a constant DC level corresponding to constant phase. The amplitude of the positive (negative) going pulses is chosen to give a net phase shift of π (-π) when applied to the laser [138]. Both the unconverted and converted DPSK signals were optically pre-amplified, filtered using a 0.64 nm filter and demodulated using a 1-bit AMZI followed by single ended direct detection. The receiver sensitivities at a BER of 10^{-9} were determined at the pre-amplifier output. The received eye (constructive port) is shown in Figure 40(b) for the converted eye and Figure 40(a) for the unconverted eye.
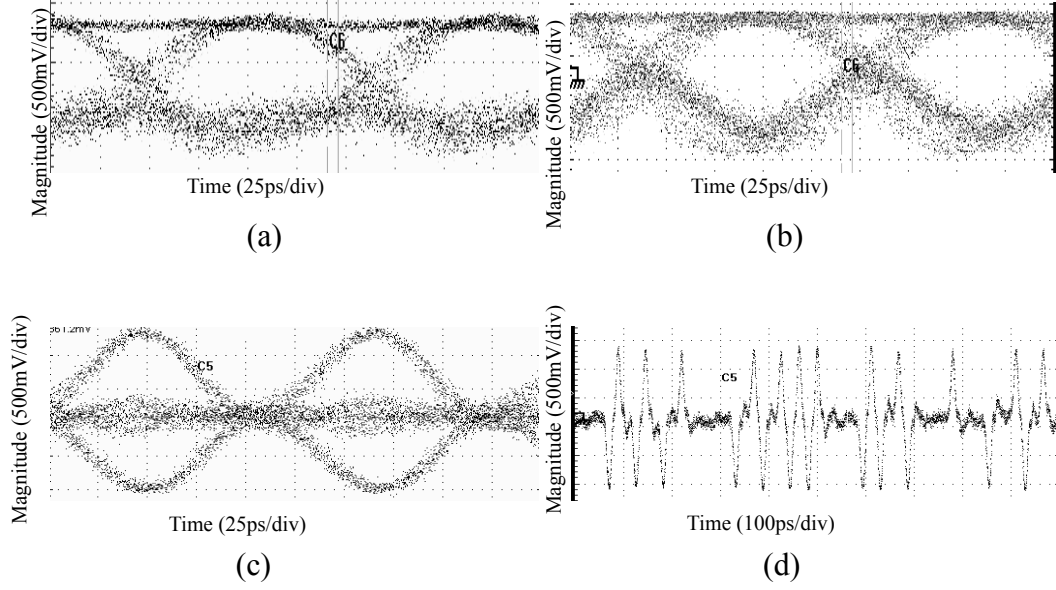
Figure 40: Eye diagrams and pulse patterns for DPSK reconstruction.   (a) transmitted signal, (b) recovered signal, (c) output of AMZI and (d) the amplitude of received signal at converter .
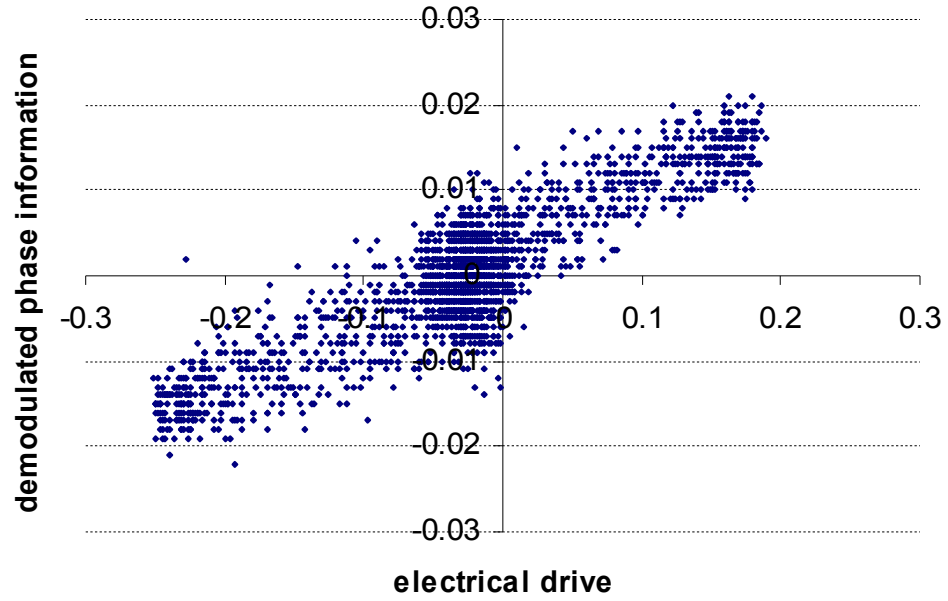
Figure 41: Demodulated phase information vs electrical drive of NEL.

To ensure that the NEL laser phase is being modulated by the estimated phase correctly (Figure 41), the demodulated phase is compared to the electrical drive signal used to modulate the NEL. As can be observed, this results in a linear relationship. This confirms that the NEL has sufficient bandwidth to be modulated

with a 10 GHz signal. If the bandwidth were insufficient, it would be evident from a tail off in the extremes – a saturation at either end – and the relationship would not be one to one. This would result in patterning effects. Figure 42 shows that, for powers less than -35 dBm, an error floor develops. For low OSNRs amplitude noise at the input to the phase estimator is converted into phase noise, whilst for higher OSNRs, the penalty from residual (unwanted) amplitude modulation is small.
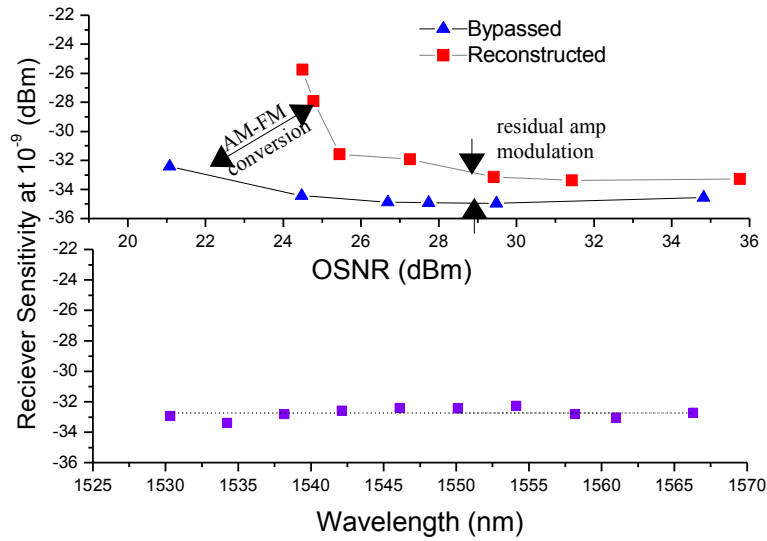
Figure 42: BER at 10^{-9} (Top) with respect to received OSNR (Bottom) with respect to wavelength.

Figure 43 shows the by-passed spectrum and the transmitted spectrum at the receiver. The limits due to the electrical bandwidth of the estimator can be seen. The bandwidth is limited to 15 GHz by using an amplifier with a Bessel shaped response, which is optimum for optical transmission. It can be seen from the the figure that, while the bandwidth of the recovered signal is limited, nevertheless, the signal is faithfully replicated onto the laser. The DFB laser was centred at 1551 nm and had an 18 GHz bandwidth. The system was very sensitive to both the bandwidth and the gain of the electrical amplifier chain in order to achieve the correct modulation of the

NEL laser. Due to the limited number of amplifiers available, it was difficult to experimentally examine the effect of different amplifier bandwidths, but, using the VPI model presented in Section 3.5 , 15 GHz is shown to be approximately optimum.
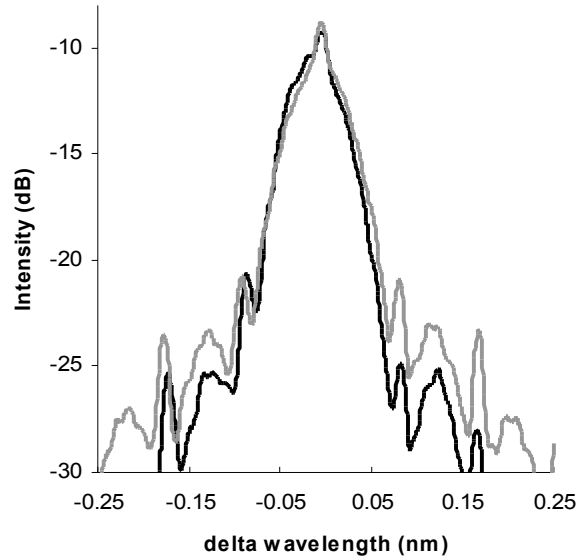
Figure 43: Shifted optical spectrum of bypassed(grey) and phase estimated signal(black).

4.6 Phase Estimation and Amplitude Reconstruction as Mid Span Spectral Inversion

In this section, the amplitude is detected and used in the field reconstruction. The ability of the amplitude and phase reconstruction to enable dispersion compensation is demonstrated (schematic is shown in Figure 44). In particular, the dispersion compensation is implemented by passing the reconstructed signal through a dispersive fibre with approximately the same amount of dispersion experienced by the signal detected by the receiver (Figure 45). Whilst the primary purpose of this experiment is as an electro-optical demonstrator to verify the concept of full-field reconstruction as a step to dispersion compensation, it is noted that this set-up

performs as an opto-electronic mid-span spectral inversion (Figure 46).
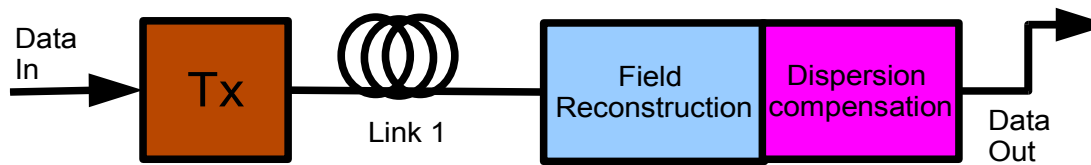
Figure 44: Schematic of concept to be verified.
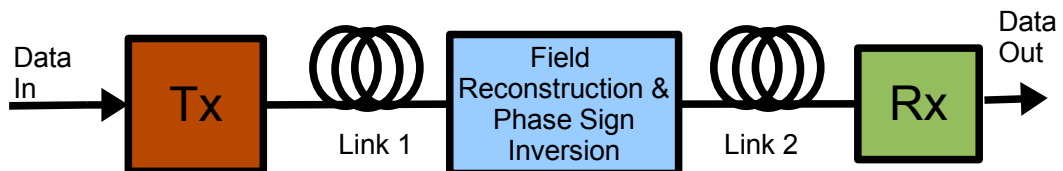
Figure 45: Schematic of Mid-Span Spectral Inversion.

The implementation is shown below. The transmitter may be an EAM or MZM - it will be specified with the results. The signal is reconstructed and then retransmitted onto a fibre link. The phase is reconstructed onto the laser directly and the amplitude information is encoded using a MZM modulator. It is then detected using a single photodetector.
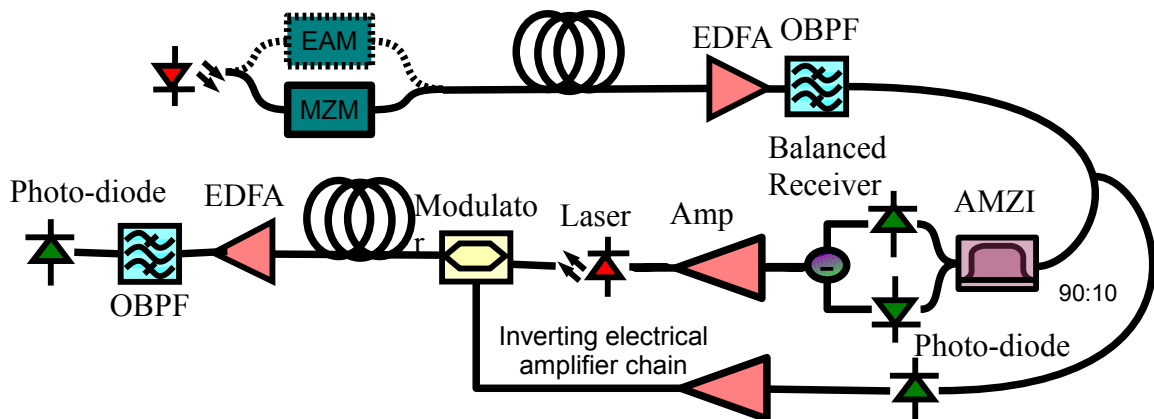
Figure 46: Block Diagram of mid span spectral inversion using phase estimation.

In order to make maximum use of the available fibre lengths, the system was set up using a single fibre so that the dispersion could be more easily matched and the same optical amplifiers could be used. This is shown in Figure 47.
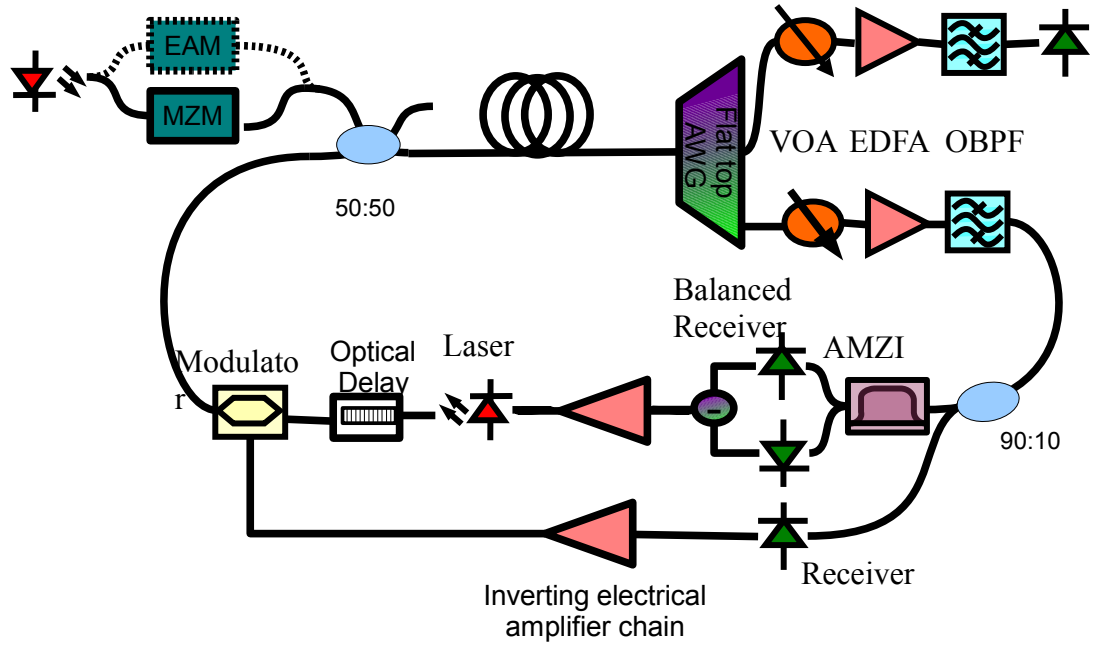
Figure 47: Block Diagram of phase estimation and amplitude compensation as mid span spectral inversion.

It consists of an NRZ 10.7 Gbit/s signal generated by external modulation of a tunable laser by a commercially available EAM as described in Section 4.3.1 . This is launched into fibre link through a 50:50 coupler. Two links were considered: an 80 km link of Corning SSMF fibre on shipping drums and installed optical fibre provided by BT Ireland (details in Section 4.2). The launched signal was co-propagated with the reconstructed signal generated by the field reconstruction node. The two signals were separated at the receiver/phase estimator using a flat top AWG which is temperature tuned. The tunable laser was tuned to 1550 nm and the NEL laser was 1552.7 nm. The OSNR of the received signals was degraded by a VOA, amplified and then filtered by a 0.8 nm filter and then split by a 90:10 coupler. The 90% tap passed through the AMZI biased at quadrature followed by the commercially available 40 GHz balanced detector. This was used to modulate the frequency of the NEL laser via a carefully selected series of electrical amplifiers and

attenuators to ensure correct scaling of the signal. The 10% tap is detected by a 10 GHz receiver. This configuration was used to simplify the practical delay and magnitude matching and must be done when this was implemented experimentally using individual components. Figure 48 shows the output of the balanced detector and single photodetector after 50 km. These are not time-aligned.
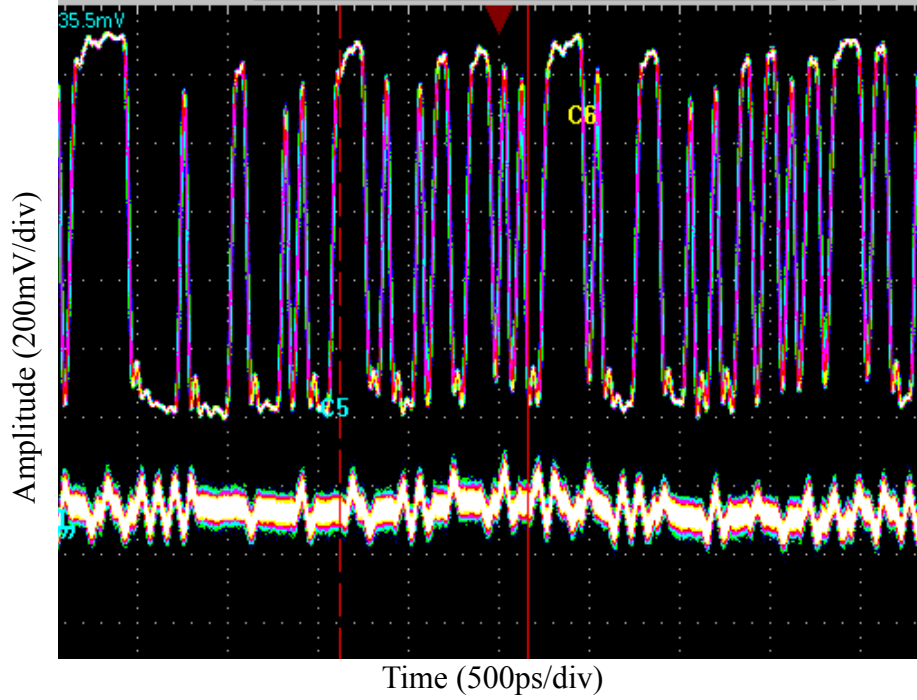
Figure 48: Amplitude drive (top) Phase drive (bottom) after 50km transmission.

The amplitude is encoded using a 40 GHz electro-optic polarisation modulator. The operation is described in [139]. An optical delay line with a resolution of ±1 ps was inserted between the NEL laser and the modulator to align the amplitude and phase signal. This was set by transmitting an isolated '11111' pattern. This results in a signal in both paths. The alignment is finely tuned by minimising the error rates. The signal is then propagated along the same fibre in order to undo the imposed dispersion effects. After the AWG, this signal is sent to a standard pre-amplified direct detection receiver with a filter of 0.64 nm and the bit error rate of this signal is measured using

a 10G BERT including a phase lock loop clock recovery unit.

4.6.1   Fibre Link 1

The spooled fibre consists of Corning standard single mode fibre. It consists of drums of various lengths < 50 km (Figure 49). This allows for the use of mid span amplification to maintain OSNR to give good performance.
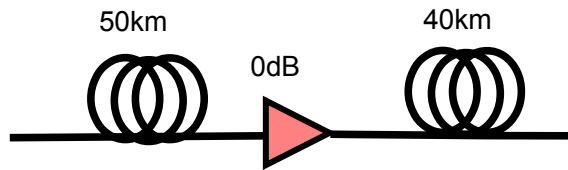
Figure 49: Block Diagram of 90 km span of spooled fibre used

As can be seen from Figure 50, by re-transmitting the amplitude information only – not phase modulating the NEL laser - the sensitivity is -31.6 dBm but introducing the phase modulation the sensitivity is reduced to -34.6 dBm. This is the same as for the 50 km span and only 2.2 dB penalty compared to 0 km transmission without the converter. This result represents transmission over 180 km with only a 2.2 dB penalty and, as will be shown on Figure 50, the majority of this penalty is due to imperfections in the implementation of the converter. Figure 51 shows the eye diagrams for the signal reconstructed using (bottom) only amplitude reconstruction and (top) using both after 180 km transmission using mid span spectral inversion. The eye opening is significantly improved and the eye shape showis less transmission effects (top) is more symmetrical than (bottom) the uncompensated eye.
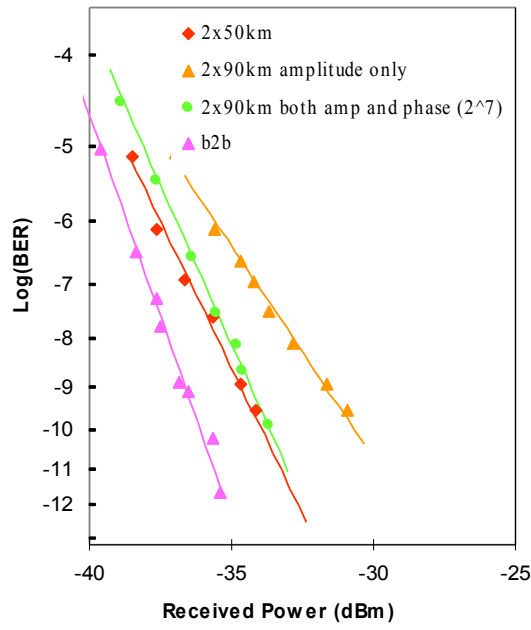
Figure 50: BER curves for 2^7-1 PRBS for fibre link 1
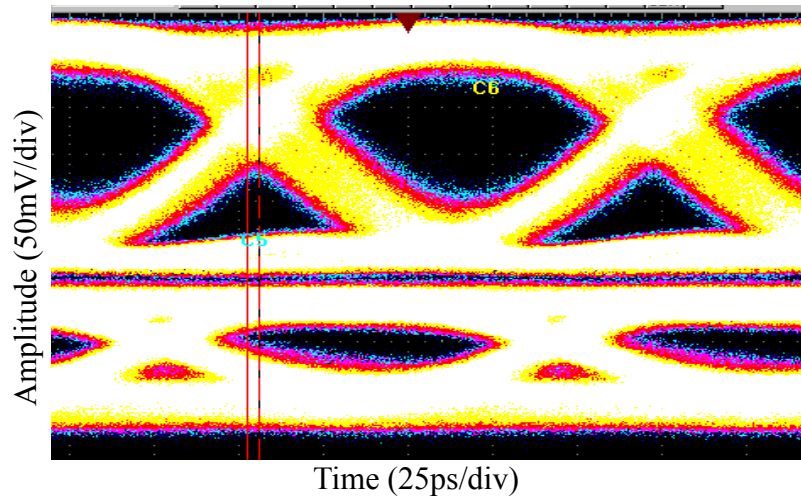
Figure 51: Eye diagrams with phase and amplitude reconstruction (top) and amplitude only (bottom) after 180 km.

4.6.2   Fibre Link 2

The laboratory fibre was replaced by an installed fibre of 124 km, the properties of

which are described in Section 4.2 . This greatly limits the power and OSNR available at the receiver. This stresses the sensitivity of the reconstruction to noise in low OSNR situations. The transmitter was changed to a 40 GHz Mach-Zehnder modulator to allow for an error free signal to be transmitted over the 124 km installed fibre link. The EAM could not achieve error free performance over this distance. Figure 52 shows the BER curves for the mid span spectral inversion.
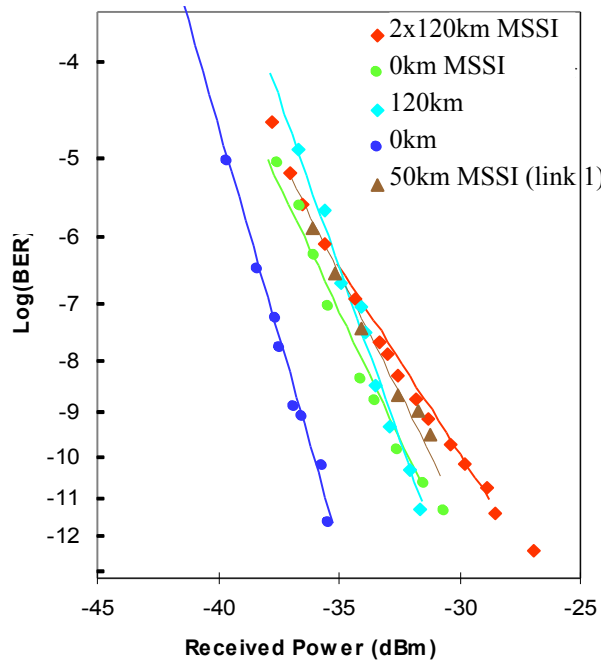
Figure 52: BER curves comparing MSSI for 240 km and 0 km transmission including 0 km transmission performance with and without the converter to observe the intrinsic penalty due to the converter.

The blue and green curves show the 0 km transmission curves with and without the mid span reconstruction, respectively. There is a 3.5 dB penalty without introducing any transmission. There is also a 3.6 dB penalty (light blue) compared to 0 km transmission for 120 km transmission followed by direct detection. With mid span spectral inversion using the full field reconstruction (red) a 5.4 dB penalty is

observed for a complete transmission of 240 km. If the 0 km transmission penalty is considered then the penalty introduced by transmission is only 1.9 dB. If this system were integrated, the 0 km transmission penalty would be reduced. The results for 50 km spool fibre mid span spectral inversion (total 100 km transmission) are shown in brown - these also show the same penalty with respect to 0 km transmission. This suggests that the penalty is dominated by imperfections in the converter, rather than the effects of dispersion or OSNR. Figure 53 shows the eye diagrams as detected by the direct detection receiver. The noise introduced by the reconstruction can be seen clearly by comparing it to the eye diagrams in Figure 54 which represent the signal reconstructed without transmission. The transitions are significantly thickened. This is due to jitter induced in the signal.

Figure 55 shows the received eye diagrams for a received power of -38.7 dBm . The effects of dispersion can be clearly seen in the shaping of the eye diagrams. Figure 56 shows the signal after midspan spectral inversion transmission of 248 km, the introduced noise is evident but note also that the symmetrical shape of the eye has been restored indicating that the effects of dispersion have been mitigated.

Time (25 ps/div)
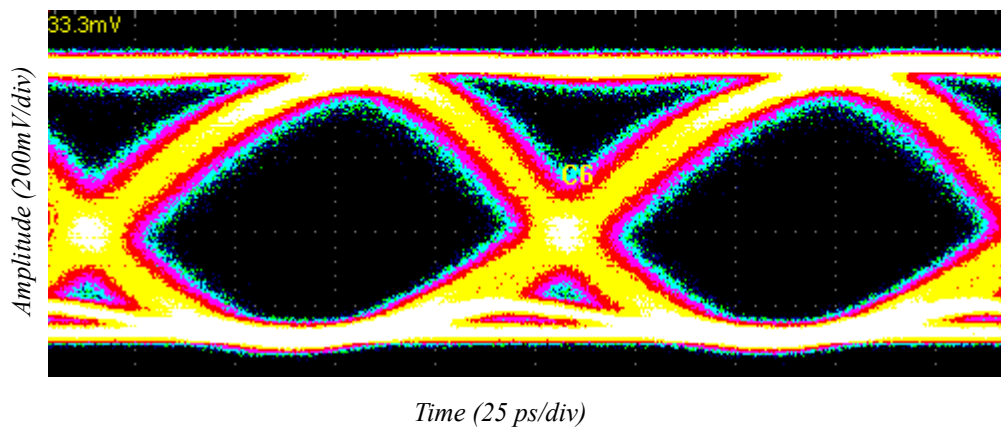
Figure 53: 0 km transmission using a 2^{31}-1 PRBS and received power of -34.5dBm.
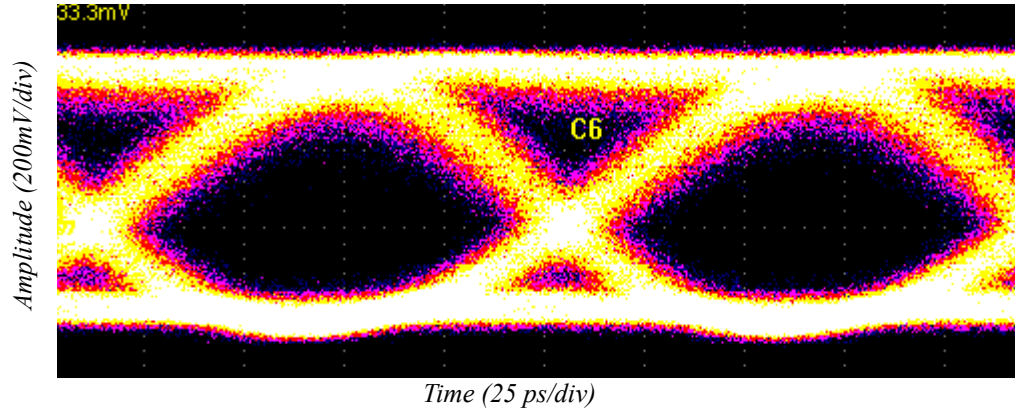
Figure 54: 0 km transmission including the mid-span spectral inversion using a PRBS of 2^{31}-1 and a received power of -36.5 dBm .
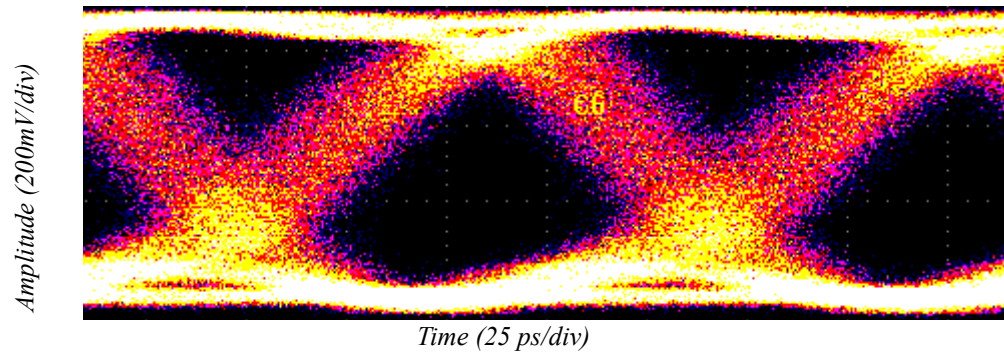
Figure 55: 124 km direct detection 2^{31}-1 PRBS and received power of -38.7 dBm.
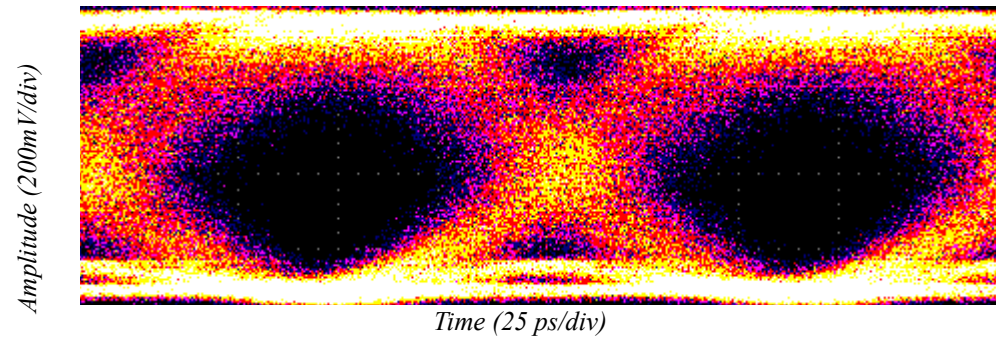
Figure 56: 248km with midspan spectral inversion with a mid-point received power of -3.3 dBm and a received power of -28.5 dBm receiver using a PRBS of 2^{31}-1 .

The system compares very well with other types of mid span spectral inversion techniques discussed in Section 1.4.3 , especially if the link lengths between amplifiers are taken into consideration. The transmission could not be extended to 4 * 124 km as the OSNR was too degraded after 248 km transmission to allow for the

reconstruction to take place.

4.7 All Optical Phase Estimation

An all optical implementation of this technique was also considered. The AMZI output is a power level proportional to the instantaneous frequency. The frequency of the output of the laser is related to the carrier density. Thus, AMZI output was injected into the NEL laser as this has a direct correlation to the instantaneous frequency. This will result in the carrier density following the instantaneous frequency of the received signal and result in modulation being reconstructed on the output of the injected laser.

 The experimental set-up is shown in Figure 57. The 10.7 Gbit/s DPSK signal was generated using a wideband phase modulator and a tunable laser. The OSNR of the signal was degraded by attenuating the input to a fixed output power fibre amplifier. The input stage of the converter comprised a 0.8 nm channel selection filter,and a planar silica AMZI with a free spectral range of 85.2 GHz biased at quadrature followed by a circulator and polarisation control. The output of the circulator was used to inject optical signal into the laser. The transmission output of the circulator is sent to a standard DPSK receiver consisting of a channel selective filter of 0.64 nm, a pre-amplifier, a 1 bit differential delay AMZI to allow for phase to amplitude conversion followed by directed detection by a 10 GHz bandwidth detector.
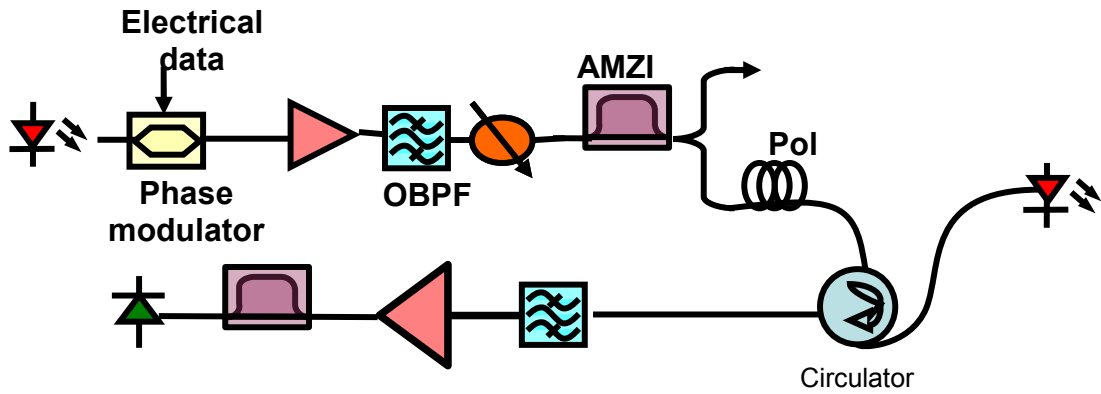
Figure 57: Block diagram of all optical phase reconstruction.

A CIP high speed laser was used. It was in a 14 pin DIL package with an output of 2.1 mW for a bias of 70 mA at 20ºC. The data sheet indicates a 3dB bandwidth with 0 dBm RF power and 70 mA of 13 GHz − this should be sufficient to allow for optical modulation of the device.

Figure 58 shows the unmodulated spectrum of the laser. The laser will be injected with the incoming signal at >2 nm from the lasing wavelength. The laser used for the transmitted signal is a tunable external cavity laser.

The laser was injected with a signal at 1553 nm, i.e. 5 nm away from the lasing wavelength. The overlaid and amplitude normalized signals are shown in Figure 59. It can be seen that the operation is strongly non-linear from the clock tones being replicated in the CIP output. The laser is indeed encoded with a 10 Gbit/s signal but its relationship to the original signal is not consistent and no sensible decoding could be established. The original signal could not be recovered. The laser responded to the injected signal in a pattern dependent manner and also caused frequency modulation. This resulted in a complex pattern dependent encoding of the data in frequency and phase of the laser. As can be seen from the spectrum, the bandwidth of the CIP laser signal is limited and the optical spectrum is not symmetrical.

CO2 Trimming - Error Function 0.2 dB/D   2006 Aug 14 16:21

▽	▽1	▽2	▽2-▽1	A:FIX /BLK
1558.632nm	1558.224nm	1557.426nm	-0.798nm	B:WRITE /DSP
0.19dBm	-59.68dBm	-59.15dBm	0.53dB	C:FIX /BLK

10.0dB/D   RES:0.01nm   SENS:MID   AVG: 1   SMPL:AUTO
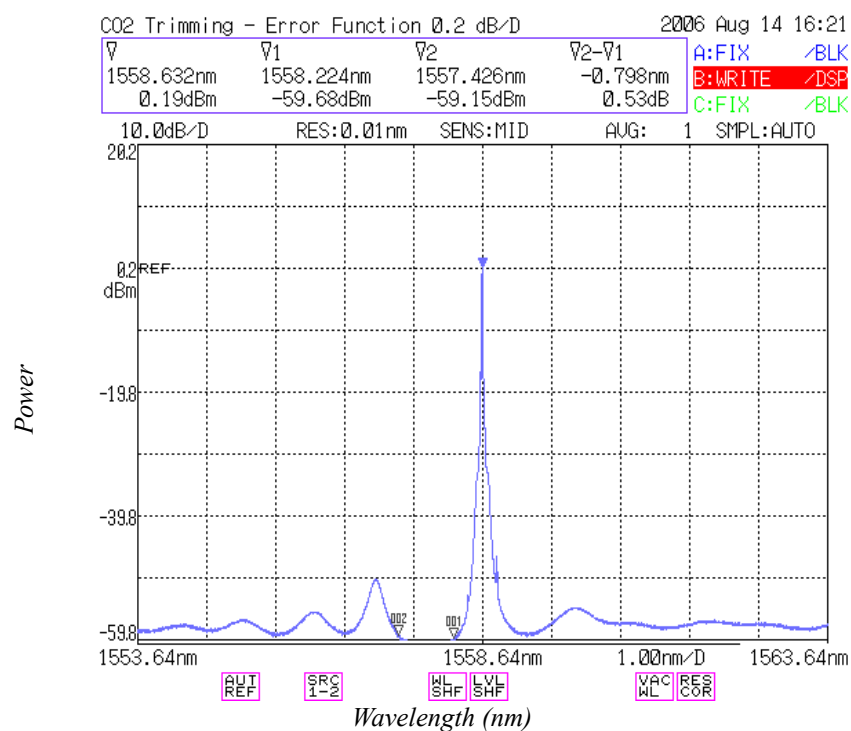
Figure 58: Unmodulated optical spectrum of CIP laser without isolator showing laser stop gap.
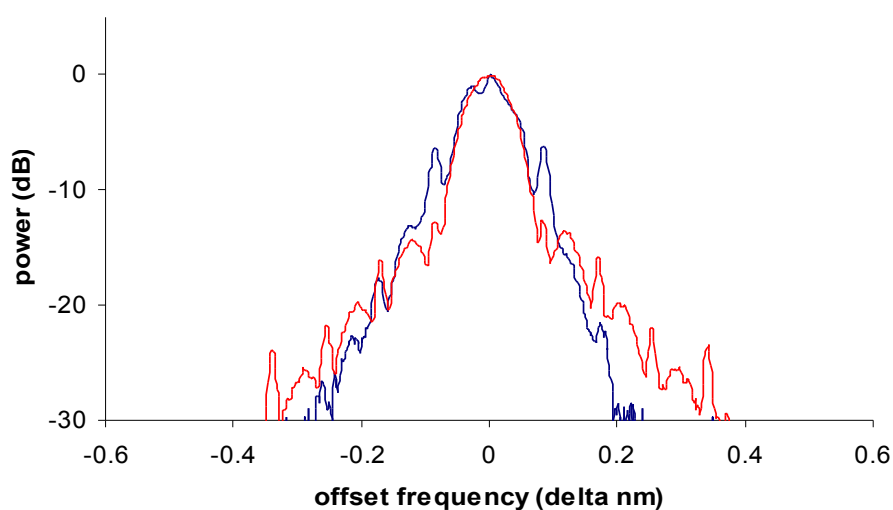
Figure 59: Overlaid transmitted spectrum (blue) and corresponding modulated CIP (red) when injected by wavelength 5 nm away.

The previous section has shown that the signal that is injected into the CIP laser does contain the correct information. Here it is demonstrate that phase modulation does result from directly injecting this signal into the laser. The precise response is not

92

understood and remains an open research area.

4.8 Conclusion

This Chapter has presented a description of the critical components that are used in this experiment, i.e. modulators and fibre links. The recirculating loop that is used to allow transmission distances that will challenge the full field receiver's ability to recover highly dispersed signals has been introduced. It has been shown, most importantly, that the principle of phase estimation is practical and that the phase information of a received signal can be converted with sufficient accuracy into the electrical domain and used for further processing. Another implementation configuration was illustrated, i.e. all optical phase estimation. This is presented as a preliminary investigation of a parallel implementation. This thesis work will concentrate on all electronic signal reconstruction and digital signal processing methods for dispersion compensation.

5 Detailed Simulation Model and Experimental Results

5.1 Introduction

This chapter describes the detailed simulation completed primarily in MATLAB with collaborating simulations from the recently implemented VPI co-simulation interface, which allow easy transfer of waveforms to and from MATLAB. The experimental set-up will be described in detail and the most significant experimental results will be presented. The critical parameters of the receiver will be identified by use of in-depth simulation. The parameters which are unique to the experimental set-up will be separated from those fundamental to this technique as a preparatory step towards integration and automating the electronic processing parameter selection. It will be illustrated that the physical mechanisms resulting for implementation of this technique are sufficiently understood to allow for very accurate simulation. This includes low frequency noise in the receiver chains that could be detrimental to the phase estimation. Other physical effects that are simulated and understood are fibre non-linearity, thermal noise in the receiver and sampling rates. The noise limited nature of receiver-side EDC is explored. The most vulnerable bit to recover for any receiver-side EDC is an isolated '1' bit as the energy from this will be spread into neighbouring '0' bits. This will be investigated and a number of possible methods to ameliorate this will be discussed. The experimental results will be presented in a progressive manner as each limiting factor identified in the simulation is overcome.

5.2 Extended Simulations (MATLAB) [iii]

Due to the limited ability to use down sampling and data exchanged between MATLAB and VPI 6.5, a basic transmission model was developed in MATLAB using Analogue to Digital (ADC) followed by Digital Signal Processing (DSP). DSP implementations of this EDC technique were not possible using the limited electronic feature set of VPI 6.5 and sothe feasibility of DSP based EDC was investigated using MATLAB. For computational simplicity, the simulations were initially performed with lumped dispersion with noise loading at the receiver. For longer transmission distances, where self phase modulation (SPM) may not be neglected, the simulations are completed using split step Fourier analysis [53]. These simulations let to the development of robust DSP algorithms and an understanding of the effects of imperfections in the receiver and link configuration. These were later verified by simulation using subsequent versions of VPI that allowed for embedded MATLAB code.

5.3 Principle and Simulation Model

Difficulties arise in matching the response of two independent receiver chains. Therefore, in this work, to allow for more readily matched performance of experimental implementation, an equivalent implementation is adopted using a balanced detector to give $V_1 - V_2$ and an additional single photodiode to obtain $V_1 + V_2$.
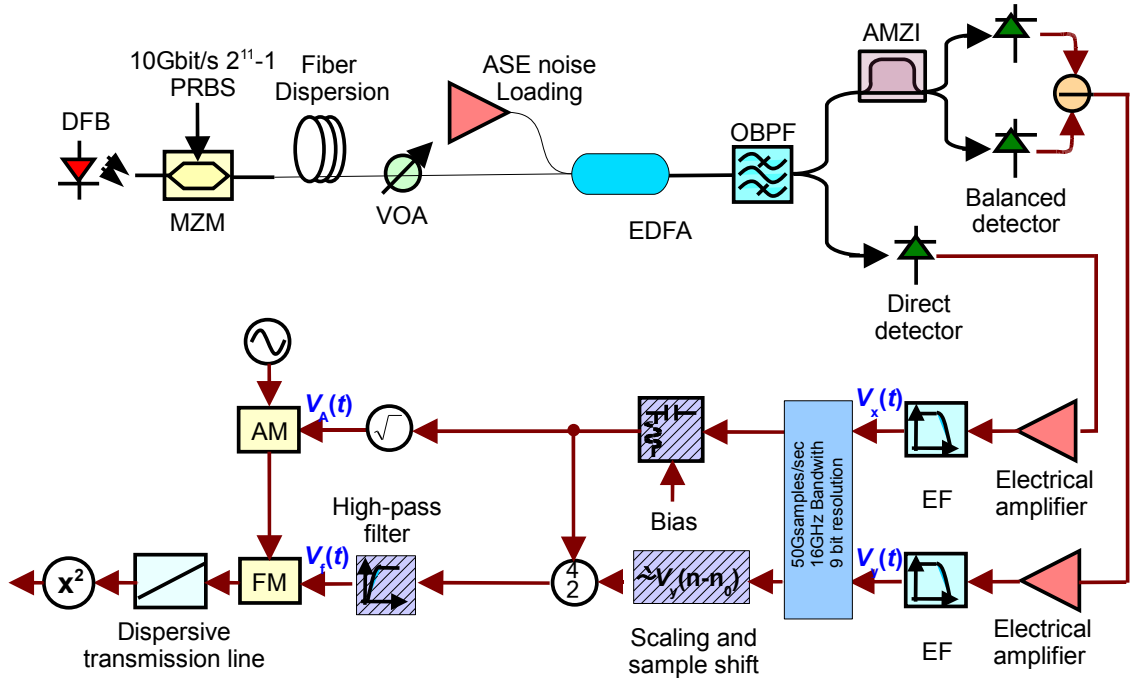
Figure 60: Schematic diagram of MATLAB simulation.

Figure 60 shows the simulation model used in this work, including a number of additional signal processing refinements reported in subsequent sections (shown with hatching lines in Figure 60). Continuous wave light was intensity modulated by a 10 Gbit/s OOK data train using a Mach-Zehnder modulator (MZM). The data train consisted of a $2^{11}-1$ pseudo-random binary sequence (PRBS) repeated nine times (18,423 bits). 10 '0' bits and 11 '0' bits were added before and after this data train, respectively, to simplify the boundary conditions. The bits were raised-cosine shaped with a roll-off coefficient of 0.4 and 40 samples per bit. The extinction ratio of the modulated OOK signal was set by adjusting the bias and the amplitude of the electrical OOK data.
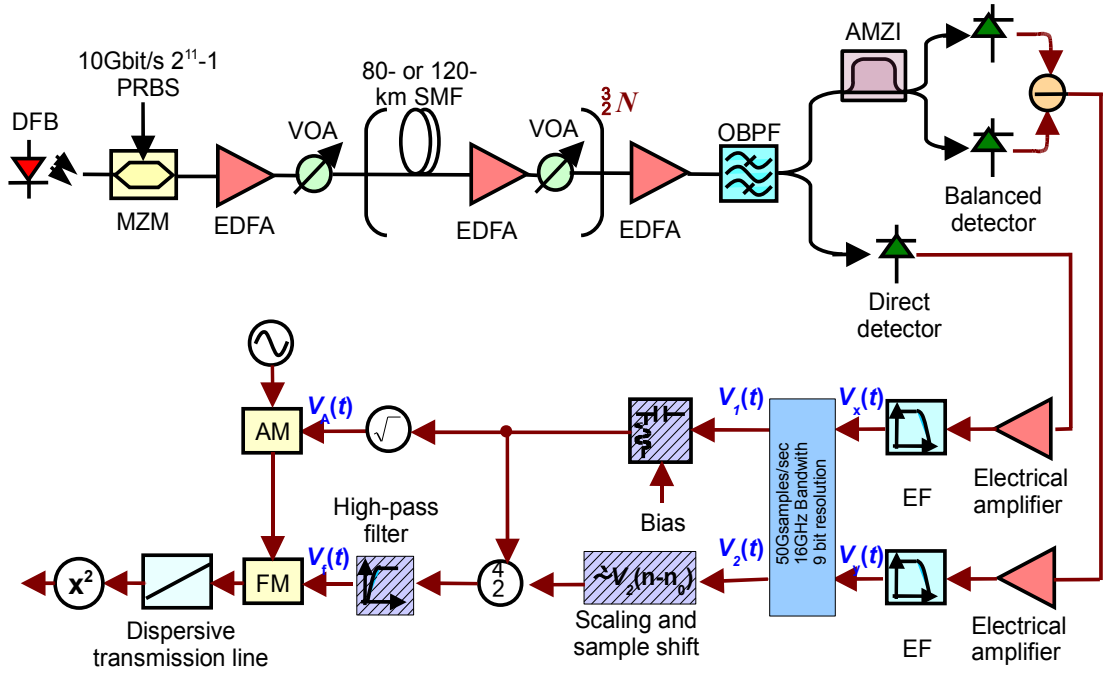
Figure 61: Schematic of simulation set-up for split step Fourier analysis.

The split step simulation method for solving non-linear equations which do not have general analytical solutions is described in [103]. Using this method to solve non-linear equations, the simulation set-up is shown in Figure 61. YOU just said this already! This is done by separating out the effects of the linear and the non-linear parts and implementing both over a small distance h repeated a large number of times N. There is a trade off between the accuracy of the simulation ($h \rightarrow 0$) and the length of time it takes for the simulations to run ($N \rightarrow \infty$) A schematic of a section is illustrated in Figure 62. :

$$A_n(t,z+h)=e^{i\gamma|A|^2 h}A(t,z) \qquad A_{N+1}(t,z+2h)=e^{i\gamma|A|^2 h}A_{N+1}(t,z+h)$$

$$if \; \tilde{A}_N(\omega,z+h)=\mathbf{\textit{fft}}\,(A_n(t,z+h))$$

$$\tilde{A}_{N+1}(\omega,z+h)=\exp[\frac{i\,\beta_2}{2}(\omega-\omega_0)^2 h]\,\tilde{A}_n(\omega,z+h)$$

$$A_{N+1}(t,z+h)=\mathbf{\textit{ifft}}\,(\tilde{A}_{N+1}(\omega,z+h))$$
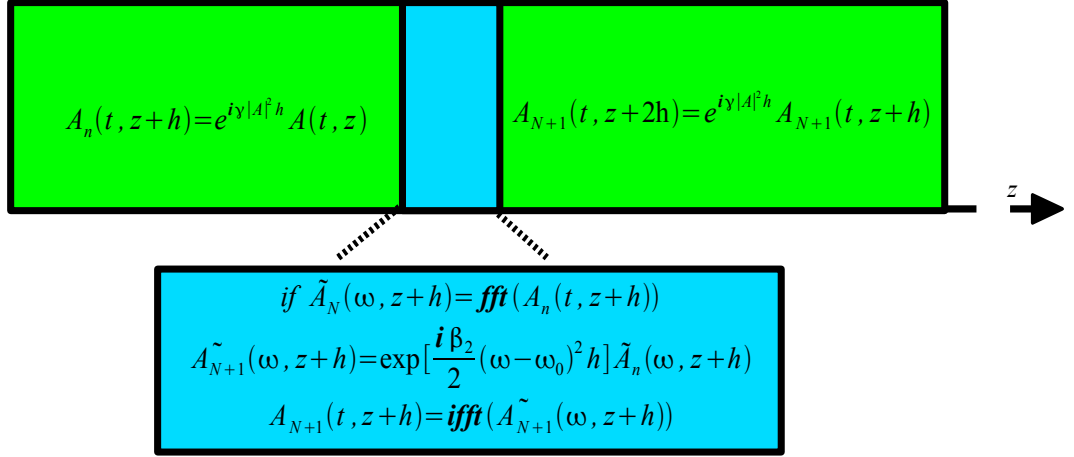
Figure 62: Split set method of simulating non-linear equations.

The signal was launched into the transmission link, whose configuration included the fibre length and launch power per span. In this section, two cases were investigated: (1) 80 km SMF per span; (2) 120 km SMF per span. The SMF was assumed to have CD of 16 ps/km/nm, a non-linear coefficient of 1.2 /km/W and a loss of 0.2 dB/km. The split-step Fourier method was used to calculate the signal propagation in the fibres. At the end of each span, noise from optical amplifiers was modelled as complex additive white Gaussian noise with zero mean and a power spectral density of $n_{sp}h\nu(G\text{-}1)$ for each polarisation, where G and $h\nu$ are the amplifier gain and the photon energy respectively. n_{sp} is the population inversion factor of the amplifiers and was set to give a 4 dB amplifier noise figure (NF).

The noise of the optical pre-amplifier was also modelled as additive white Gaussian noise with random polarisation. The launch power into the pre-amplifier was adjusted to control the OSNR while the output power was varied to investigate the influence of thermal noise. The pre-amplified signal was filtered by an 8.5 GHz Gaussian-shaped optical band pass filter (OBPF) which suppressed the optical noise and chromatic dispersion to a certain extent. The signal after the OBPF was then split into two paths to extract $V_x(t)$ (electrical output of single photodetector) and $V_y(t)$

(electrical output of the balanced detector) respectively. The AMZI for the extraction of $V_y(t)$ had $\pi/2$ phase shift and a delay time of either 10 ps or 30 ps. The responsivities of the balanced detector and the single photodetector were assumed to be 0.6 and 0.9 respectively, and equivalent thermal noise spectral power densities were assumed to be 100 pA/Hz$^{1/2}$ (u2t Photonics BPDV2020R) and 18 pA/Hz$^{1/2}$ (Bookham PT10XGCJ57)respectively. These receiver parameters match typical values of the commercial detectors used in the recent experimental demonstration . After detection, the signals were electrically amplified, filtered by 15 GHz 4th-order Bessel electrical filters (EFs), and down-sampled to 50 Gsamples/s (5 samples per bit at 10 Gbit/s) to simulate the sampling effect of the commonly implemented real-time oscilloscope. The down-sampled copy of $V_x(t)$ was re-biased, which can significantly enhance the robustness of the scheme to thermal noise. To allow for path length variations due to manufacturing tolerance, temperature variations and device ageing, a sample shifting was included to provide delay tunability with a resolution equivalent to the sampling interval, and the amplitude was adjusted to correct for the scaling constant which equals $1/(2 \, \delta t)$ and any gain imbalance. $V_A(t)$ and $V_f(t)$ thus represent the recovered intensity and instantaneous frequency respectively. This information was exploited to reconstruct a replica of the optical signal, which was subsequently compensated using a dispersive transmission line. The compensated signal was then square-law detected and decoded using optimal threshold detection.

The simulation was iterated seven times with different random number seeds to give a total of 128,961 simulated bits. The performance was evaluated in terms of the required OSNR to achieve a bit error rate (BER) of $5*10^{-4}$ by direct error counting.

5.4 Suppression of Low-frequency Component Amplification [xii]

The performance of the full optical-field EDC greatly depends on the quality of the phase estimation, which, , was found to be fundamentally degraded by an impairment arising from low-frequency amplification. To determine the origin of such instability, the Fourier transform of the estimated phase is used to show the relationship between $V_p(t)$ and $V_f(t)$ in the frequency domain:

$$V_p(t) \propto 2\pi \int_0^t V_f(\tfrac{1}{100})d\tfrac{1}{100} \quad \text{or} \quad V_p(\omega)=\frac{2\pi V_f(\omega)}{i\,\omega} \quad , \tag{45}$$

where $V_p(\omega)$ and $V_f(\omega)$ are the spectra of $V_p(t)$ and $V_f(t)$, respectively. It is clear from equation (45) that the low-frequency components of $V_f(t)$ dominate phase reconstruction, with an amplification factor of $1/\omega$. Therefore, if there is noise or inaccuracy in the estimated $V_f(t)$, its low-frequency components accumulate and eventually limit the performance of the following EDC. This is illustrated in Figure 63.

As the optical signal is chirped at arrival at the receiver, $V_f(t)$ will change similarly to that shown above – it will be proportional to the instantaneous frequency but will also contain noise. The spectrum $V_f(\omega)$ is shown to be contaminated by noise indicated in red. In order to estimate the phase of the signal, which is necessary for reconstruction, it must be integrated. If this function this function is observed in the frequency domain, it has a transfer function of $1/(i\omega)$ which is represented by the trace shown in blue. This has a gain that approaches infinity at DC. This means that low frequency noise will be greatly amplified by integration. This suggests that the low-frequency components of $V_f(t)$ should be minimized.

Figure 63: Illustration of low frequency amplification due to integration for phase estimation.

To achieve this a small extinction ratio to minimise the low frequency content of V_f and a high-pass electrical filter to suppress the impairment from low-frequency component amplification in the frequency estimation path only are employed. This is illustrated by the red line limiting the possible amplification of the low frequency component due to integration. By placing the high pass filter in the frequency estimation path only, this minimises the distortion to the overall construction by allowing the low frequency characteristics to be propagated along the amplitude path which is more robust to noise.

To simplify the analysis, fibre non-linearity and thermal noise are not considered in this section. The fibre length per span is 80 km. The time delay of the AMZI and the bias of $V_x(t)$ are assumed to be 10 ps and 0 V, respectively.

Figure 64: V_f(♥ [(a)-(c)] and the eye diagrams of the signal after dispersion compensation [(d)-(f)] at fibre length of 2160 km. (a) and (d): extinction ratio is 25 dB and no high-pass electrical filter is employed; (b) and (e): extinction ratio is 12 dB and no high-pass electrical filter is employed; (c) and (f): extinction ratio is 12 dB and a 0.85 GHz high-pass electrical filter is employed.

Figure 64 shows V_f(♥ [(a)-(c)] and the eye diagrams of the signal after dispersion compensation. (a) and (d) show the results for a very good extinction ratio (25 dB) and no modification to the receiver. A reduced extinction ratio of 12 dB is shown inq- (b) and (d) but still no high-pass electrical filter is used. In (c) and (f), an extinction ratio of 12 dB is used and a 0.85 GHz high-pass filter is employed. At a larger

extinction ratio [(a) and (d)], the value of $V_A(t)$ for logical data '0' is so small that a small amount of optical noise leads to large estimation inaccuracy of

$$V_f(t) = V_y(t)/V_A(t)^2$$ This inaccuracy has a lot of low-frequency components, which are further amplified by the impairment from low-frequency component amplification. By using a smaller extinction ratio, the low-frequency components of V_f are reduced, which alleviates the instability in phase reconstruction. The high-pass electrical filter further eliminates the low-frequency components of V_f. As a result, the compensated OOK signal after 2160 km transmission, shown in Figure 64(f), has a significantly clearer eye than that in Figure 64(d). To quantify the performance improvement of the proposed methods, Figure 65(a) depicts the required OSNR (0.1 nm resolution) for these three cases. Circles, triangles, and squares represent the cases of 25 dB extinction ratio and without a high-pass electrical filter, 12 dB extinction ratio and without a high-pass electrical filter, 12dB extinction ratio and with a 0.85 GHz high-pass electrical filter, respectively. From Figure 65(a) and (b), it is shown that by using 12 dB extinction ratio and a 0.85 GHz high-pass electrical filter, the OSNR transmission limit can be significantly extended. At fibre length of 2160 km, the required OSNR is around 13.7 dB, confirming the effectiveness of the proposed method. It should be noted that the high-pass electrical filter suppresses the impairment from low-frequency component amplification but introduces distortion to $V_f(t)$ as well. Therefore, the upper and lower levels of the eye diagrams in Figure 64(f) are thicker than those in Figure 64(e). At an extinction ratio of 12 dB, the bandwidth of the electrical filter was optimised for 2160 km transmission, which is around 0.85 GHz as shown in Figure 65(b).
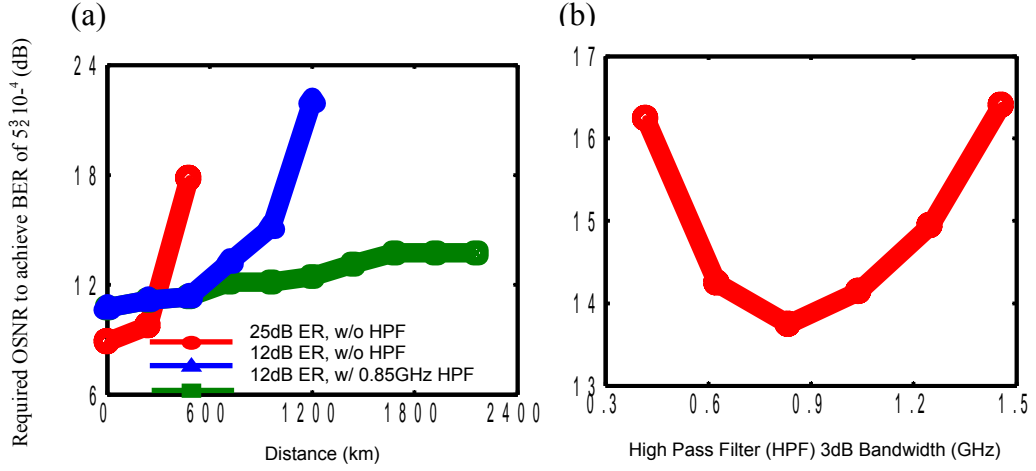
Figure 65: (a) The required OSNR versus the transmission distance at 25 dB extinction ratio and without a high-pass electrical filter (circles); at 12 dB extinction ratio and without a high-pass electrical filter (triangles); at 12 dB extinction ratio and with a 0.85 GHz high-pass electrical filter (squares). (b) The required OSNR versus the 3 dB bandwidth of the high-pass electrical filter at the fibre length of 2160 km and the extinction ratio of 12 dB.

5.5 Impact of Fibre Non-Linearity

Figure 65(a) depicts the OSNR performance without non-linearity, in which case the transmission link is linear and thus, fibre link configurations do not significantly influence the system performance. However, by taking the fibre non-linearity into consideration, it would be essential to design the signal launch power and the fibre length per span to allow for sufficient OSNR margin for the transmission system, whilst avoiding excessive non-linearity. Figure 66 shows the required OSNR without (circles) and with (triangles) fibre non-linearity and the actual obtained OSNR (squares) for 80 km SMF fibre per span and -3 dBm signal launch power. The extinction ratio is 12 dB and a 0.85 GHz Gaussian-shaped high-pass electrical filter is employed. The time delay of the AMZI and the bias of $V_1(t)$ are assumed to be 10 ps and 0 V respectively. Thermal noise is neglected in this section. From Figure 66, it is shown that by taking fibre non-linearity into consideration, the additional penalty is limited to 1.8 dB for fibre length less than 2160 km. On the other hand, the actual

OSNR degrades as the fibre length increases. In fact, the actual obtained OSNR can be derived as follows:

$$OSNR = \text{signal launch power (dBm)} - \text{fibre loss per span (dB)} -$$
$$(2^{\frac{3}{2}} N^{\frac{3}{2}} n_{sp} h \searrow \Delta v) \text{ (dBm)}$$

(46)

where N is the span number. For a 1550 nm optical signal and 0.1 nm (~12.5 GHz) resolution, $2^{\frac{3}{2}} n_{sp} h \searrow 12.5$ GHz = -54 dBm. Therefore, when $N=3$ and $N=27$, corresponding to fibre length of 240 km and 2160 km, the actual obtained OSNRs are 30.2 dB and 20.6 dB respectively. These results agree well with the Monte Carlo simulation results, as shown by the squares in Figure 66.
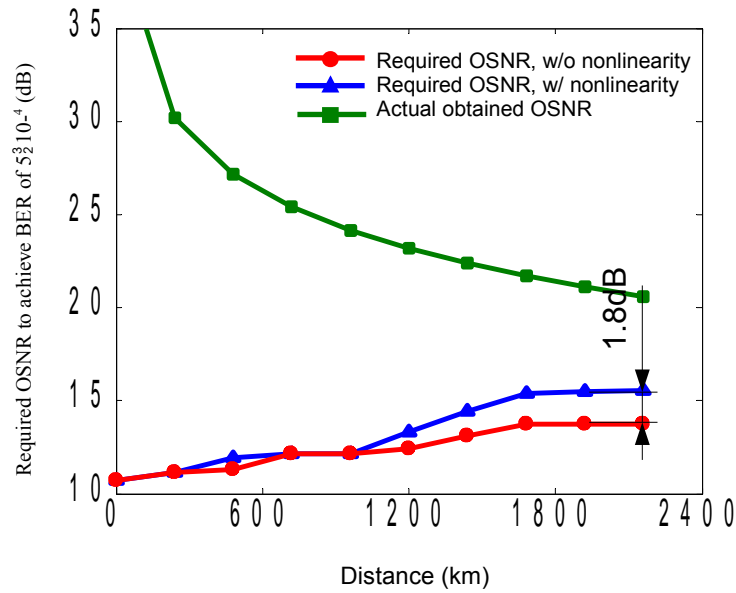
Figure 66: Required OSNR without (circles) and with (triangles) fibre non-linearity and the actual obtained OSNR (squares) for 80 km SMF fibre per span and -3dBm signal launch power. The extinction ratio is 12 dB and a 0.85 GHz Gaussian-shaped high-pass electrical filter is employed. The time delay of the AMZI and the bias of $V_1(t)$ are assumed to be 10 ps and 0 V respectively

To find out the influence of the signal launch power per span, Figure 67(a) shows the required OSNR (circles) and the actual obtained OSNR (triangles) versus the signal launch power at fibre length of 2160 km with 80 km per span. In Figure 67 (a), the required OSNR for 0 dBm signal launch power is not plotted because it is higher

than the actual obtained OSNR of 23.6 dB. The time delay of the AMZI and the bias of $V_1(t)$ are assumed to be 10 ps and 0 V respectively. From the Figure, it is shown that for the signal launch power less than -4.5 dBm, the required OSNR (circles) approaches to that without non-linearity, 13.7 dB as shown in Figure 67(a). When the signal launch power is larger than -3 dBm, the penalty induced by the fibre non-linearity increase significantly. On the other hand, the maximum attainable OSNR is linearly proportional to the signal launch power. -3 dBm is a near-optimum value to achieve the balance between the fibre non-linearity induced penalty and the maximum attainable OSNR, allowing for 5 dB OSNR margin.
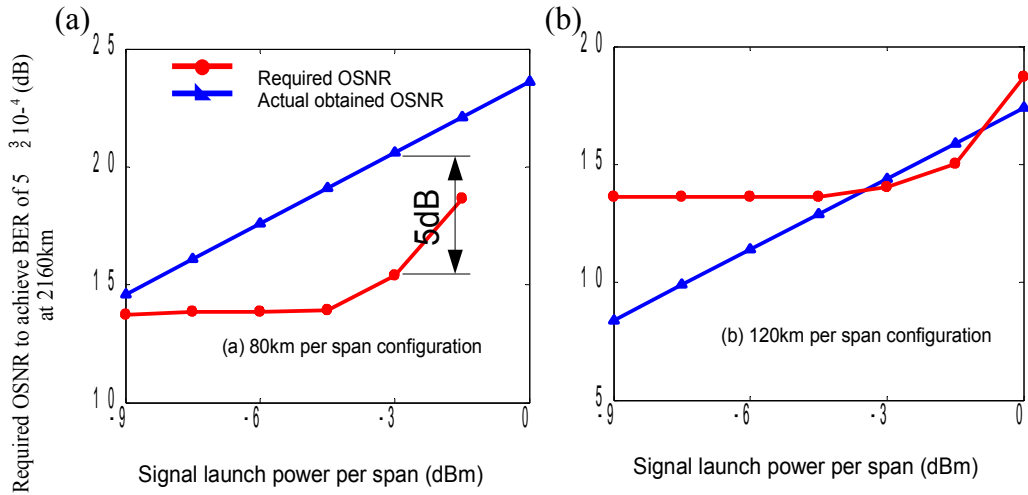
Figure 67: Required OSNR (circles) and the maximum attainable OSNR (triangles) versus the signal launch power at fibre length of 2160 km with (a) 80 km per span and (b) 120 km per span. For both (a) and (b), the time delay of the AMZI and the bias of $V_1(t)$ are assumed to be 10 ps and 0 V respectively

Besides signal launch power per span, the fibre length per span would also play an important role in the system design. Figure 67(b) shows the attainable OSNR and required OSNR for 120 km span spacings. It should be noted that in the Figure, the required OSNR for the signal launch power of 0 dBm, -4.5 dBm, -6dBm, -7.5dBm, and -9 dBm were simulated by assuming that the amplifiers in the fibre links have no noise and the noise was only loaded at the receiver because the required OSNR for

these cases is higher than the actual obtained OSNR. From the Figure, it is shown that compared to the 80 km per span configuration with the same signal launch power, the required OSNR (circles) by using 120 km per span is reduced, due to less fibre non-linear effect from larger transmission loss. However, the actual OSNR decreases dramatically compared to Figure 67(a). As a result, such system configuration is more sensitive to the signal launch power and even at the optimal signal launch power (-1.5 dBm), the OSNR margin is only around 0.8 dB, more than 4 dB less than that in Figure 67(a).

5.6 Enhanced Robustness to Thermal Noise

The previous results indicate the impact of OSNR on the performance of full field EDC. However, in practical systems, thermal noise may be equally important. The increased significance of thermal noise when compared to a conventional direct detection receiver may be attributed to the frequency/phase estimation process, where the balanced detector output is divided by the total received power. For long strings of data zeroes reconstruction due to the impact of noise are more likely resulting in erroneous reconstruction. The periods of low received power results in both the received total power and its difference being dominated by noise rather than the required signal.

Thermal noise might exhibit a comparable effect as the optical noise even in the OSNR limited operation region. To show the influence of the thermal noise, Figure 68 (a) show the required OSNR versus the fibre length without and with thermal noise for 0 V bias of $V_x(t)$ and 10 ps time delay for the AMZI when the received optical powers of the balanced detector and amplitude detector (include both optical signal and optical noise) are both 0 dBm. From the Figure, it is shown that thermal

noise has significant impact on the system performance and limits the transmission distance to less than 300 km. To solve this problem the use of an AMZI with a large time delay and properly biasing the detected intensity signal before optical-field reconstruction to enhance the robustness of the scheme to thermal noise is proposed. Mathematically, $V_f(t)$ in Figure 61 can be derived as (where n_{th_x} and n_{th_y} represent the thermal noise on $V_x(t)$ and $V_y(t)$ respectively):

$$V_y = V_1 - V_2 \tag{47}$$

Therefore following the assumption in Chapter 2

$$V_y \approx |E_0(t)|^2 \omega(t) \Delta t \tag{48}$$

But this will be corrupted by noise of the balanced detector

$$V_y \approx |E_0(t)|^2 \omega(t) \Delta t + n_{th_y} \tag{49}$$

Similarly $V_x(t)$, the output of the amplitude detector will be corrupted by noise

$$V_x(t) = |E_0(t)|^2 + n_{th_x} \tag{50}$$

Resulting in a $V_f(t)$

$$V_f(t) = \frac{V_y(t)}{V_x(t)\Delta t} = \frac{|E_0(t)|^2 \omega(t) + \dfrac{n_{th_y}}{\Delta t}}{(|E_0(t)|^2 + n_{th_x})} \tag{51}$$

Thus

$$V_f = \frac{|E_0(t)|^2 \omega(t)}{(|E_0(t)|^2 + n_{th_x})} + \frac{\dfrac{n_{th_y}}{\Delta t}}{(|E_0(t)|^2 + n_{th_x})}$$

$$V_f(t) \underset{|E_0(t)|^2 \to 0}{\overset{\Delta t \to \infty}{\longrightarrow}} \frac{\omega(t)}{1 + \dfrac{n_{th_x}}{0}} \tag{52}$$

As can be seen from above, having a large AMZI time delay reduces the dependence of signal estimation on the thermal noise of the balanced detector. The estimation is still affected by the thermal noise of the amplitude receiver but this is less than the thermal noise of the balanced detector by a factor of 10.

The method proposed to make the system more robust to thermal noise is to introduce a bias voltage in the $V_x(t)$ path and this results in the following.

$$V_f(t) = \frac{|E_0(t)|^2 \omega(t) + \dfrac{n_{th_y}}{\Delta t}}{|E_0(t)|^2 + V_{bias} + n_{th_x}}$$ (53)

Thus

$$V_f(t) \underset{|E_0(t)| \to 0}{\overset{\Delta t \to \infty}{\longrightarrow}} \frac{\omega(t)}{1 + \dfrac{V_{bias}}{0}}$$ (54)

for $V_{bias} + n_{th_x} \approx V_{bias}$

Thus the value of V_f will be slightly distorted but it will be distorted by a constant value which makes the influence of noise negligible. If V_{bias} is too small, it will not dominate the thermal noise but if it is too large, its value will affect the accuracy of the phase estimation, leading to an optimum value.

By adding a bias on $V_x(t)$, the value for logical data '0' is increased, leading to enhanced robustness to thermal noise $|E(t)|^2$. By employing an AMZI with a larger time delay, the output signal power from the AMZI is increased since $V_y(t)$ is proportional to àt, which therefore improves the signal to thermal noise ratio of $V_y(t)$. Considering the transfer function of the AMZI, a larger àt results in sharper slope in the AMZI response, hence giving a greater voltage change for the same change in instantaneous frequency.

Figure 68 (b) show the required OSNR versus the fibre length without (circles) and with (triangles) thermal noise for 0.3M bias for $V_x(t)$ and 30ps time delay for the AMZI, where $M=[E\{\text{✦}_1(t)\ ^2\}]^{1/2}$ and $E\{\text{✱}$ represents the ensemble average. The received optical powers of the balanced detector and single photodetector (include both optical signal and optical noise) are both 0 dBm. From the Figure, it is shown

that without thermal noise, the proposed method has negligible penalty compared to the case of 0 V bias for $V_x(t)$ and 10 ps time delay for the AMZI, as shown by the circles in Figure 68 (a). However, the method exhibits significant tolerance enhancement to thermal noise, which attributes to the great improvement in stabilizing the estimation of $V_f(t)$.
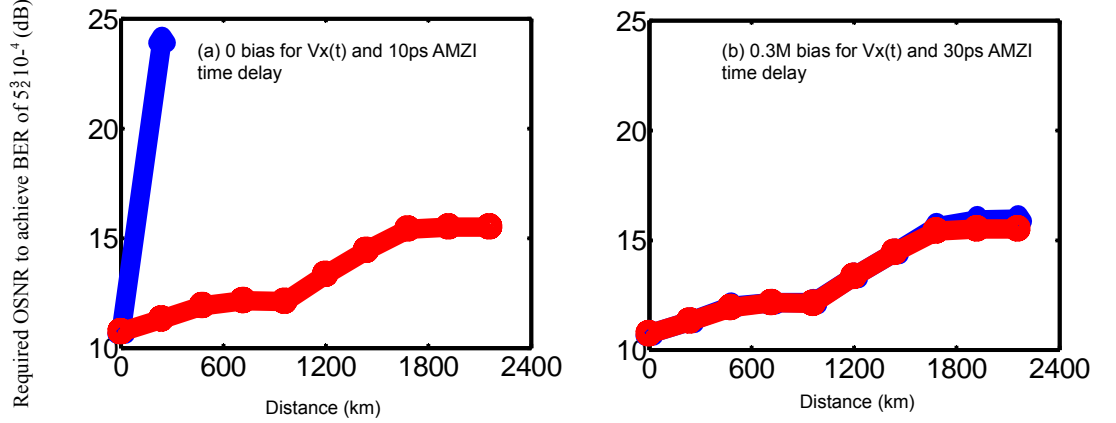
Figure 68: Required OSNR versus the fibre length without (circles) and with (triangles) thermal noise for (a) 0 V bias of $V_x(t)$ and 10 ps time delay for the AMZI; (b) 0.3M bias for $V_x(t)$ and 30 ps time delay for the AMZI, where M=[E{ ✦1(t) ^{2}}]$^{1/2}$ and E{✦ represents the ensemble average. The received optical powers of the balanced detector and single photo-detector (include both optical signal and optical noise) are both 0 dBm.

To further verify the effectiveness of the proposed method, Figure 69 shows the required OSNR versus the received optical power (including both optical signal and optical noise) at fibre length of 2160 km for (i) 0 bias for $V_1(t)$ and 10 ps time delay for the AMZI (circles); (ii) 0.3M bias for $V_1(t)$ and 10 ps time delay for the AMZI (triangles); (iii) 0.3M bias for $V_1(t)$ and 30 ps time delay for the AMZI (squares). From the Figure, it is shown that for case (i), a received optical power larger than 9 dBm should be required to achieve negligible penalty from the thermal noise. Such strict requirement can be significantly relaxed by properly biasing the $V_x(t)$. By both biasing the $V_x(t)$ and using an AMZI with a larger time delay, the received optical power is further reduced. As a result, in case (iii), less than 0.5 dB thermal noise

induced OSNR penalty is achieved for 0 dBm received optical power, which, on one hand, still provides 4.5 dB OSNR margin for the transmission systems, on the other hand, significantly relaxes the requirements for the gain of the pre-amplifier, the loss of the OBPF and the AMZI, and the maximal power of the detectors. The following section assumes that both fibre non-linearity and thermal noise are included. $V_x(t)$ has a $0.3M$ bias and AMZI has a 30 ps time delay.
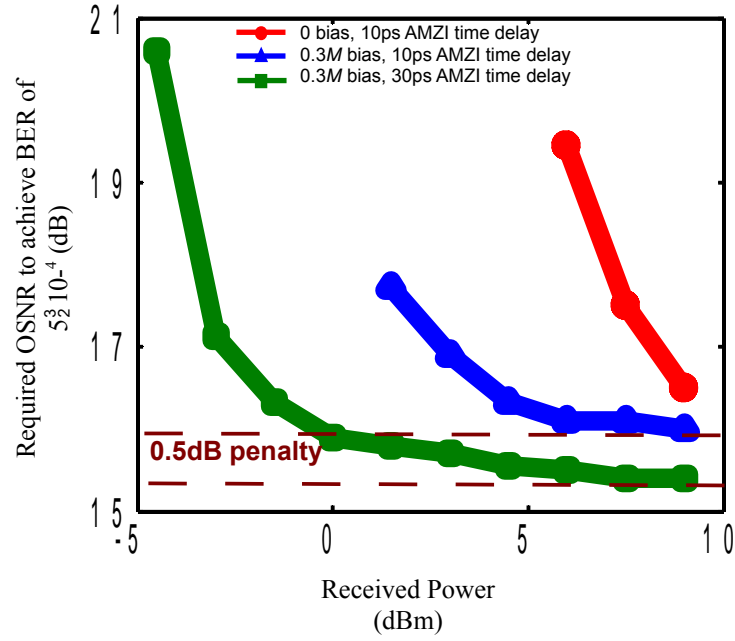
Figure 69: Required OSNR versus the received optical power (including both optical signal and optical noise) at fibre length of 2160 km for (i) 0 bias for $V_1(t)$ and 10 ps time delay for the AMZI (circles); (ii) 0.3M bias for $V_1(t)$ and 10 ps time delay for the AMZI (triangles); (iii) 0.3M bias for $V_1(t)$ and 30 ps time delay for the AMZI (squares)

5.6.1   Effect of V_{bias} Neglecting Noise

This is a note to consider the effect that the introduction of V_{bias} has in normal operation. As will be indicated in the experimental section, the physical purpose of V_{bias} is to compensate for the fact that the amplitude detector is AC couple and does not include the DC component of the signal. However, it is important to understand

the impact if this signal is set too great or too little

$$V_f(t) = \frac{V_y(t)}{V_x(t)\Delta t} = \frac{|E_0(t)|^2 \omega(t)}{(|E_0(t)|^2 + V_{bias})} \tag{55}$$

Thus

$$V_f(t) = \omega(t) \frac{1}{(1 + \frac{V_{bias}}{|E_0(t)|^2})} \quad, \tag{56}$$

which approximately gives

$$V_f(t) = \omega(t)(1 - \frac{V_{bias}}{|E_0(t)|^2}) \quad, \tag{57}$$

which leads to the to a reconstructed phase of

$$V_\phi = \int \omega(t)dt - \int \omega(t) \frac{V_{bias}}{|E_0(t)|^2} dt \tag{58}$$

The first term is what is required and the second term introduced by the V_{bias}

$$E = \sqrt{V_A} e^{\iota \phi} e^{V_{bias} \int \frac{\omega(t)}{|E_0(t)|^2} dt} \tag{59}$$

In general, this introduced term will be negligible for

$$\frac{V_{bias}}{|E_0(t)|^2} \to 0 \tag{60}$$

but it does limit the maximum value for the DC bias before it begins to affect the reconstruction detrimentally.

5.7 Optical Band Pass Filter (OBPF) [v]

For low cost application, assume ITU networking with 100 GHz spacing, therefore in metro applications one might use a relatively broad optical filter. However, given the impact of noise identified above, this section investigates the impact of OBPF (spon-spon noise effect on received zeros). The optimum high pass filter and extinction ratio combination and OBPF width is investigated. The effect of shorter amplifier spans will be considered. The simulation model used is shown in Figure 61.

The signal was launched into the transmission link of 120 km SMF per span with 0 dBm. The powers incident on the detectors were 0 dBm. The simulation was iterated 10 times with different random number seeds to give a total of 184,320 simulated bits. The performance was evaluated in terms of the required OSNR to achieve a BER of $5*10^{-4}$ by direct error counting. 184,320 bits were sufficient to produce a confidence interval of $[3.5*10^{-4}\ 7*10^{-4}]$ for this BER with 99% certainty.

Figure 70(a) shows required OSNR as a function of OBPF bandwidth at 6 dB and 12 dB extinction ratio for (a) 480 km and (b) 960 km. A 0.85 GHz high-pass electrical filter was used for suppression of low-frequency component amplification. From Figure 70(a), it is shown that when the ASE noise was not sufficiently suppressed (bandwidth >0.2 nm), a system with 6 dB signal extinction ratio exhibited better performance compared to that with 12 dB extinction ratio. As described above this is because a lower extinction ratio effectively reduced noise amplification arising from the division by total received power and low-frequency component amplification in phase estimation. However, the power penalty associated with the 6 dB extinction ratio system performance the ASE noise was sufficiently suppressed (bandwidth<0.2 nm). The optimal filter bandwidth was around 0.1 nm, at which the required OSNR was only 14 dB at BER of $5*10^{-4}$. In Figure 70(b), it is shown that for the optimized OBPF bandwidth, 960 km transmission reach was also achieved albeit with a substantially reduced tolerance in filter width. Clearly, the optimal performance depends on the balance between noise amplification and penalty induced by a lower extinction ratio and above a certain extinction ratio, no further benefit is achieved.
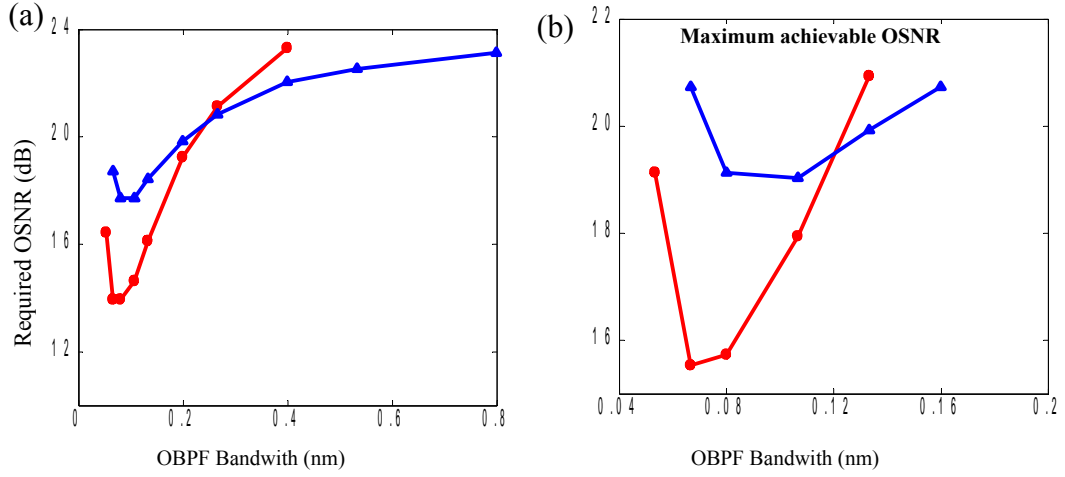
Figure 70: Required OSNR versus 3 dB bandwidth of OBPF at 6 dB extinction ratio (blue) and 12 dB extinction ratio (red) for (a) 480 km and (b) 960 km.

The capability of full-field EDC to compensate fibre length up to 1000 km is further verified is Figure 71(a). In this figure, it is shown that with 12 dB extinction ratio and 0.07 nm OBPF, the required OSNR to achieve a transmission distance of 1200 km was around 18 dB. As discuss In section 5.4 , a system with 12 dB signal extinction ratio, compared to that with a 6 dB extinction ratio, was more sensitive to low-frequency component amplification and thus the bandwidth of Gaussian-shaped high-pass electrical filter. The optimal high-pass filter bandwidth was found to be around 0.85 GHz at 12dB extinction ratio and 960 km, as depicted in Figure 71(b), beyond which distortions induced by high-pass electrical filter dominated.

Having demonstrated the importance of the optical filter width for reduction of spontaneous-spontaneous noise, thermal noise is re-introduced.
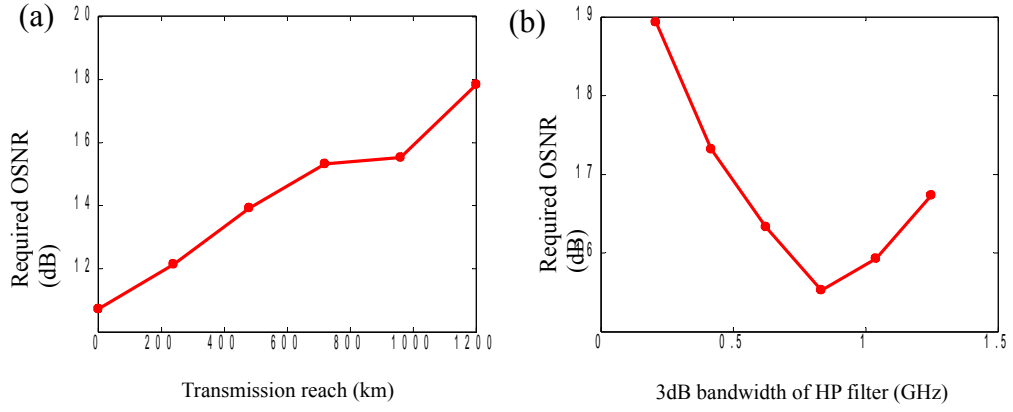
Figure 71: (a) Required OSNR versus fibre length at 12 dB extinction ratio. The high-pass filter is 0.85 GHz. (b) Required OSNR versus 3 dB bandwidth of high-pass filter at 960 km. The OBPF bandwidth is 0.07 nm

Although the optical power at the receiver could be high (e.g. 0 dBm), the power of $V_y(t)$ from the output of the AMZI depends on AMZI's differential time delay (46). Therefore, for small Δt, thermal noise could play an important role even for high signal powers and can be even more severe than ASE noise for sufficiently small time delay. The differential time delay of the AMZI in the previous simulations was assumed to be 10 ps, which was not sufficient to minimize the impact of thermal noise. The OSNR itself may be enhanced either by use of Raman amplification or by reducing the amplifier spacing. In order to combine all the features discussed above to examine the effect of these over longer transmission distance, it was selected to have an AMZI with 30 ps time delay, the signal to have a 12 dB extinction ratio, -3 dBm signal launch power per span and a fibre length per span of 80 km. The bandwidths of OBPF and high-pass electrical filter were optimized. Other parameters were the same as those in the previous simulation.
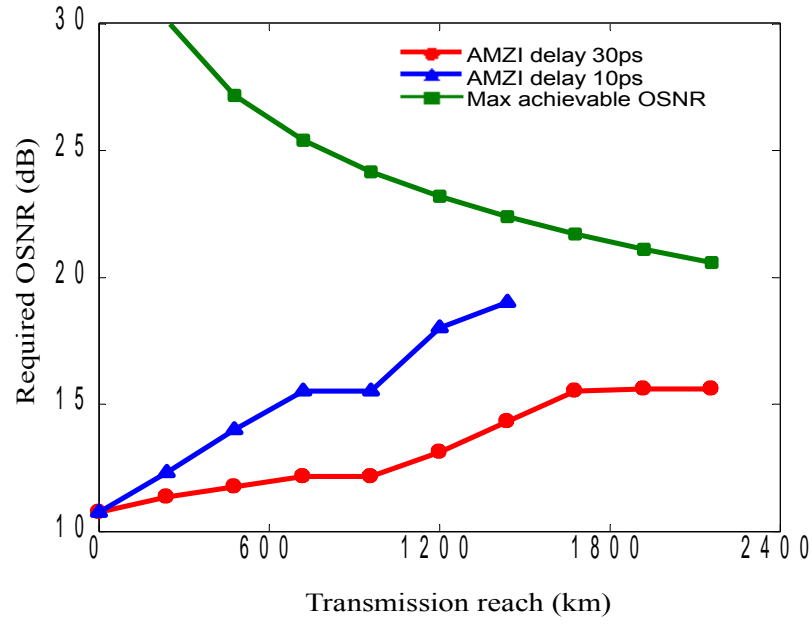
Figure 72: Required OSNR as a function of fibre length for AMZI time delay of 30 ps (circles) and 10 ps (triangles). Squares represent the maximum achievable OSNR. The OBPF and HP filter bandwidths are 0.07 nm and 0.85 GHz respectively. The extinction ratio is 12 dB.

Figure 72 shows the performance versus transmission distance for AMZI time delay of 30 ps (circles) and 10 ps (triangles). Squares represent the maximum achievable OSNR of the system. It is clearly shown that an AMZI with larger time delay could greatly improve the performance and allow 2160 km transmission with 15.7 dB required OSNR. Furthermore the 80 km amplifier spacing and -3dBm signal launch power per span provided improved maximum achievable OSNR resulting in a predicted OSNR margin of 5 dB at 2160 km.

5.8 AMZI Phase Misalignment

The optical system in the previous sections is assumed to be carefully optimized, i.e. the phase of the AMZI is perfectly adjusted to be $\pi/2$ and the signals are ideally oversampled. This enabled the DSP system and optical components to be designed to

minimise the impact of noise on FF-EDC. The next two sections examine the tolerance to these timing parameters.

For the case of AMZI phase misalignment, assuming that the phase of the AMZI is $\pi/2 + \alpha$, it can be readily shown that

$$V_A(t) = |E_0(t)|^2$$

$$V_f(t) = \frac{|E_0(t)|^2}{|E_0(t)|^2 + V_{bias}}(\omega(t) + \frac{\Delta\zeta}{\Delta t}) \quad, \tag{61}$$

where $\Delta\zeta$ represents the phase error. It has been verified that the first term of $V_f(t)$ can accurately estimate $\omega(t)$. The second term of $V_f(t)$ is from the AMZI phase misalignment. Therefore, the proposed compensator is to remove the second term of $V_f(t)$. In practice, a certain algorithm can be used to obtain $\Delta\zeta$ [vii]. Due to the slow variation of the phase drift, it is straightforward to ensure that the convergence speed of the algorithm is faster than the variation of the phase drift. This section, to simplify the analysis, adopts a stationary compensation for each phase misalignment value. Figure 73 shows the required OSNR versus the phase of AMZI at fibre length of 2160 km without (circles) and with (triangles) the proposed compensator. From the figure, it is clearly shown that without the compensator, the FD-EDC is very sensitive to the phase misalignment. At 1 dB penalty, the tolerance range is only ±7 degrees. By using the proposed method, the tolerance range can be significantly increased up to ±21 degrees at 1 dB penalty, more than 3 times than that without the compensator. These results verify the effectiveness of the proposed method.
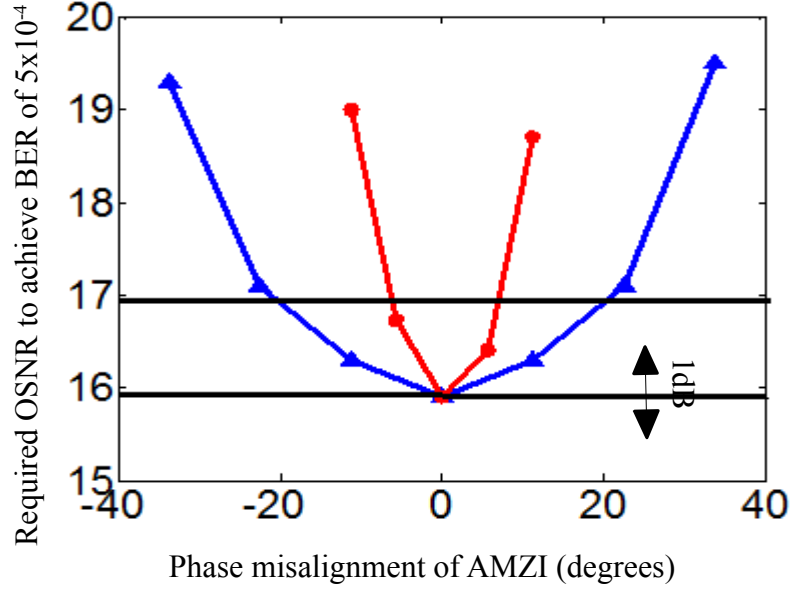
Figure 73: Required OSNR versus the phase of AMZI at fibre length of 2160 km without (circles) and with (triangles) the proposed compensator with 1 dB penalty operating region indicated.

5.9 Unsynchronized Sampling of $V_x(t)$ and $V_y(t)$

Because the signal is sampled with a resolution of 5 samples per bit or 20 ps time interval between two adjacent samples after re-sampling, any delay can be chosen between $V_x(t)$ and $V_y(t)$ to a time window of [$\frac{1}{100}$ n x 20] (ps) by shifting the digital sample, where $\frac{1}{100}$ is an arbitrary fixed time delay. For simplicity, the real-time oscilloscope is assumed to sample at the eye centre of $V_x(t)$. Figure 74 shows the required OSNR versus the delay of $V_y(t)$ from $V_x(t)$ at fibre length of 2160 km. From the Figure, it is shown that the curve is not symmetric. For near-optimum operation, the operation region of [-15 ps 5 ps] is chosen. For example, if the delay of $V_y(t)$ is 9 ps, the sampled $V_y(t)$ can be shifted by one sample to -11 ps, the maximum OSNR penalty is below 1 dB. In the laboratory experiments, the optimal shifting was implemented manually. In a practical system, an adaptive algorithm which can automatically optimize the samples shifting should be used. By properly shifting the

samples to an optimal operation region, the unsynchronized sampling of $V_x(t)$ and $V_y(t)$ would not be an essential impairment, with the OSNR penalty limited by 1 dB, as shown in Figure 74.
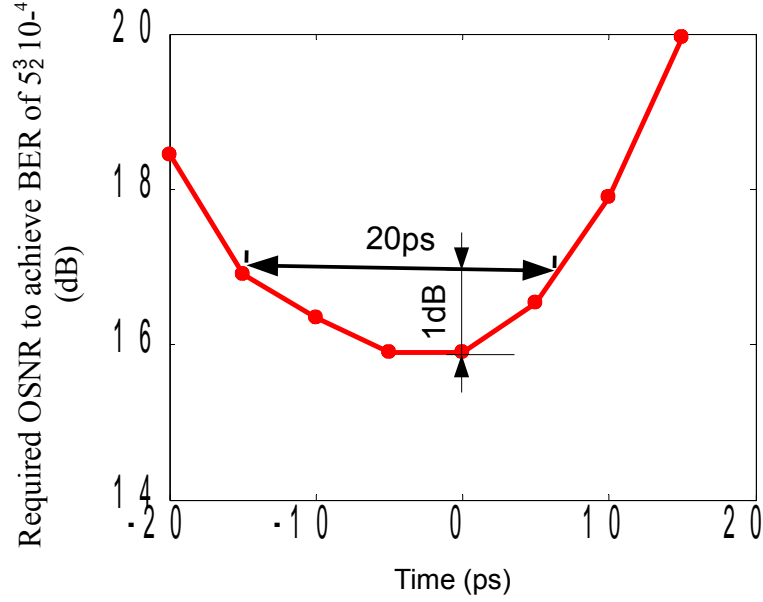
Figure 74: Required OSNR versus the delay of Vy(t) from Vx(t) at fibre length of 2160km where the optimum operating region allowing a 1 dB penalty due to sample time alignment is indicated by the horizontal arrow.

5.10 Effect of the Sampling Rate

According to the Sampling theorem [105], in order to convert analogue signals to digital signals, the maximum frequency which must be retained (F_{max} or B of signal) should be known. In the case of the 10 Gbit/s signal, a 20 Gsamples/s rate should be sufficient. Figure 75 shows the required OSNR versus the sampling rate at fibre length of 480 km, 960 km and 2160 km.
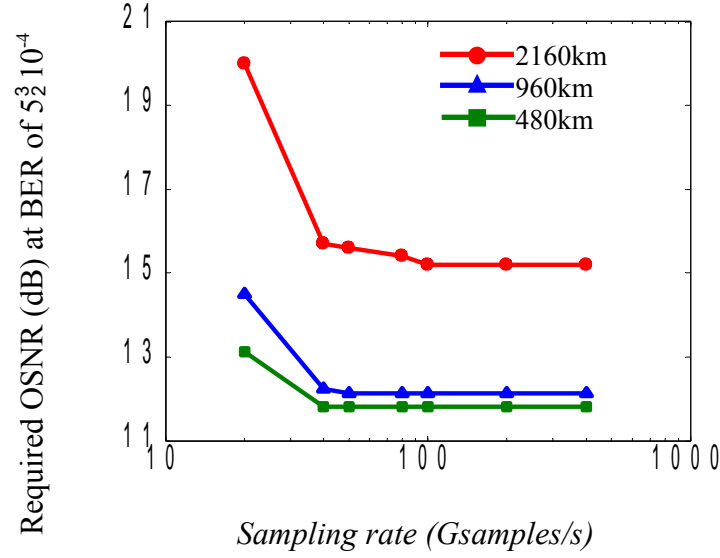
Figure 75: required OSNR versus the sampling rate at fibre length of 480 km, 960 km and 2160 km.

From the Figure, it is shown that the required OSNR is nearly the same for a sampling rate larger than 50 Gsamples/s. At sampling rate of 50 Gsamples/s, slight power leaks out of the frequency window of ±25 GHz, as shown in Figure 76(c). Figure 76(a) and (b) show the spectra and (d) and (e) show eye-diagram for lower sample rates and wider electrical bandwidth. In both cases (optimum sampling rate with a broader filter and lower sampling rate with a broader filter) significant power escapes from the frequency window, confirming that a low pass filter should be used to maximise the performance by controlling the signal spectrum. However, even when the optimum 7 GHz filter in employed, a relatively high sample ratio (50 GHz) is required, reflecting the broadened spectrum of V_f, which ,after transmission, has significant content up to 2.5 times the bit rate. 50 Gsamples/s is an optimal value to achieve the balance between the complexity of the real-time sampling device and the OSNR penalty.

120
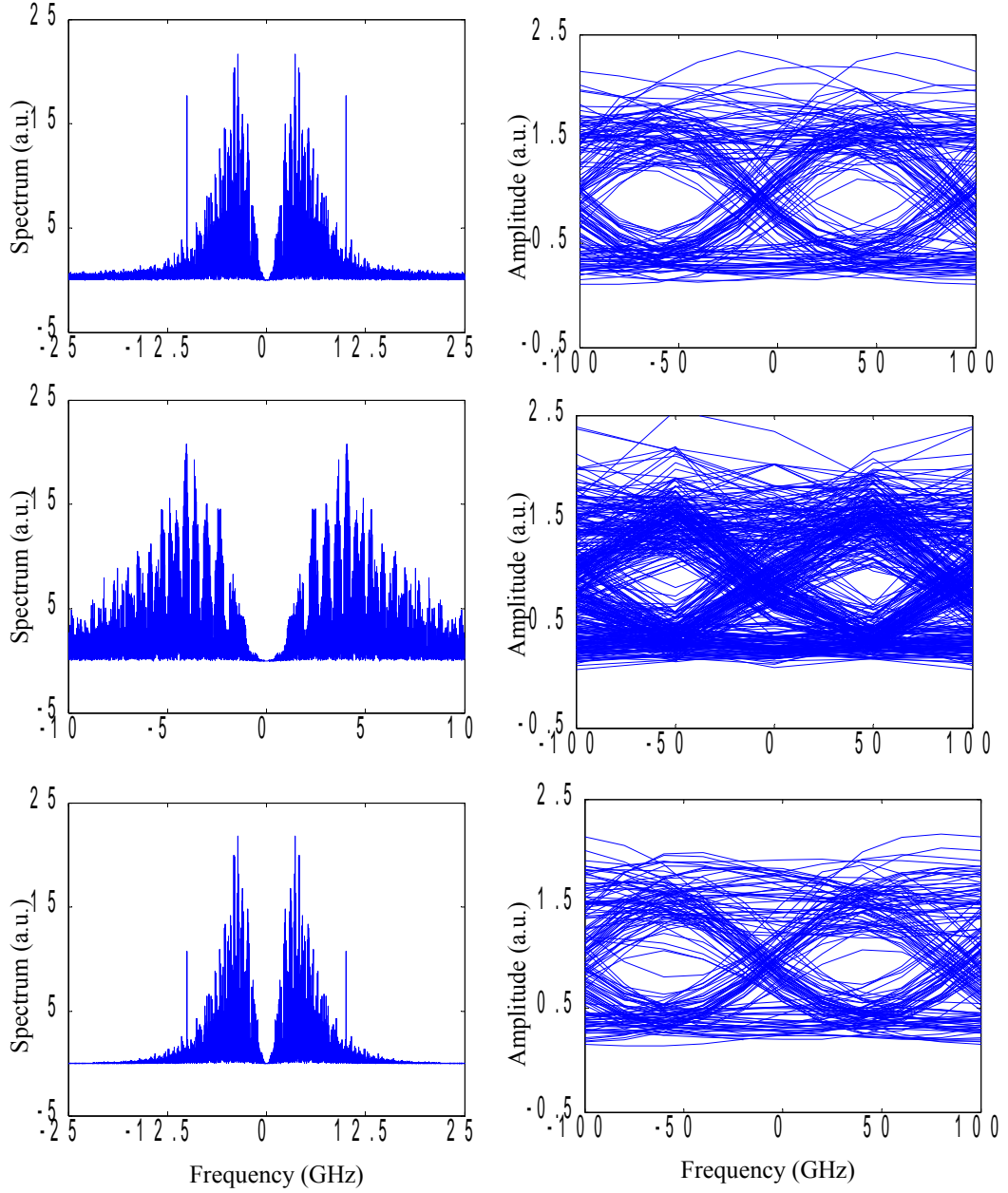
Figure 76: The spectra of Vf(t) [(a)-(c)] and the eye diagrams of the signal after dispersion compensation [(d)-(f)] at Fibre length of 2160km and 20dB OSNR. (a) and (d): 15GHz EFs and 50Gsamples/s;; (b) and (e): 15GHz EFs and 20Gsamples/s; (c) and (f): 7GHz EFs and 50Gsamples/s.

For 2160 km, the OSNR penalty for 50 Gsamples/s is less than 0.5 dB compared to that for 400Gsamples/s. From the Figure, it is also shown that the for the sampling rate less than 50 Gsamples/s, the slope of the OSNR increase is dependent on the fibre length, with the case of 2160 km more sensitive to the sampling rate, reflecting

121

the increased high frequency content of $V_f(t)$ for longer distances.

5.11   Sanity Check – VPI 7.5 Simulations

Initial simulation verifying the concept of Full Field signal reconstruction were carried out using VPI Transmission Maker 6.5 (Section 3.5). These simulations had limited abilities to simulate electronic dispersion compensation as the ability to export data to MATLAB was unavailable. In order to develop electronic signal processing algorithms suitable for use with the full field receiver, it was necessary to employ a MATLAB simulation model of both the optical and the electronic components. to expiate the development of the optimum electronic signal processing algorithms. Whilst the dominant physical mechanisms for optical transmission are well understood, and every effort was made to ensure MATLAB simulations were accurate, the simulator was not rigorously verified against an appropriate range of experimental conditions. As a step towards this verification, comparative simulations are run by embedding DSP run in MATLAB in a VPI optical simulation. Final verification is, of course, with experimental configuration, as reported in following sections.

The simulation set-up is shown in Figure 77. The transmitter used was a MZM with a maximum extinction ratio (as defined by VPI model) of 30 dB modulated by PRBS $(2^{11}-1)$ with a rise time of 25 ps and the bias and drive amplitude are adjusted to give various extinction ratio which are monitor by a single photodetector and electrically signal analyser. The laser used has a 2 mW output and a 10 kHz linewidth. This is a very narrow linewidth The launch power into the spans is controlled by a amplifier. The fibre model used is the unidirectional fibre model which takes into account

unidirectional signal flow. It includes the PMD and polarisation dependence of non-linear effects. There are four links each with a wide band filter to simulate the dynamic gain equaliser in the loop with a band width of 40 GHz and an amplifier.
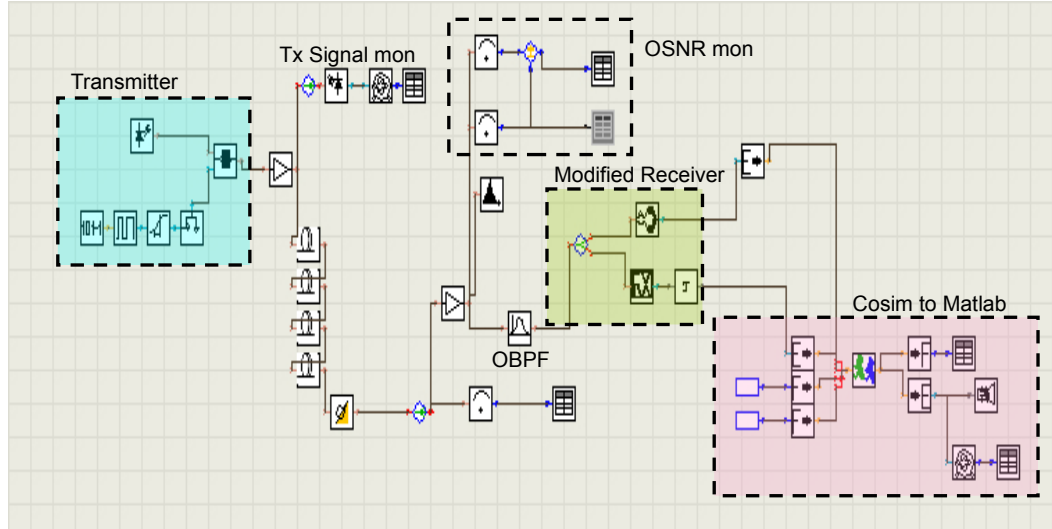
Figure 77: Screen shot of VPI simulation

The receiver consists of a optical Gaussian band pass filter with a bandwidth of 30 GHz follow by a 90:10 splitter into a single photodetector with a bandwidth of 15 GHz and a modified Rx_DPSK (a supplied simulation module) where the time delay can be varied as a schematic parameter and which has a detector bandwidth of 20 GHz. The outputs of these are passed to MATLAB via a co-simulation module and are processed using off-line processing program that is identical to the one used on the experimental data and in the MATLAB simulation. The processed data is returned to VPI where Q factors are determined and eye diagrams is displaced. The calculated error rate by direct error counting is also returned.
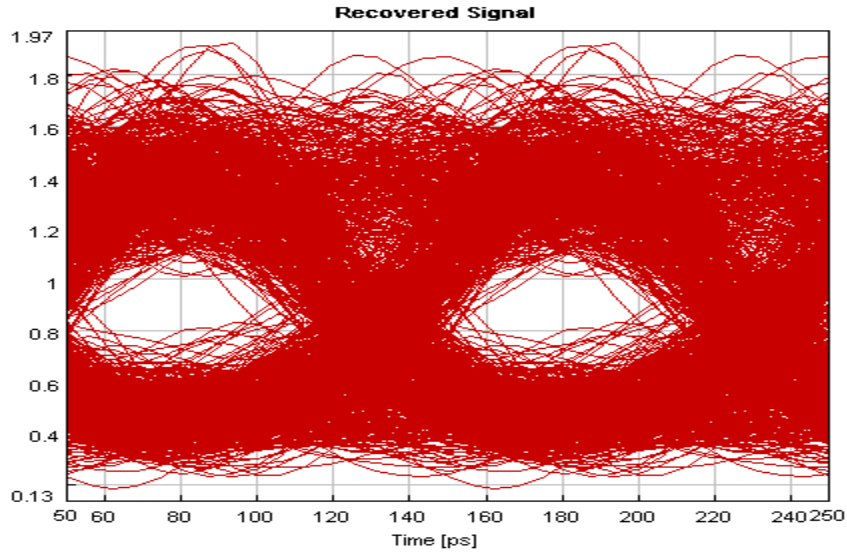
Figure 78 eye diagram for four 120 km spans of transmission with a MZM extinction ratio of 6 dB, launch power per span of 3 dBm, and a received Q-factor of 11.7 dB for an OSNR of 21.1 dB

Figure 78 shows a typical recovered eye diagrams for propagation very similar to the experimental set-up that will be described next. It shows a good open eye with a non-dispersed shape. It shows a very similar shape to that of the experimental eye diagrams shown in Figure 90. This gives very similar performance to the MATLAB simulation which for 6 dB extinction ratio, 120 km spans, 0.3 nm receiver filter result in a 21.5 dB required OSNR (Figure 70)

In section 5.6 , it was shown that increasing the time delay of the AMZI results in enhanced performance in the presence of thermal noise. Results were presented showing the improvement for 10 ps and 30 ps AMZI (Figure 69). Using the VPI simulation, this investigation is extended. Figure 79 shows the performance of the full field detection for an received OSNR of 36 dB for 6 and 12 dB extinction ratio as a function of the AMZI time delay. The simulation was run using a 2048 bits to reduce the simulation run time. It shows that there is an optimum range. If the time delay is two small, then the signal incident on the receiver is very small and the

124

system will be dominated by noise. If the delay is too large as in the experimental demonstration, the phase estimation will be compromised as the linearity assumption of the slope of the frequency sensitive filter response will be invalid. The 6dB extinction ratio shows improved performance due to its tolerance to low frequency noise amplification.
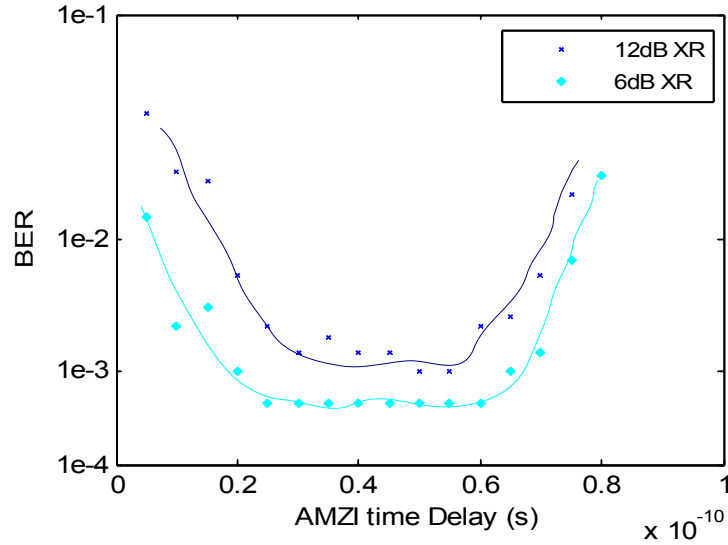
Figure 79: AMZI time delay vs. OSNR for 4x120km transmission

The impact of the OBPF bandwidth was studied In section 5.7 . Figure 80 shows the performance of the VPI simulation for different OBPF bandwidth for 6 dB extinction ratio for 480 km transmission. This shows a very similar response to Figure 70 for the same extinction ratio. It has an optimum filter bandwidth of 15 GHz and tails off with a comparable shape. The required OSNR is reduced for the VPI simulations. The majority of this difference can be attributed to the fact that the thermal noise of the balanced detector was reduced to $10*10^{-12} A/\sqrt{Hz}$ in the simulation. This was selected to reduce the influence of the thermal noise so that the effect of reducing the optical noise at the receiver could be isolated.
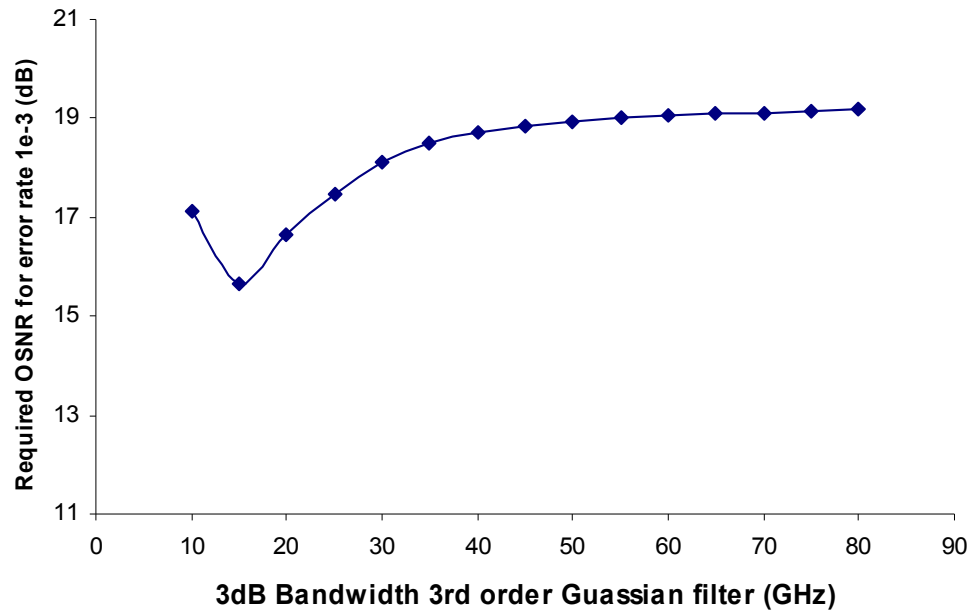
*Figure 80: Optical Band Pass Filter vs OSNR for 4*120km transmission*

5.12   Q-factor and BER

Q-factor is measured from the eye diagrams and is a quick method of determining transmission quality without having to synchronize patterns and optimize threshold levels. A method to calculate the Q-factor is described in section 2.3 . Because Q-factor does not use the actual data pattern and EDC operates at relatively high BER (as the implementation of FEC is assumed), it may not be a suitable estimation of BER. The VPI simulation typical produces two measurements of performance, the BER and the Q-factor. A VPI simulation was carried out using 65,538 bits with the simulation as described above and the following conditions - extinction ratio of 6 dB; AMZI delay of 30 ps; OBPF bandwidth of 30 GHz; 120 km spans; balanced detector thermal noise of $100*10^{-12}$ A/$\sqrt{Hz}$ and conventional detector thermal noise of $10*10^{-12}$ A/$\sqrt{Hz}$; per span launch power of 3 dB. .
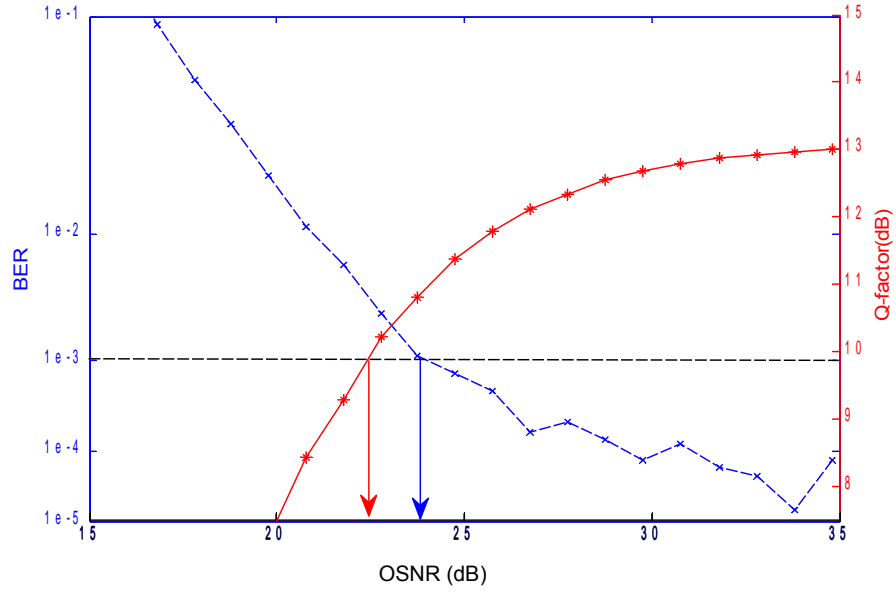
(a)
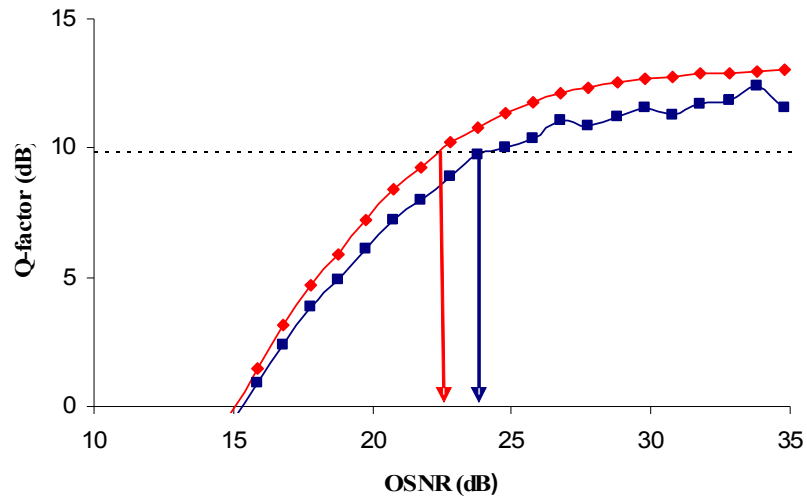
(b)

Figure 81: Q-factor and BER measurement for 4*120km VPI simulation VPI calculated (red) Q-factor and Direct Error counting returned from MATLAB (blue)

Figure 81(a) plots BER estimated by direct error counting and Q-factor estimated by the built in VPI module on separate axis. Figure 81(b) compares the Q-factor generated by converting the error rate using

$$Q_{factor} = 20\log\left(\sqrt{(2)} * erfc^{-1}(2 * BER)\right) \qquad (62)$$

with the VPI Q-factor. This gives a Q-factor of 9.78 dB from direct error counting

127

[140]. It can be seen that the VPI Q-factor underestimates the bit-error rate by between 1.7-2 dB. This must be kept in consideration when examining any results. The BER, however, depends on the joint optimization of a number of processing parameters while Q-factor depends only on eye shape. The accuracy of the BER is limited also by the sample sizes that are considered. Thus while Q-factor is a quick and easy way of estimating system performance, it is important to examine the actual BER rates as well. Q-factor is still a very useful tool for looking at trends in FF-EDC implementation.

5.13   Experimental Set-Up

Figure 82 shows the experimental set-up. A 1557.5 nm signal from a distributed feedback (DFB) laser was intensity modulated using a Mach-Zehnder modulator (MZM). The extinction ratio was controlled by varying the amplitude and bias of the drive signal to the MZM. This was measured and monitor as described In section 4.3.2 by a 10% transmitter monitor tap that is not shown in the figure. The recirculating loop in not shown in detail here for simplicity but its equivalent part representation is shown. The loop is described in detail in section 4.4 .

The received signal was pre-amplified and passed through a band pass filter. The signal was then split using a 90:10 coupler. 10% of the signal passed through a fixed optical attenuation and delay to the amplitude detector. 90% of the signal was passed through a variable optical delay line to the AMZI with a free spectral range of 85 GHz. The delay line was used to time align the phase and the amplitude signals. The variable optical delay line had a precision of ± 1 ps. It was necessary to use a variable alignment stage as optical and electrical delays were found to vary more strongly with temperature and re-connection.
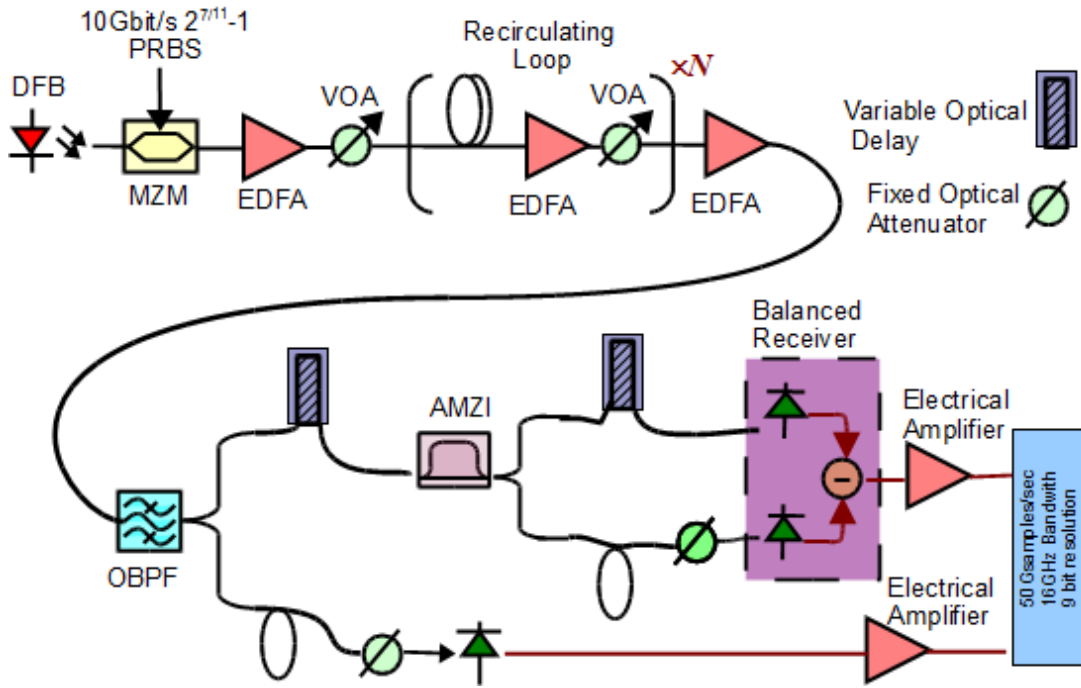
Figure 82: Experimental set-up.

The insertion of the delay line resulted in increase in the path length of *~2 m* so a length of fibre was placed in the amplitude path to ensure that the path length difference is within the tuning range of the time delay (*200 ps*). A fixed optical attenuator is also place here to protect the amplitude receiver from saturating. A similar time alignment set-up was necessary to match the output of the AMZI and the signal being detected by the two ports of the balanced detector. This signal alignment is necessary because the receiver was generated from individual components.

The loss of the phase estimation optical path was approximately 12dB. Thus to ensure optimum balanced detector performance, the power after the OBPF was monitored and also the currents of the two photodiodes of the balanced detector, to ensure that the performance was not dominated by thermal noise. Monitoring the currents of the balanced detector had the added advantage that when receiving a CW signal, equalising these currents was an accurate way of setting the AMZI to quadrature without disturbing the time alignment of the receiver.

The amplitude receiver had a bandwidth of 10 GHz and was followed by an electrical amplifier with 12 GHz bandwidth. The balanced detector had a 40 GHz bandwidth, and electrically amplified with a net amplification bandwidth of 15 GHz (Bessel Shape). Both detected signals were sampled by a real-time oscilloscope at a sampling rate of 50 Gsamples/s. The program for transferring the data from the oscilloscope is described in section 2.5

5.14   Preliminary Transmission Results Beyond the Dispersion Limit.[xii]

This section shows the first results for this technique using ADC and off-line processing. It shows that even without any adaptation of the basic algorithm greatly improved performance compared to uncompensated transmission may be achieved. The overall schematic is shown in Figure 60, and the specific parameters are detailed below.

The signal was generated with 12 dB extinction ratio and 10 Gbit/s 2^7-1 PRBS data. The generated OOK signal was transmitted over two looped 124km spans with a launch power of 0 dBm per span. Fibre non-linear effects were negligible (<< 1 dB penalty) for this fibre link configuration. At the receiver, the signal was pre-amplified and optically filtered by a 0.64 nm optical band pass filter (OBPF). 10% of the signal power was detected by a 10 GHz single photodetector and electrically amplified by a 12 GHz electrical amplifier. The remaining signal was optically processed by an AMZI with a 11 ps time delay and $\sqrt{2}$ phase shift. Off-line processing with 1,000,000 samples was used for optical field reconstruction and CD compensation. V_A and V_f in Figure 60 represent the estimated amplitude and frequency of the optical

130

field, respectively. Note that due to AC coupling, the bias of V_{up} was reset during off-line processing. A dispersive transmission line simulated the inverse transfer function of CD in the fibre, allowing for 85% compensation of the link dispersion. Figure 83(a) and (b) show the eye diagrams of the OOK signal after 248 km SMF transmission (a) without and (b) with EDC at OSNR of 24 dB (0.1 nm resolution). In the figure, the eye under conventional direct detection is completely closed. However, following digital processing of the received signal, the 10 Gbit/s OOK signal after 248 km SMF can be successfully recovered, with the Q-factor improved from -4.4 dB to 11.4 dB. This Q-factors were calculated from the actual bit error rates.
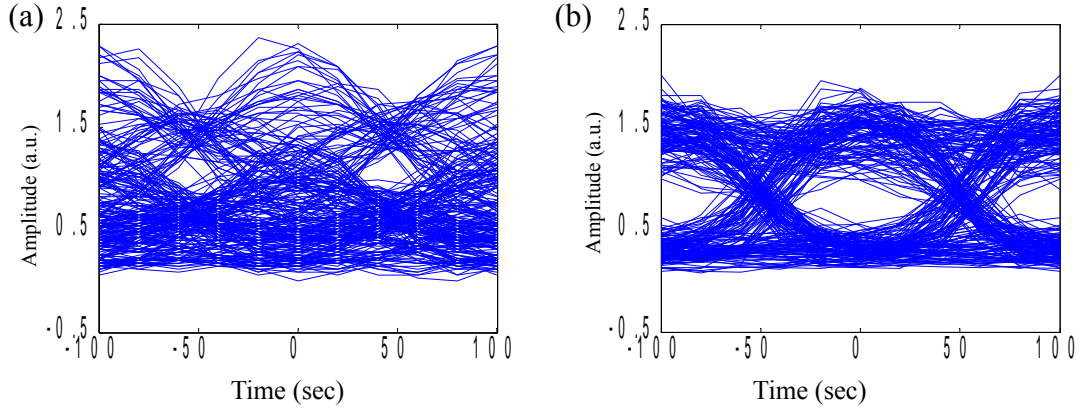
Figure 83: Eye diagrams of the OOK signal after 248km SMF transmission (a) without and (b) with EDC at OSNR of 24 dB.

It should be noted that the compensation parameters (compensation ratio, effective bandwidth, scaling of V_x and V_y) were not optimized for this system. It was shown in section 5.6 that the thermal noise of the 40 GHz balanced detector degrades the performance, and the Q-factor after EDC may also have been degraded by imperfect AMZI bias and timing alignment between V_x and V_y. Consequently, improved EDC performance may be expected. A large proportion of the degradation is due to inaccuracies in the phase estimation due to low frequency noise being amplified in

131

the frequency estimation path (Section 5.4).

5.15   Transmission Limited by Low Frequency Noise in V_f

The effect of inaccuracies in the estimation V_f are shown in section 5.4 to have a very strong influence on the performance of the system. This bandwidth of this filter may be optimised to provide optimum performance balance between noise suppression and signal distortion. This is shown Figures 90 and 91 which have been kept with their respective experimental set-ups to prevent duplicating descriptions. Figure 84 shows eye-diagrams with and without the filter. It is difficult to distinguish the improvement in performance but the eye with the filter is more open.
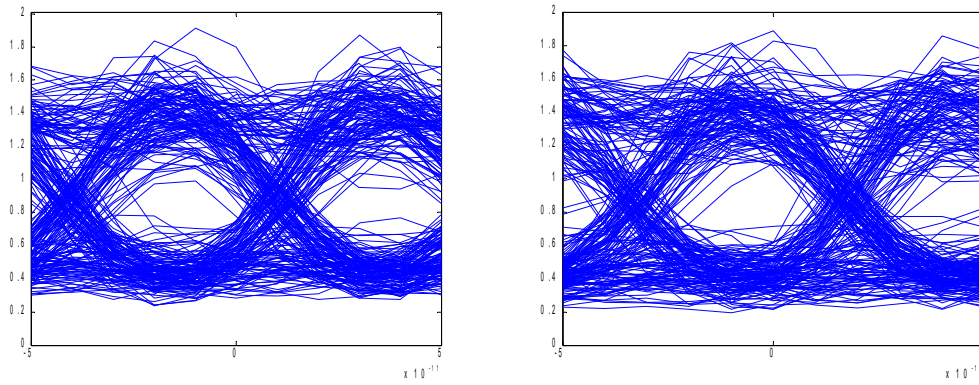
Figure 84: eye diagrams at 22.63 dB OSNR after 496 km transmission (left)without filter (right) with filter

5.16   Effect of Patterns on Reconstruction[iv]

With noise limited receiver side dispersion techniques, the most vulnerable bit to recovery is a isolated logical '1' surrounded by strings of '0's . This is because as this isolated bit becomes dispersed, its amplitude spreads out into the neighbouring bit slots and its' amplitude becomes negligible compared to the detected noise. This section investigates this phenomenon and presents on analysis of how the degree of

isolation (number of zeros on either side of the logical '1') affects the likelihood of a pattern dependent error occurring.

The amplitude and frequency signals were both sampled by a real-time oscilloscope at 50 Gsamples/s. Off-line processing with 5,000,000 samples was used for optical intensity and phase recovery. A Gaussian-shaped high-pass filter was used to suppress the low-frequency component amplification, as verified by Figure 85(a) and (b), eye diagrams of the compensated signals for 2^{11}-1 data pattern at fibre length of 496 km (a) without and (b) with a 1.2 GHz high-pass filter. $V_x(t)$ was re-biased to allow for the AC coupling of the receiver and $V_y(t)$ was re-scaled to correct for the different gains of the $V_x(t)$ and $V_y(t)$ signal paths.

Figure 85(c) and(d) illustrate the experimental intensity captures of a data sequence that contains an isolated '1' (c) without and (d) with EDC after 496 km SMF transmission. N_{before} and N_{after} represent the number of consecutive '0's before and after the isolated '1' respectively. From Figure 85(c), it can be seen that a typical isolated '1' following 496 km transmission results in a low optical intensity in that region. Consequently, it is expected that the poor signal-to-noise ratio would increase the uncertainty in both the extracted intensity and the instantaneous frequency, which would hinder the reconstruction of such isolated '1' bits. As a result, the isolated '1' might result in erroneous decisions, even after EDC if conventional threshold detection is used.
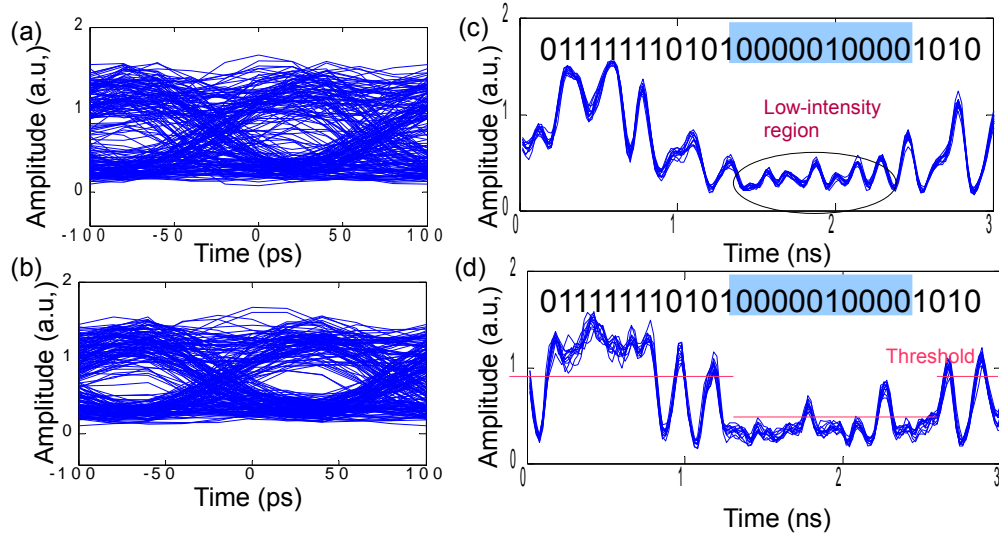
Figure 85: (a) and (b): Eye diagrams of the compensated signal with 2^{11}-1 sequence at 496 km and 26.4 dB OSNR (a) without and (b) with a 1.2 GHz high-pass filter; (c) and (d): a data sequence that contains an isolated '1' in a signal with 2^{11}-1 sequence at 496 km (c) without and (d) with EDC.
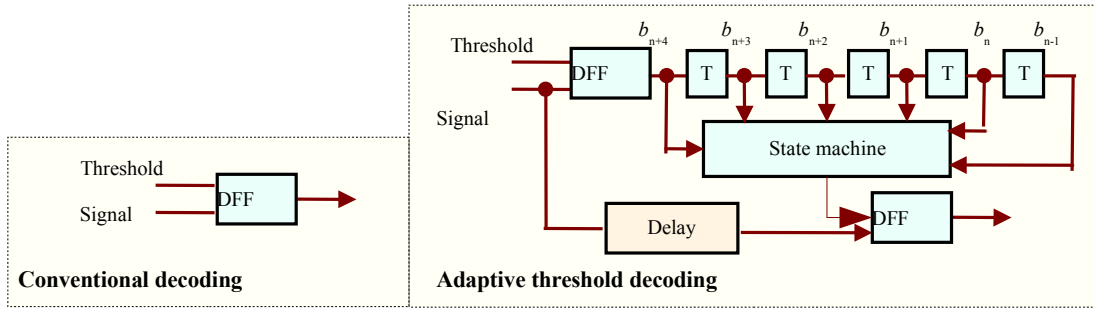
Figure 86: Decoding structures

This pattern sensitivity may be alleviated by using appropriate line coding in a practical system to reduce the number of such sequences at the expense of a certain amount of overhead. In order to avoid this overhead, a receiver-side mitigation technique may be used to adaptively employ a lower threshold for sequences containing a single isolated '1' and a higher threshold for elsewhere, as proposed here. This adaptive threshold detection (ATD) can be viewed, in a certain extent, as a simple line decoder without the sacrifice of net data rate and the transmitter-side encoder module. As illustrated in Figure 86, a D-flip flop (DFF) was used to perform an initial bit estimate, with the output data evaluated by a state machine. The state machine has two states representing two output values and is initially pre-set at state '1' with output of threshold '1'. When a sequence containing a single isolated '1' occurs, the first DFF may erroneously detect it as a long string of consecutive '0's due to low intensity of the isolated '1'. The state machine determines if the initial estimate suggests a chain of consecutive '0' bits and under this condition changes its state to give threshold '2' in order to allow the detection of low-intensity isolated '1' bits. State '2' is held until the sequence of consecutive '0's ends. Table 2 summarizes the principle. In the table, b_i represents the logical data from the first D-flip flop. m, k determines the conditions which the decoder recognizes as a long string of consecutive '0's and are set to be 1 and 4 respectively. Threshold '1' and '2' are

135

higher and lower than that in conventional decoding. Note that the pattern dependent decoding failure influences the optimization of various system parameters besides threshold, such as $V_x(t)$ bias, compensation ratio, bandwidth of electrical high-pass filter, etc. In particular, the electrical high-pass filter suppresses the low-frequency component amplification but introduces signal distortions as well. Such distortion is more severe for the isolated '1' pattern because the poor OSNR in this region induces a lot of low-frequency components. The high-pass filter eliminates these low-frequency components and thus also reduces the energy or amplitude of the isolated '1' pattern.

Table 2: Truth Table of Adaptive Threshold Detection

State	Input	Action	Output
State '1'	$b_{n-m}...\&b_n\&...b_{n+k}=0$	Change state	Threshold '2'
	Else	Hold state	Threshold '1'
State '2'	$b_{n+m}\neq 0$	Change state	Threshold '1'
	$b_{n+m}=0$	Hold state	Threshold '2'

In the off-line processing, the parameters, including bias added to $V_x(t)$, scaling factor of $V_y(t)$, compensation ratio and thresholds '1' and '2', were adjusted to achieve a local minimal rather than the global minimal bit error rate (BER) for each set of data, due to complexity of global optimisation. This would correspond to an adaptive decision directed optimisation of the thresholds.

To quantify the issue a figure of merit is defined a normalized error probability (*NEP*) of a pattern as:

$$NEP_{pattern} \triangleq \frac{NE_{pattern}}{NE_{sequence}} \frac{NB_{sequence}}{NB_{pattern}} \tag{63}$$

where $NE_{pattern}$ (or $NB_{pattern}$) represent the number of errors (or bits) of the particular pattern in the observed sequence, whilst $NE_{sequence}$ (or $NB_{sequence}$) represent NE (or NB)

of the whole sequence. $NEP_{pattern}$ will be greater than one if a given pattern causes abnormally high errors. Figure 87(b) shows the occurrence probability of a pattern with a given degree of '1' bit isolation (min(N_{before}, N_{after})), whilst Figure 87(a) shows *NEP* following off-line signal processing of the received sequence. The dotted line in Figure 87(a) is an arbitrary fitted curve for all symbols showing the general trends with respect to isolation. The figure shows that *NEP* increases dramatically as the isolation increases to 4 after which it becomes steady, verifying the susceptibility of the EDC receiver to isolated '1' bits. Note that '1' bits with larger isolation ($^{24}_{124}$) occur less frequently in a signal with 2^{11}-1 sequence, which should therefore lead to reduced BER compared to a signal with 2^7-1 sequence. The occurrence probability of '1' bits with such large isolation in real data is $\sim 1/2^9$.
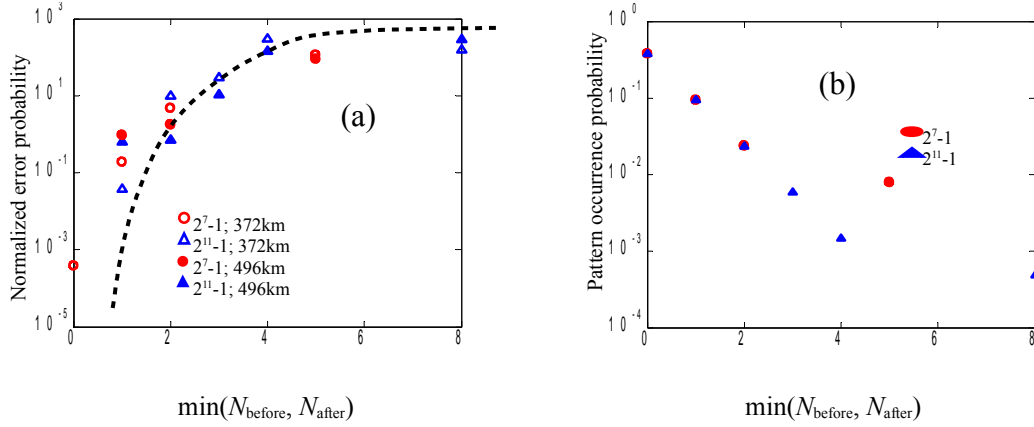
Figure 87: (a) Pattern occurrence probability versus min(N_{before}, N_{after}) for 2^7-1 (circles) and 2^{11}-1 (triangles) sequences. (b) Normalized error probability as a function of min(N_{before}, N_{after}) for 2^7-1 (circles) and 2^{11}-1 (triangles) sequences after 372 km (open) and 496 km (closed) SMF transmissions.

Figure 88 depicts $\log_{10}$(BER) versus OSNR for (a) 372 km and (b) 496 km field-installed SMF transmission. From the Figure, it is shown that by using 2^7-1 sequence, 372 km SMF transmission was unachievable. Analysis of the error distribution (Figure 87) showed that most errors were caused by the isolated '1' with min(N_{before}, N_{after})>2. For a signal with 2^{11}-1 sequence, the density of isolated '1' bit surrounded

137

by long strings of '0's was reduced, enabling a substantial performance improvement of full-field EDC with a $3.8*10^{-4}$ BER at 26 dB OSNR after 372 km SMF transmission. However, a significant number of errors were still induced by isolated '1' bits, which hindered further distance extension to 496 km. By using a 2^{11}-1 sequence and the adaptive threshold decoding described above, the errors from isolated '1's were further reduced. As a result, 496 km SMF transmission was achieved with a $3.3*10^{-4}$ BER at 26.4 dB OSNR.

(a)   (b)
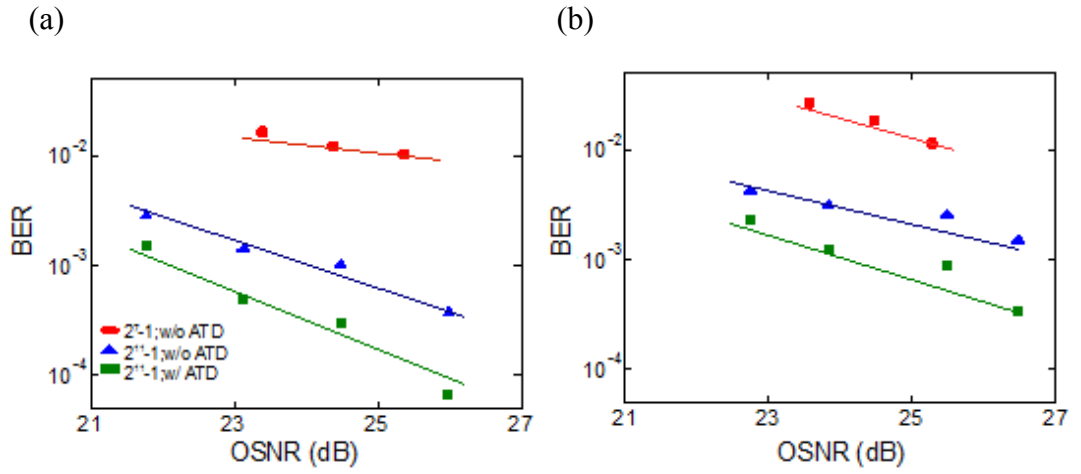
Figure 88: $log_{10}(BER)$ versus OSNR for (a) 372 km and (b) 496 km SMF transmission. Circles, triangles, and squares represent 2^7-1 sequence with conventional decoding, 2^{11}-1 sequence with conventional decoding, 2^{11}-1 sequence with adaptive threshold decoding, respectively.

This state based encoding system, while allowing an extension in transmission distance, does result in an increase in complexity of the receiver and further distance reach is not possible unless line coding is used to reduce the probability of isolated ones occurring. Such schemes are familiar in electrical communication systems where long strings of zeros result in loss of clock recovery. Line coding and the proposed adaptive thresholding may also be used in combination for optimum trade off between performance and overhead.

138

5.17   Improved Performance by Noise Suppression [v]

This is a receiver side based electronic dispersion technique and is therefore limited by received noise. This sections shows the impact a lower than typical optical extinction ratio. Another way of reducing the overall noise in the receiver is to use a very narrow bandwidth optical filter which will reduce the ASE noise incident on the receiver. A combination of these two alterations will be shown to give a performance very close to that predicted in simulation of the exact transmission system.

The important parameters and changes will be described here. The intensity modulation was at 10 Gbit/s using a 2^{11}-1 pseudo random bit sequence (PRBS). The extinction ratio was set to be either 12 dB or 6 dB by adjusting the amplitude of the electrical data. The generated OOK signal was transmitted over a recirculating loop comprising 124 km of field-installed standard single mode fibre (SSMF) in the BT Ireland network between Cork City and Clonakilty, County Cork, Ireland, with a signal launch power of around 0 dB per span. The signal polarisation was randomised after each recirculation using an Adaptif A3200-1 synchronous scrambler (POL). A 3 nm-wide band of ASE noise with spectral power density -20 dB less than that of the signal, located from 1550-1553 nm, co-propagated with the signal to ensure that the loop amplifier was appropriately saturated. The ASE noise was obtained from an erbium doped fibre amplifier (EDFA) filtered by an eight-channel arrayed wave-guide grating (AWG). A dynamic gain equaliser (DGE) was used in the loop to compensate for residual amplifier gain tilt. The spectrum profile of the signal and the ASE noise launched into the loop was shown in Figure 89. At the receiver, the signal was pre-amplified and optically filtered by either a 0.8 nm or a 0.3 nm OBPF. 10% of the signal power was detected by a 10 GHz single

photodetector and electrically amplified with a 12 GHz bandwidth.
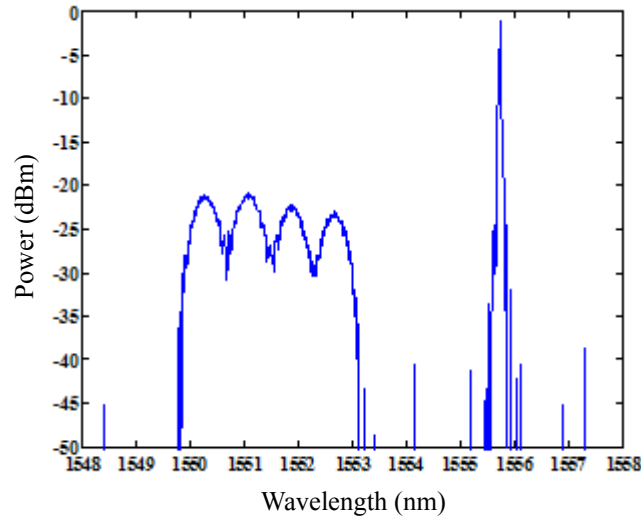
Figure 89: Spectrum of launched signal and co-propagated ASE noise

The remaining signal was optically processed by an AMZI with 11.76 ps (free spectral range (FSR) of 85 GHz) time delay and $\sqrt{2}$ phase shift, detected by a 40 GHz balanced detector, and electrically amplified with a net amplification bandwidth of 15 GHz. Both detected signals were sampled by a real-time oscilloscope at a sampling rate of 50 Gsamples/s. Off-line processing with 1,000,000 bits was used for optical intensity and phase recovery. Relative delays of the three signal paths shown in Figure 82 were fine tuned using optical delays placed prior to the detectors.

Figure 90 illustrates the performance of full-field EDC for a 12 dB extinction ratio and 0.8 nm OBPF (circles), and 6 dB signal extinction ratio and 0.3 nm OBPF (squares) after 496 km SMF transmission. To show the influence of high-pass electrical filter, the BER versus received OSNR without a high-pass electrical filter for the case of 6 dB extinction ratio and 0.3nm OBPF is also plotted (triangles). The insets show the eye diagrams of compensated signal (a) at 22.3 dB OSNR using 6 dB extinction ratio and 0.3 nm OBPF; (b) at 26 dB OSNR using 12 dB extinction ratio and 0.8 nm OBPF.
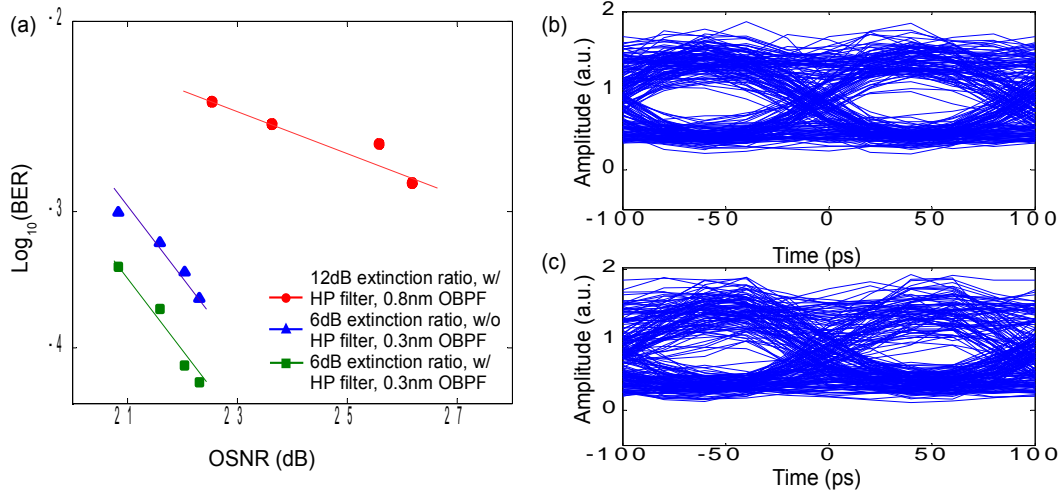
Figure 90: (a). log$_{10}$(BER) versus received OSNR after 496 km SMF transmission for 0.8 nm OBPF (circles) and 0.3 nm OBPF with (squares) and without (triangles) high pass filtering. (b) and (c). Reconstructed eye diagrams with high pass filtering (a) at 22.3 dB OSNR with 6 dB extinction ratio and 0.3 nm OBPF (left) and (b) at 26 dB OSNR with 12 dB extinction ratio and 0.8 nm OBPF (right).

From the Figure, it may be observed that 496 km was not achievable using 12 dB extinction ratio and a 0.8 nm OBPF. This was because ASE noise was not properly suppressed by the relatively wide bandwidth of the OBPF. Such noise not only directly degraded the quality of the photodiode outputs but also severely affected full-field reconstruction via the noise amplification mechanisms arising from the division by the total received power in phase estimation and low-frequency component amplification. By using a 6 dB signal extinction ratio and 0.3 nm OBPF, significant performance improvement was obtained. This improvement is primarily attributed to a reduction of ASE noise due to narrower bandwidth of the OBPF. Note that whilst the 0.3 nm OBPF suppressed the impact of ASE noise, the optimum filter width is narrower (~0.1 nm), as will be shown in the next section. The resultant excess noise associated with 0.3 nm OBPF increases the significance of the noise amplification process which in turn greatly impacts the optimum extinction ratio. Consequently, a reduced extinction ratio of 6 dB would result in the minimum value

of sampled version of $V_x(t)$ being increased, greatly suppressing the noise amplification arising from the division of $V_x(t)$ in the estimation of $V_f(t)$.
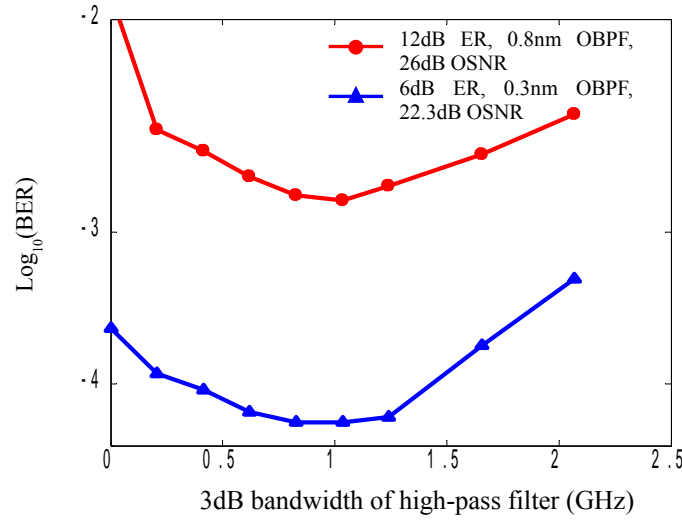
Figure 91: log$_{10}$(BER) versus bandwidth of high-pass filter. Circles: 12 dB signal ER, 0.8 nm OBPF, 26 dB OSNR; Triangles: 6 dB signal ER, 0.3 nm OBPF, 22.3 dB OSNR.

The use of a high-pass filter as discussed in section 5.15 and used during full-field reconstruction can suppress the low-frequency component amplification and improved the compensated signal quality, as shown in Figure 91. The level of improvement afforded by the high-pass filter is clearly dependent on the noise level, and in the case of 6 dB extinction ratio with a 0.3 nm OBPF where the noise has already been significantly suppressed, the benefit of the high-pass filter was not prominent. However, when the noise was not properly reduced (in the case of 12 dB extinction ratio and 0.8 nm OBPF), the employment of a high-pass filter was essential to suppress low-frequency component amplification of the noise. As a result, BER exhibited over one order of magnitude increase when the filter was removed. The figure also shows that the optimal cut-off frequency of the filter was around 1 GHz for both extinction ratio.

It has been experimentally demonstrated full-field EDC technique to achieve a bit

error rate of $5*10^{-5}$ at 22.3 dB OSNR for OOK signal after 4 spans of 124 km (496 km total length) field-installed SSMF by effectively suppressing the impact of ASE noise and the associated noise amplification. If this is compared with the results presented in Figure 70 for the 0.3 nm filter, this shows that this performance is OSNR limited for this filter bandwidth and AMZI length. The simulated OSNR is 21 dB and therefore results in a 1.3 dB penalty due to experimental imperfections.

5.18 Comparison of Experimental and Simulation Results

In section 5.3 , a simulation model developed in MATLAB is presented which is used to analysis the mechanisms at work in this proposed receiver. In this section, this model is tailored to mirror the experimentally set-up as closely as possible. The simulation uses a straight line link of 120 km spans. The launch power per span is 0 dBm and the power incident on the receiver was varied from from 0 dBm to 3 dBm as this is an important parameter is determining the influence of thermal noise on the effectiveness of the reconstruction. The AMZI delay was 10 ps and the OBPF at the receiver was 0.3 nm. The off-line parameters were optimised. For the simulations, the off-line parameters were the same for all OSNR values while for the experiment, the parameters were optimized for each set of data. This was done to account for equipment variation due to temperature fluctuations and drift in biasing voltages which are less than the precision of the equipment control. However as shown in Chapter 4 and in section 5.19 , variations in off-line parameters and experimental parameters such as DC offset, exact sampling phase and high pass filter bandwidth, may all contribute to an error of required OSNR. This error was estimated by an

allowance of approximately ±0.3 dB. In Figure 92, this potential error is added to the error bars for each point (arising from the confidence interval for the actual BER given the finite sample size). Figure 92 shows that for ±0.5 dB margin in the power incident on the receiver over 4 dB change in OSNR, the experimental results are very well predicted by the simulation. The FEC limit is given as being $1*10^{-3}$ which results in a Q-factor of 9.79. This gives a 0.8 dB margin for the 22.3 dB OSNR point to the FEC limit which is the same as when considering the BER representation indicating that Q-factor is a reasonable representation of performance in this case. The PMD is 0.1 ps/√km for all links and Corning SMF-28e has a design value of ≤ 0.06 ps/√km and a maximum ≤ 0.2 ps/√km so while the simulations are not worst case, they do take a pessimistic value for PMD which would also degrade performance compared to experiment.
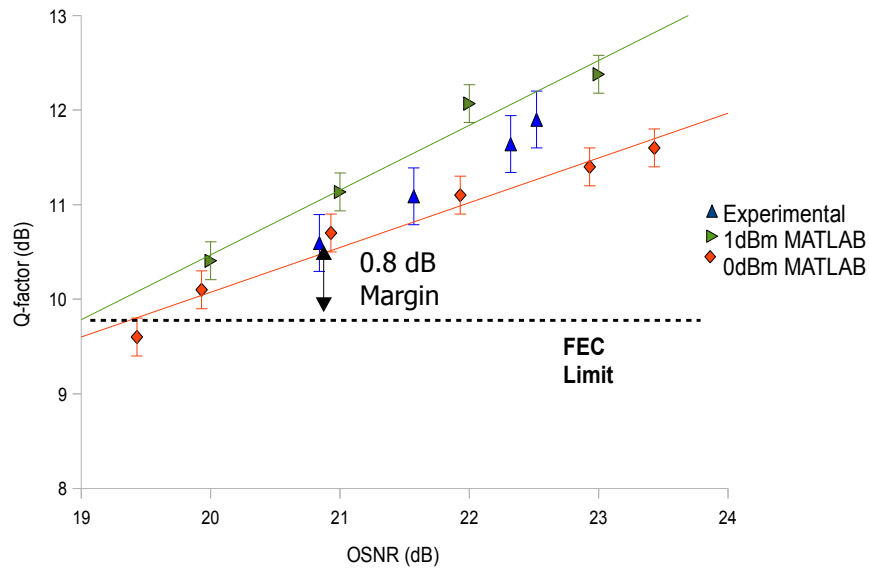
Figure 92: Q-factor of Experimental Results and MATLAB simulations with varying receiver incident power

In section 5.11 , a simulation model was described using VPI that simulated the experimental set-up closely. The highlighted differences are that the transmission link

simulated was a straight line link of 120 km spans with wideband 40 GHz filters before each in-line EDFA to simulate the action of the DGE in the link. The extinction ratio of the data was 6 dB, the AMZI had an 11 ps delay and the received OPBF is 3rd order Gaussian with a 30 GHz bandwidth. The OSNR was measured in 0.1 nm bandwidth. The incident power on the receiver is 0 dBm.
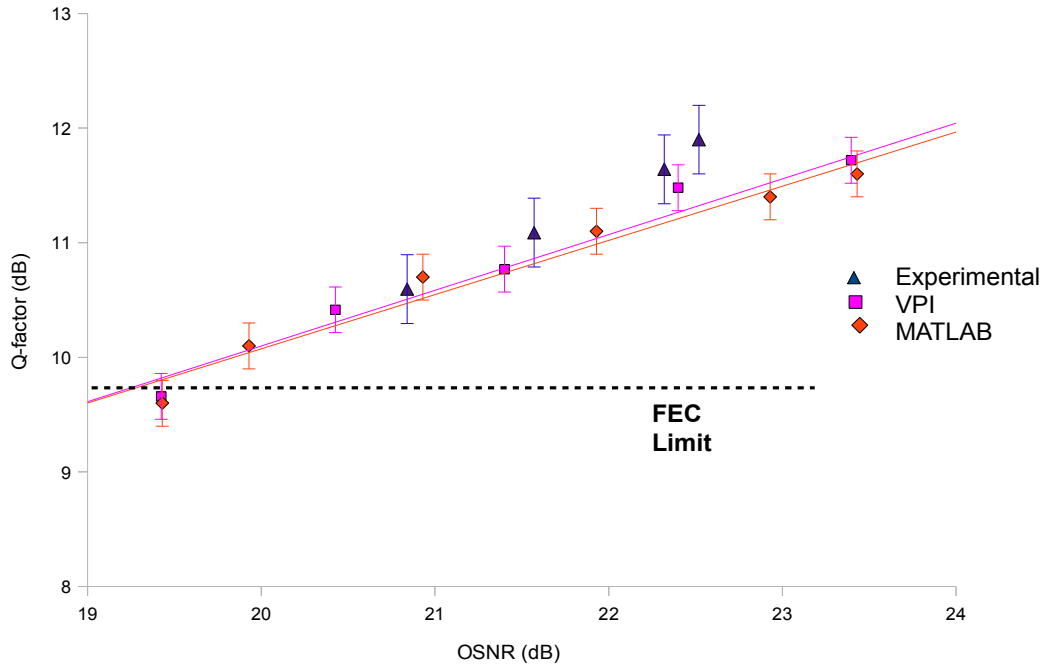
Figure 93: Q-factor vs OSNR for VPI simulations (magenta) and MATLAB simulations (orange) calculated with 0dBm received power and experimental results (blue). Q-factor for results are calculated from actual BER.

Figure 93 shows that if identical parameters are used, both simulation tools provide very good agreement with each other and the experimental results where it is believed that the slight difference between experimental and simulated results is due to the actual ratio of received power to thermal noise in the experiment (see figure 92). The VPI model is not extended here to look at different incident powers on the receiver. The optimization and expansion of the VPI model is on-going work in Tyndall National Institute.

5.19 Sensitivity to Off-Line Processing Parameters

The off-line processing used was described in detail in section 2.5 and results in a number of parameters which influence the performance of the technique. It is important to understand the sensitivity of performance to the tuning of these. This will of great practical importance in any implementation.

5.19.1 Compensation Length

The amount of dispersion compensation used is simulation by using a transmission line to match the transmission distance. Here the results are presented in Figure assuming a dispersion of 16 ps/nm/km.
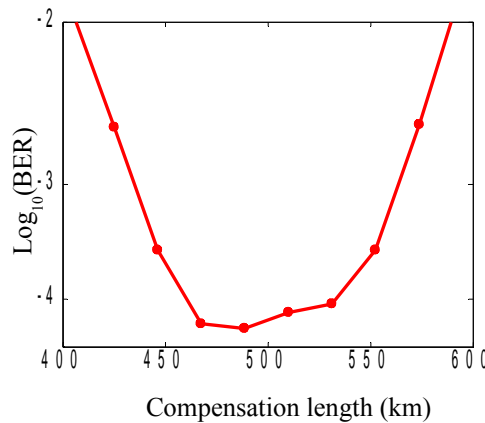
Figure 94: log₁₀(BER) as a function of compensation length for 6 dB extinction ratio and 0.3 nm OBPF after 496 km SMF transmission.

This illustrates that the tolerance range to errors in the estimation of the range of chromatic dispersion compensation. It is shown from the figure that the tolerance range at 496 km using full-field EDC is comparable to that of a signal at back-to-back without EDC. At the FEC limit (BER of 1×10^{-3}), the tolerance range is around 120 km. Alternatively when blindly estimating the distance it can be done in 120 km wide sections which should allow for fast acquisition for metro size distance.

5.19.2 Bias Coefficient M of V_A
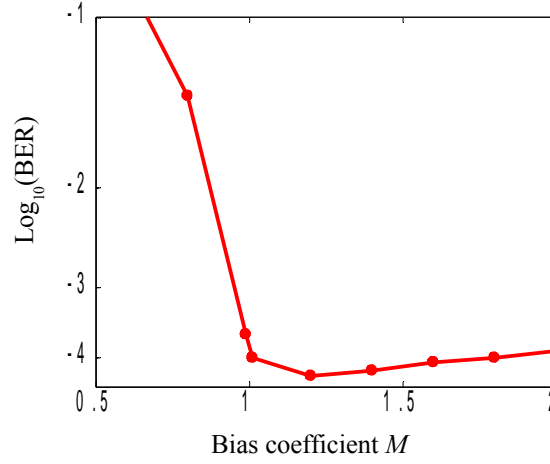
Figure 95: log₁₀(BER) as a function of bias coefficient M for 6 dB extinction ratio and 0.3 nm OBPF after 496 km SMF transmission.

Figure 95 shows performance variation as a function of normalized bias coefficient M, where the physical bias was $-M \times \min(V_x(t))$. The extinction ratio was 6 dB and OBPF had 3 dB bandwidth of 0.3 nm. Note that due to AC coupling of the receiver, $\min(V_x(t))$ had a negative value. From the Figure, it is shown that for proper operation of full-field EDC, it would be essential to bias the sampled values of $V_x(t)$ to a value larger than zero ($M>1$). This is because $V_f(t)=V_y(t)/(V_x(t)+bias)$ has ✓ phase shifts whenever the samples of $V_x(t)+bias$ changes from positive to negative and vice versa. When the noise amplification due to division by $V_x(t)+bias$ is suppressed ($M>1$), the system performance is robust to further bias increase. The optimal bias value balances the noise amplification and bias induced distortion to the estimated frequency. It also shows that this parameter has a soft tail-off as the bias is increased so bias should be kept above this threshold in a practical system and tuned only when compensation distance has first been fixed.

5.19.3   Phase Gain Parameter α

This parameter will be fixed depending on the receiver design parameters. As individual components are used, this needs to be tuned only when components are changed. This parameter compensated for different relative losses in the amplitude and phase paths in the receiver. Figure 96 shows the optimum phase gain parameter for the laboratory demonstrator. It is an important consideration in receiver design as there is a 4 decade penalty in going for α=1 to 4. If it increased beyond a certain point the noisy frequency estimation begins to dominates the performance.
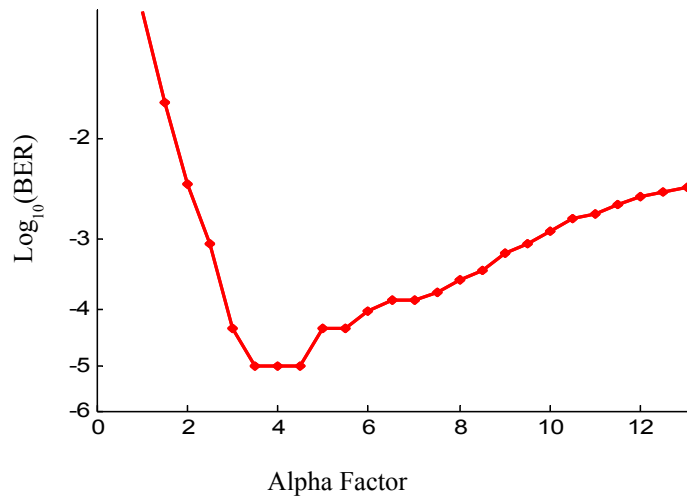
Figure 96: BER vs Frequency scaling factor α for 6dB extinction ratio and 0.3nm OBPF after 496km SMF transmission

5.19.4   Off-Line Clock Recovery Estimation

Due to the operation of the real time sampling oscilloscope, the sampling clock phase drifts over the time length of the data packet. Therefore clock recovery must be done after sampling. Note that future generations of oscilloscope and real time implementations are not expected to have this problem. The implications of sampling errors are shown in Figure 75 and Figure 97 illustrates the impact problem in a

typical data set. The optimum sampling phase changes ~10 μs and the bit slips every ~60 μs after 496 km transmission. Each line represents the error curve for each sampling phase and shows how it drifts into and out of optimum. Due to this the error rate for a particular measurement will be the slightly raised due to errors caused by when no sample phase is optimum. This indicates that real time measurement with a clock recovery and synchronized sampling would have an improved performance.
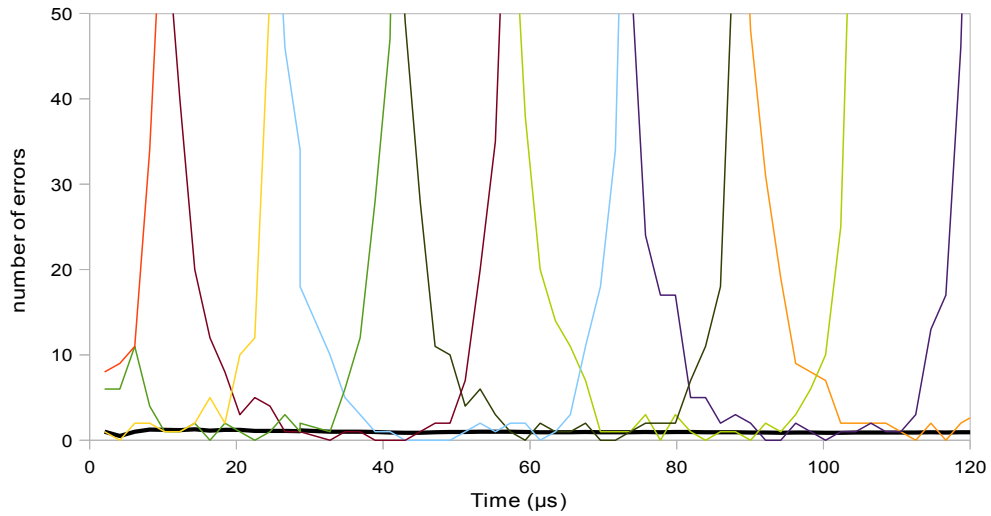
Figure 97: errors vs time for different sampling phases from a single measurement. The coloured lines are for different sampling phases and the black line shows the minimum number of errors recorded by using the optimum sampling phase.

5.20   Digital Signal Processing Simplification

Section 3.5.3 introduces a possible simplification of the off-line processing set-up in Figure 61 by neglecting the division of $V_x(t)$ which contributes to the extinction ratio and ASE sensitivity of the system. This simplification could greatly reduce the complexity of the system in practice because the intensity and phase estimation paths can be independently processed without synchronization until they reach the amplitude and frequency modulators in Figure 98.
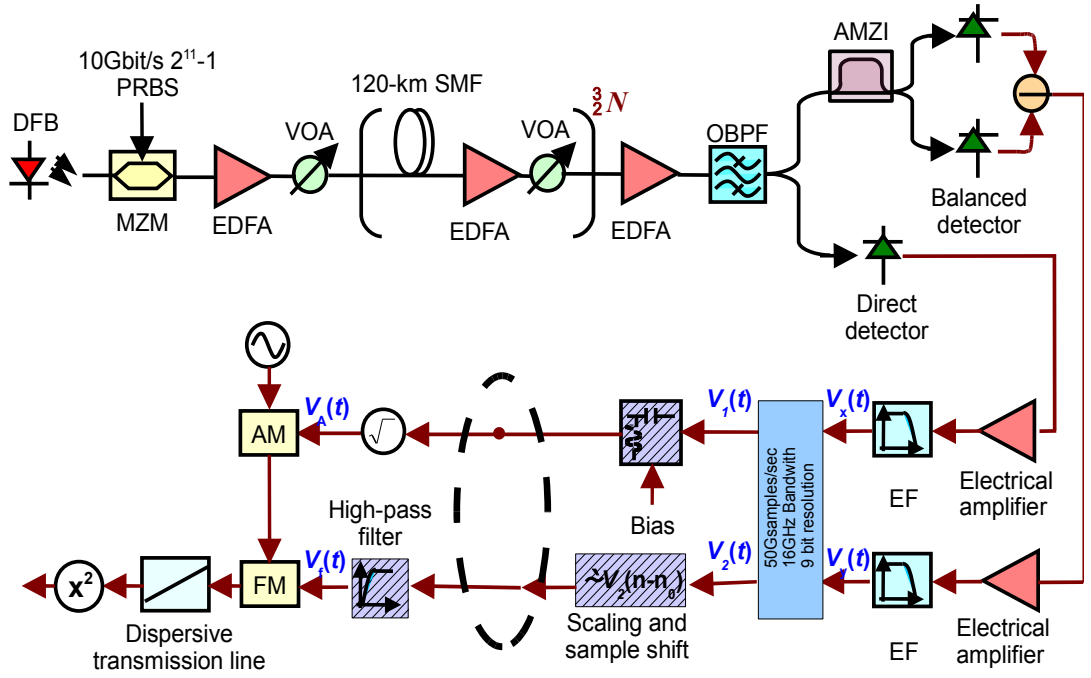
Figure 98: Schematic of set-up neglecting division

The system parameters optimized for the system including the division were used for this investigation. This simplification resulted in a small OSNR penalty of around 1 dB at BER of 1×10^{-3} as shown in Figure 99, which depicts the performance with (squares) and without (triangles) the division. This is in close agreement to previously simulated performance which indicated a 1 dB Q-factor degradation at 500 km with an 83 km amplifier spacing. At 496 km and 22.3 dB OSNR, FEC limit (1×10^{-3}) could still be achieved while implementation complexity was reduced, and further improvement is anticipated for a system optimized for this processing algorithm. The eye diagrams is shown in Figure 100. The rails are much thicker due to the inaccuracy arising from non-inclusion of the division operation.
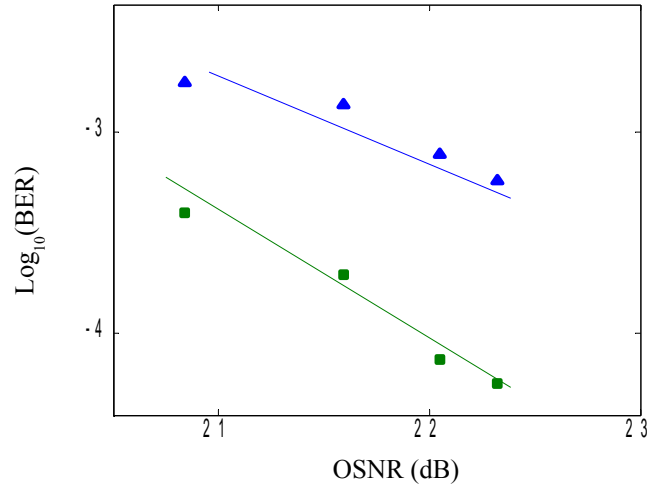
Figure 99: log₁₀(BER) versus received OSNR with high-pass filter(green) and without (blue) the division of $V_x(t)$. extinction ratio was 6dB and OBPF was 0.3nm. A 1GHz Gaussian-shaped high-pass filter was used.
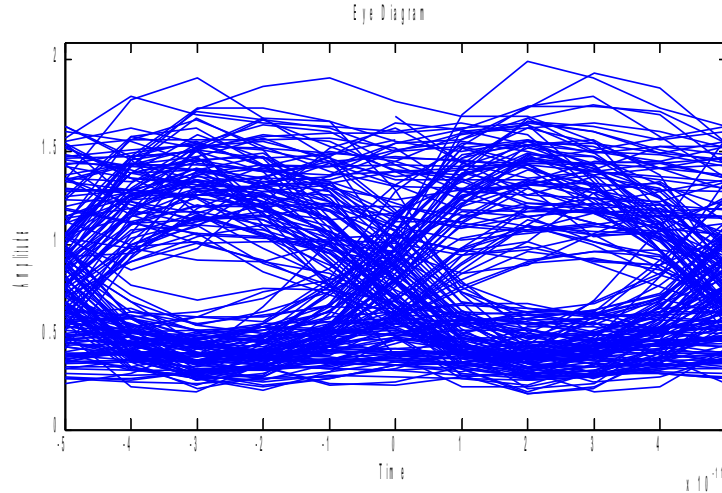
Figure 100: Eye Diagram 496 km no division 22.3dB OSNR

5.21   Conclusion

This chapter examined in detail the theory of full-field detection and dispersion compensation. The optimum parameters of a full field receiver are identified and lead to a theoretical reach of this technique of 2000 km. The system performance is analysed under different link conditions with different device imperfections. The system penalties due to each of these is investigated. The use of low extinction ratio

151

and high pass electrical filter to combat the amplification of low frequency noise which degrades phase estimation. The chapter demonstrated the reach of the technique experimentally beyond the dispersion limit and examined the sensitivity of the reconstruction to pattern dependent error due to extremely dispersed isolated '1's. The dispersion compensating properties of FF-EDC have been illustrated over 4 links of 124 km installed fibre showing that this is a practical and robust technique for even technically challenging metropolitan area networks. The MATLAB and VPI models are used to predict the performance of the experimental set-up used in this work and were found to agree with the experimental results within acceptable error margins. It illustrates a good understanding of the mechanisms which influence the reconstruction.

6 FD-EDC in Conjunction Full-Field Maximum Likelihood Sequence Estimation (FF-MLSE) Techniques

6.1 Introduction

This chapter considers the implementation of dispersion compensation using digital signal processing in conjugation with full-field reconstruction. Most EDC implementations [20,70-71,119] are optimised to achieve maximum performance with access to the amplitude alone. The exception are those which use coherent detection [62,68,86,90-91,94]. Maximum likelihood sequence estimation (MLSE) is one of the most promising techniques for dispersion compensation in optical transmission systems, due to its excellent compensation performance and fast adaptation to the fibre link conditions [14]. A 4-state MLSE receiver has recently been commercially implemented. Prior work has been based on MLSE using conventional direct detection, where the system performance is unavoidably limited by the loss of optical phase information before the application of MLSE. This typically caused ~3 dB penalty even when sufficient trellis states were employed to deal with the channel memory [72]. In this chapter, an EDC implementation (Maximum Likelihood Sequence [119-125] estimation (MLSE)) will be extended to consider the use of the full optical field.

6.2 Channel Model

This section is adapted from Section 10.1 of [126] and from the original papers. [[120]-[121]]

Inter-symbol interference arises in systems whenever the effects of one transmitted

bit are not allowed to die away at the receiver before the transmission of the next. In optical fibre transmission, dispersion will result in pulse spreading which will lead to a transmitted bit interacting with the light in the preceding and following bit-slots. For linear transmission as illustrated in Figure 101, dispersion can be considered to be a linear filter with a magnitude response of unity and a phase response, let this be represented by the impulse response

$$h(t) = e^{\frac{-i}{2}\beta_2 \omega^2 z} \tag{64}$$

which may be longer that the symbol rate T, and therefore the filtered signal is given by

$$s(t) = \sum_n I_n h(t - nT) \quad, \tag{65}$$

where I_n is the nth original transmitted binary symbol. The signal is corrupted by noise assumed to be additive white Gaussian noise (AWGN) $n(t)$ to give a received signal

$$r_l(t) = s(t) + n(t) \quad. \tag{66}$$

This is a statement that the received signal is the original transmitted bit acted on by dispersion and corrupted by noise. The duration of $h(t)$ is limited depending on the distance traversed. That is, the amount of significant pulse spreading increases with distance and therefore, so does the range of the inter-symbol interference.
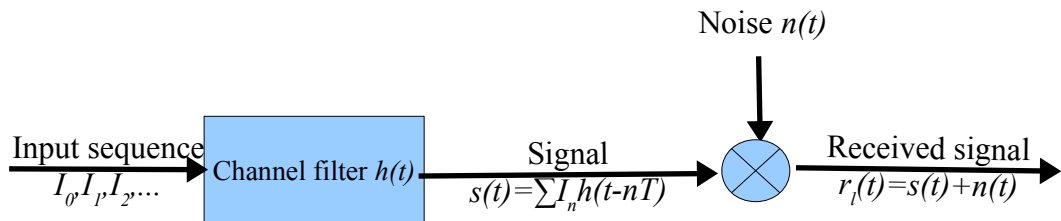
Figure 101: Communications System

The joint probability density function of the random variable, r_l, at the receiver is

conditional on the input sequence, I_P. As the number of random observation of the the random variable approaches infinity, the received probability metric may be written

$$PM(I_p) = -\int_{-\infty}^{\infty} |r_l(t) - \sum_n I_n h(t-nT)|^2 dt \qquad (67)$$

The maximum likelihood estimation of I_p is that which maximises (67). It is related to the calculation of the least mean squared error between the received samples and the expected sequence in the absence of noise. An efficient method to calculate the sequence I_P which minimises this mean square error is given below. (67) can be expanded to (details in referenced papers and in digital signal processing text books)

$$PM(I_p) = ...$$
$$-\int_{-\infty}^{\infty} |r_l(t)|^2 ...$$
$$+2\,\Re \sum_n [\int_{-\infty}^{\infty} r_l(t) h^*(t-nT) dt] ... \qquad (68)$$
$$-\sum_n \sum_m I_n^* I_m \int_{-\infty}^{\infty} h^*(t-nT) h(t-mT) dt$$

The maximum-likelihood estimates of the symbols $I_1, I_{2,} ..., I_p$ maximised this quantity. Examining the terms of (68), $|r_l(t)|^2$ is common to all possible sequences so can be neglected. Observing the second term, it can be generated by passing the received signal through a matched filter $h*(t)$ and then digitally sampled at a rate of $1/T$.

$$y_n \equiv y(nT) = \int_{-\infty}^{\infty} r_l(t) h^*(t-nT) dt \qquad (69)$$
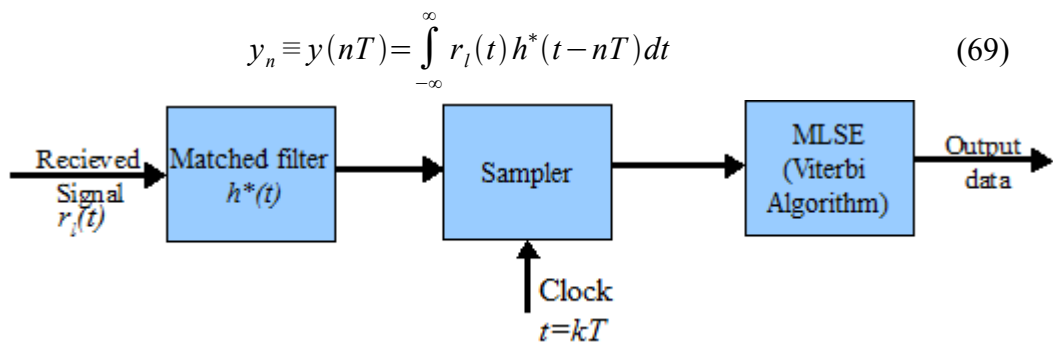
*Figure 102: Optimum receiver for an AWGM channel with IS*I

The samples y_n form sufficient statistics to compute (67) or equivalently the correlation metrics

$$CM(I_p) = 2\Re\left(\sum_n I_n^* y_n\right) - \sum_n \sum_m I_n^* I_n x_{n-m} \qquad (70)$$

where $x(t)$ is defined as

$$x_n \equiv x(nT) = \int_{-\infty}^{\infty} h^*(t) h(t+nT) \, dt \qquad (71)$$

where $x(t)$ is the autocorrelation of $I(t)$ realised as the output of a filter with an impulse response of $h^*(-t)$ and an excitation of $h(t)$. By substituting into (66) and using (65) and (69):

$$y_k = \sum_n I_n x_{k-n} + v_k \qquad (72)$$

where v_k is the additive noise sequence at the output of the filter. (72) can be illustrated as a state machine in Figure 103.
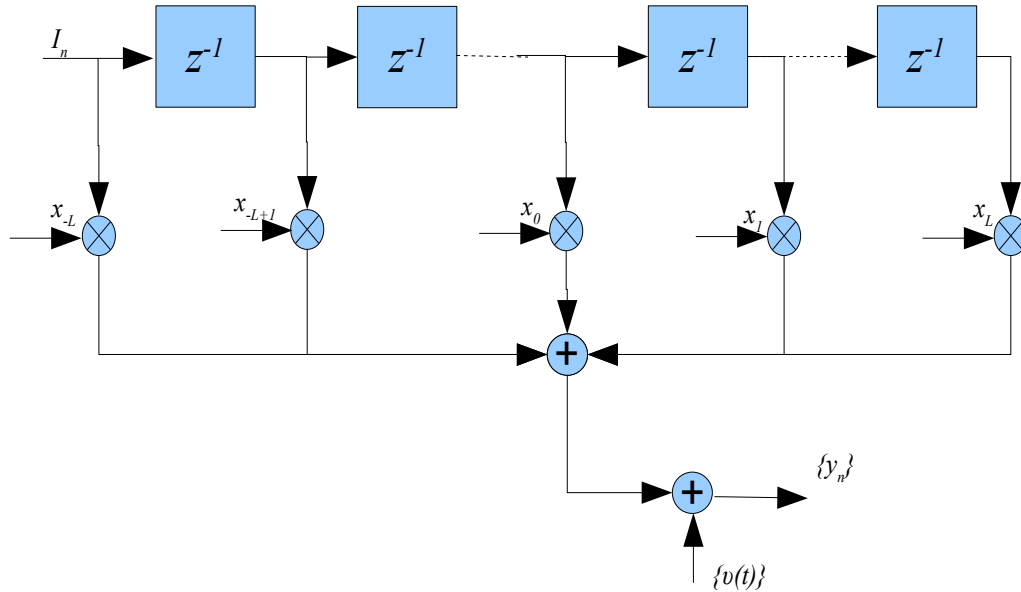
Figure 103: Equivalent discrete time model of the channel with inter-symbol interference

Assume that the amount of inter-symbol interference is limited as is the case with ISI caused by dispersion, $x_n = 0$ for $|n| > L$. Thus, it is possible to consider the output of the channel as a finite state machine and hence can be described as a trellis diagram

(Figure 104) and the maximum-likelihood estimation of the information sequence (*I*) is the most probable path through the trellis given the received demodulator output sequence *{y_n}*. The shortest path through a trellis has been previously used as a method of decoding convolution codes. The method which has been used in many applications is the Viterbi algorithm[120-121,127]. This can be used to calculate (70) recursively

$$CM_n(I_n) = CM_{n-1}(I_{n-1}) + \Re\left[I_n^*(2y_n - x_0 I_n - 2\sum_{m=1}^{L} x_m I_{n-m})\right] \qquad (73)$$

One of the major problems is the correlations of the noise sequence $\{v_k\}$ at the output of the of the matched filter. Therefore a noise-whitening filter must be determined – this is dealt with in detail in [120], in section 10.1.2. in [126] or any digital signal processing text book.

Let *X(z)* be the two sided *z* transform of the sampled autocorrelation function (69),

$$X(z) = \sum_{k=-L}^{L} x_k z^{-k} \qquad (74)$$

where $z^{-1} = delay\, of\, T$. Since, $x_k = x_{-k}^*$ it implies that $X(z) = X^*(z^{-1})$ and hence the roots are related allowing factorisation:

$$X(z) = F(z)F^*(z^{-1}) \qquad (75)$$

where *F(z)* and *F*(z⁻¹)* are polynomials of length *L*. By setting requirements for the digital filter to be physically real, stable and recursive. *1/F*(z⁻¹)* can be defined as the noise-whitening filter. By filtering the received signal $\{y_k\}$ by this results in an output sequence $\{v_k\}$

$$v_k = \sum_{n=0}^{L} f_n I_{k-n} + \eta_k \qquad (76)$$

which is referred to as the equivalent discrete-time white noise filter model of the cascaded transmitting signal, the channel, the matched receiver filter $h^*(-t)$, the

157

sampler and the discrete time noise whitening filter $1/F^*(z^{-1})$ which is a transverse filter with tap coefficients $\{f_k\}$.

6.3 Maximum Likelihood Sequence Estimation

The system can be imaged as a finite state machine with a memory depth of L and has 2^L possible states (S_k). The channel can therefore be described by an 2^L-state trellis. Thus the Viterbi algorithm can be used to determine the most probable path. The Viterbi algorithm (VA) was first described in [120] for decoding convolutions codes but was soon recognized as a solution to the problem of maximum *a posteriori* probability (MAP) estimation of the state machine of a finite-state discrete-time Markov process.

The state of the process at any time depends on the L most recent inputs:

$$S_k \triangleq (I_{k-1}, I_{k-2}, ..., I_{k-L}) \tag{77}$$

where $I_k=0$ for $k \leq 0$.

It is important to note that the mapping from input sequence I_k to state sequence s_k and further on to the resulting signal sequences v_k is invertible. That is two successive states uniquely determine an output.

$$y_k = y(s_k, s_{k+1}) \tag{78}$$

This results in the relationship, that an allowable state sequence S_k or received whitened signal signal sequence v_k is one such that it will result in an allowable input sequence. MLSE will be described in terms of the whitened received signal v_k.

The trellis search requires the calculations of metrics at every step. Using the observation samples $v_1, v_2, ..., v_{L+1}$, compute 2^{L+1} metrics:

$$\sum_{k=1}^{L+1} \ln p(v_k | I_k, I_{k-1}, ..., I_{k-L}) \quad . \tag{79}$$

The 2^{L+1} possible transmitted sequences are given by $I_{L+1}, I_L, ..., I_2, I_1$ which are

divided into 2^L groups or *states* which differ by I_l and are paths which converge to a single node on the trellis. For each state, a *survivor* is selected which has the largest probability which is assigned a metric

$$PM_1(\mathbf{I_{L+1}}) \Rightarrow PM_1(I_{L+1}, I_{1,.}.., I_2)$$
$$\max_{I_1} \sum_{k=1}^{L+1} \ln p(\nu_k | I_k, I_{k-1}, ..., I_{k-L}) \tag{80}$$

The remaining sequences are discarded and 2^L survivors and their corresponding metrics remain. This is repeated for the each new observation and now the sequences arriving at each node differ by $I_{1,} I_2$. So at each step into the trellis the surviving sequences extend but their number and the number of metrics calculated remain the same. This generates the follow recursive equation:

$$PM_k(\mathbf{I_{L+k}}) = \max_{I_k} [\sum_{k=1}^{L+1} \ln p(\nu_{L+k} | I_{L+k}, ..., I_k) + PM_{k-1}(\mathbf{I_{L+k-1}})] \tag{81}$$

Hence the 2^{L+1} metric calculated at each time step *t* are given by

$$PM_k(\mathbf{I_{L+k}}) = \ln p(\nu_{L+k}(t) | I_{L+k}, ..., I_k) + PM_{k-1}(\mathbf{I_{L+k-1}}) \tag{82}$$

As the received signal is essentially infinite, there will be a large delay in generating the estimation of the I_k, this is unacceptable in practice. At a delay of $\geq 5L$, the penalty optimum is negligible. Whether this is possible to implement in high speed electronics is an open question.

Figure 104 illustrates the evolution of the probabilities through the trellis. It shows a Viterbi algorithm with 4 states (*L=2*) with initially equal probabilities of being in any state. From each state there are two possible transitions in the next observation period. The bit sent may be a '1' or '0'.State 00 can be preceded by State 00 or State 10 by a '0' having been sent. Thus the probabilities of these two transitions are calculated and compared and the most probable path is retained. This results in the 4 states in the next time slot having slightly different probabilities. Again State 00 can

be reached by the transition from State 00 or 01, but State 00 has probability calculated above and State 10 is the more probable of the transitions given the observation from States 11 and 01, if a '0' was transmitted. Thus it can see that the number of states remains constant and the probability of paths through the trellis is build up as time increases.
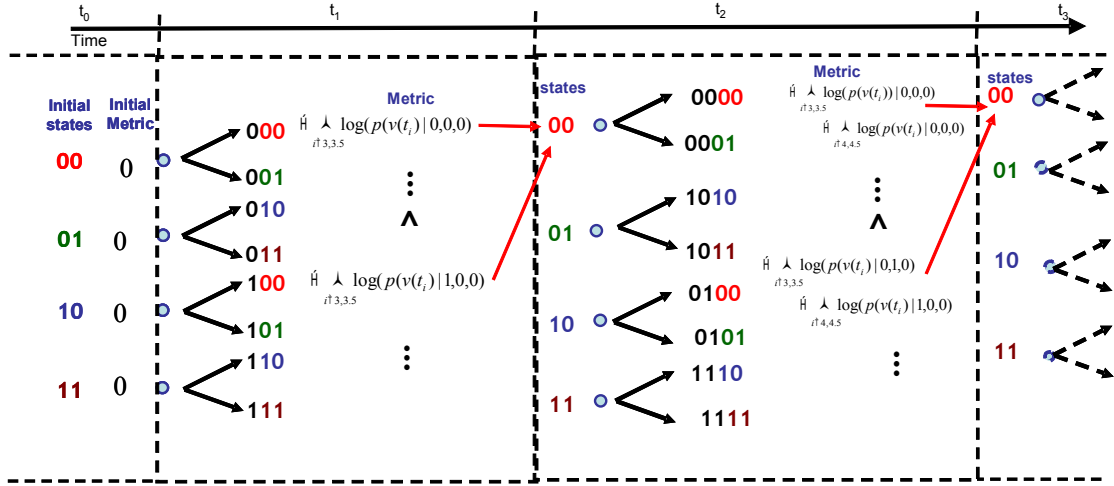
Figure 104: Illustration of trellis propagation

6.4 Full Field MLSE[xii]

This thesis has presented a low cost technique for accessing the amplitude and phase information of the received signal. This section proposes a novel field-detection MLSE (FD-MLSE) for chromatic dispersion compensation for an OOK modulation format. Figure 105 depicts the principle of the proposed FD-MLSE. The intensity $V_A(t)$ and the phase $V_f(t)$ of the optical field are extracted with a single AMZI using the method outlined in Chapter 3. The recovered intensity and phase information was then used to obtain the real and imaginary components of the optical field, which were synchronously down-sampled to two samples per bit. It should be noted that while this work only considers using the real and imaginary fields extracting using the phase estimation receiver described in this thesis, equivalently, these could be

160

generated using a digital coherent receiver followed by the blue box below in Figure 105.
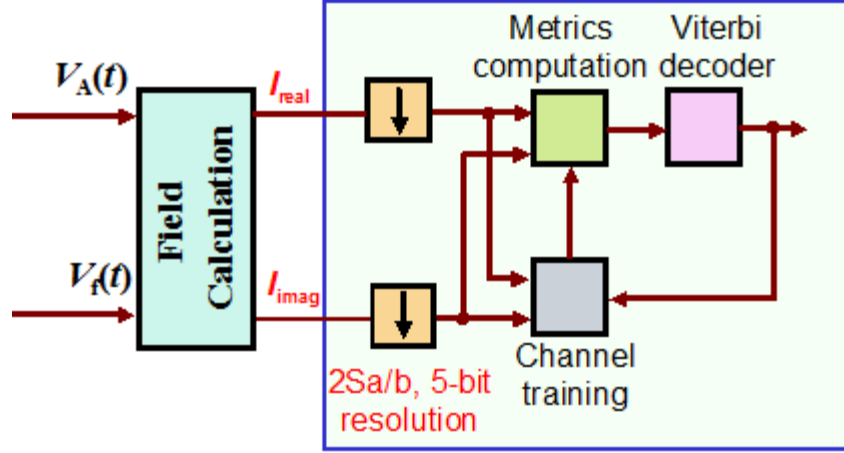
Figure 105: Principle of FD-MLSE receiver

FD-MLSE exploits the real and imaginary components simultaneously both in channel training and in metric computation. The metric of FD-MLSE, $PM(I_k)$, is:

$$PM_k(\boldsymbol{I_k}) = \sum_i \ln p(\Re(v_k(t)), \Im(v_k(t))|I_{L-k},...,I_k) + PM_{k-1}(\boldsymbol{I_{k-1}}) \tag{83}$$

where $i \times \{k \ k+1/2\}$. This differs from the previous section in that it is a fractional MLSE receiver. This has the advantage of being able to compensate without optimum phase sampling – i.e. greater than the Nyquist rate.

The initial metrics in the training table were obtained using the histogram method. Although the required memory for $\ln p(\Re(v_k(t)), \Im(v_k(t))|I_{L-k},...,I_k)$ was proportional to the square of the number of quantisation levels, q^2, the complexities of the metric computation and Viterbi decoding were the same as those of a DD-MLSE with the same number of states. The numerical model set-up is shown in Figure 107 which is used to prove concept and refine the monitoring algorithm. The link simulation is the same as that used in Chapter 5 but will be re-iterated here for completeness. Note that the refinements described in Chapter 4 to improve the phase

estimation and hence, the field calculation are retained.
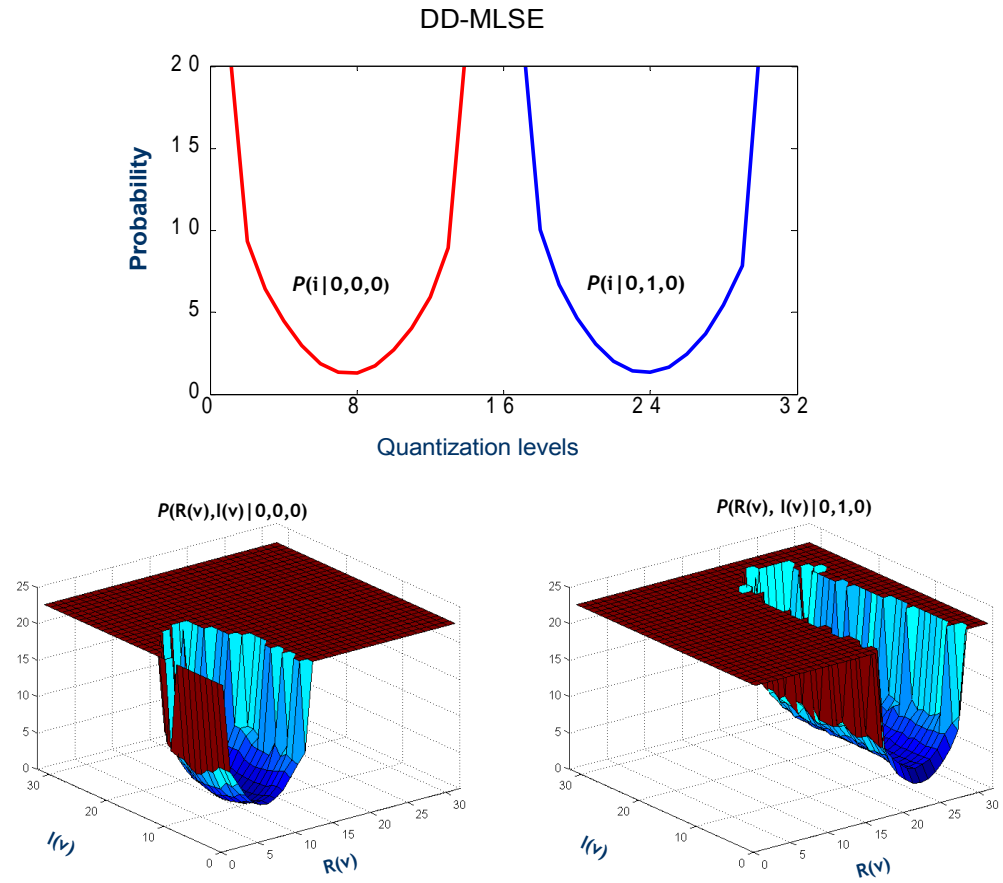
Figure 106: Examples of Theoretical Probabilities Distributions of '0' and '1' surrounded by '0's 0 km transmission for DD-MLSE and FD-MLSE from model described .

Continuous wave light was intensity modulated by a 10 Gbit/s OOK data train using a Mach-Zehnder modulator (MZM). The data train consisted of a 2^{11}-1 pseudo-random binary sequence (PRBS) repeated nine times (18,423 bits). 10 '0' bits and 11 '0' bits were added before and after this data train respectively to simplify the boundary conditions. The bits were raised-cosine shaped with a roll-off coefficient of 0.4 and 40 samples per bit. The extinction ratio of the modulated OOK signal was set to be 12 dB.
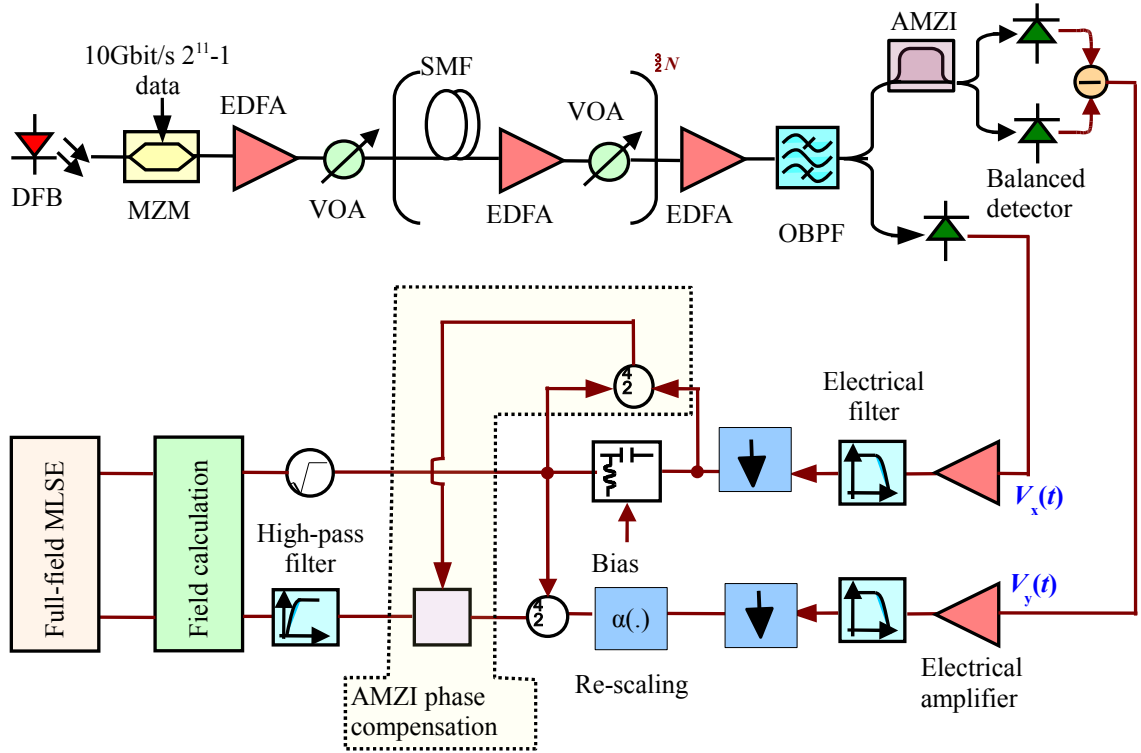
Figure 107: Simulation model in MATLAB

The signal was launched into an erbium-doped fiber amplifier (EDFA) amplified

transmission link with 80 km SMF per span and 0 dBm signal launch power. The

SMF was assumed to have CD of 16 ps/km/nm, a nonlinear coefficient of 1.2

/km/W, and a fiber loss of 0.2 dB/km. Split-step Fourier method was used to

calculate the signal propagation in the fibers. At the end of each span, amplified

spontaneous emission (ASE) noise from optical amplifiers was modelled as complex

additive white Gaussian noise with zero mean and a power spectral density of

$n_{sp}h$ (G-1) for each polarisation, where G and h are the amplifier gain and the

photon energy respectively. n_{sp} is a population inversion factor of the amplifiers and

was set to give 4 dB noise figure (NF).

The noise of the optical preamplifier was also modelled as additive white

Gaussian noise with random polarisation. The launch power into the preamplifier

was adjusted to control the OSNR while the output power was set to be 0 dBm,

unless otherwise specified. The pre-amplified signal was filtered by an 8.5 GHz Gaussian-shaped optical band pass filter (OBPF) which suppressed the optical noise and CD to a certain extent. The signal after the OBPF was then split into two paths to extract $V_x(t)$ and $V_y(t)$, as shown in Figure 107. The AMZI for the extraction of $V_y(t)$ had $\sqrt{2}$ differential phase shift and DTD of 30 ps or 10 ps. The responsivities of the balanced detector and the single photodetector were assumed to be 0.6 A/W and 0.9 A/W respectively, and equivalent thermal noise spectral power densities were assumed to be 100 pA/Hz$^{1/2}$ and 18 pA/Hz$^{1/2}$ respectively. After detection, the signals were electrically amplified, filtered by 15 GHz 4th-order Bessel electrical filters (EFs), and down-sampled to 50 Gsamples/s (5 samples per bit at 10Gbit/s) to simulate the sampling effect of the real-time oscilloscope. The down-sampled copy of $V_x(t)$ was re-biased, which can significantly enhance the robustness of the scheme to thermal noise. To allow for path length variations due to manufacturing tolerance, temperature variations and device aging, a sample shifting was included to provide delay tunability with a resolution equivalent to the sampling interval (20 ps), and the amplitude was adjusted to correct for any gain imbalance of the $V_x(t)$ and $V_y(t)$ paths. Additional signal processing stages included a phase compensator to enhance the tolerance of differential phase misalignment of AMZI and a Gaussian-shaped high-pass electrical filter to suppress the impairment from low-frequency amplification. Full-field MLSE module operates with two samples per bit, 5-bit ADC resolution, and memory length m of 2 and 4 (corresponding to the state number of 4 and 16 respectively).

The simulation was iterated ten times with different random number seeds to give a total of 184,230 simulated bits. The performance was evaluated in terms of the

required optical signal-to-noise ratio (OSNR) to achieve a bit error rate (BER) of $5*10^{-4}$ by direct error counting. 184,230 bits were sufficient to produce a confidence interval of $[3.5*10^{-4}\ 7*10^{-4}]$ for this BER with 99% certainty.
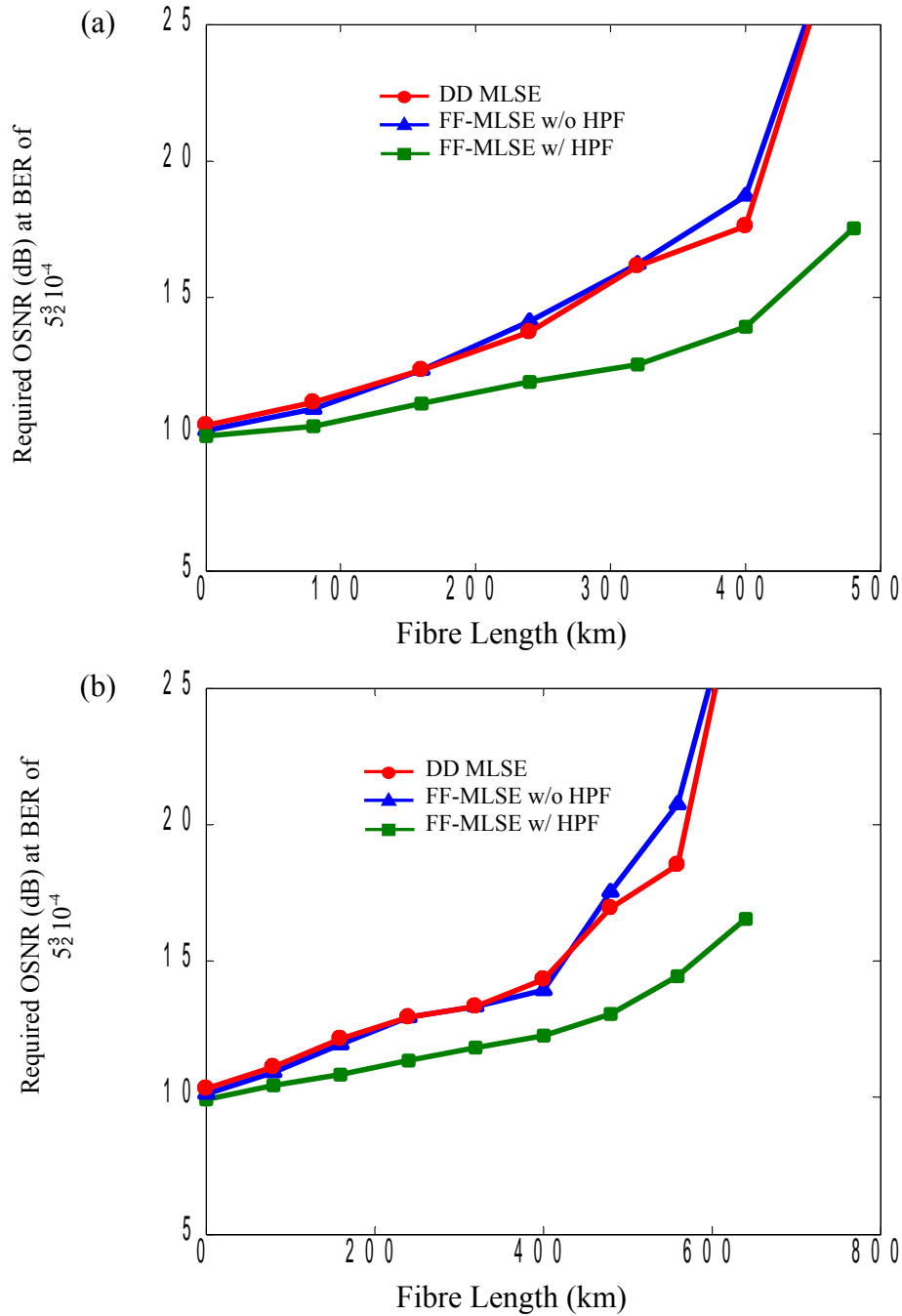
Figure 108: Required OSNR versus transmission reach when the MLSE memory is (a) 2 and (b) 4

Figure 108 shows the required OSNR versus fibre length by using conventional direct-detection MLSE (circles), full-field MLSE without high-pass filter (triangles), and with a 0.85 GHz high-pass filter for suppressing low-frequency amplification mechanism (squares). From the Figures, it is found that the full-field MLSE without proper suppression of low-frequency amplification shows slightly poorer compensation performance compared to conventional DD MLSE regardless of the memory length m. By optimizing the low-frequency response for the estimated frequency $V_f(t)$ (squares), phase estimation is significantly improved. As a result, full-field MLSE can greatly outperform DD MLSE, as verified for both 4 and 16 states. At OSNR of 15 dB (~ 5 dB penalty with respect to back-to-back sensitivity), the CD tolerance was enhanced from 270 km to 420 km, and from 400 km to 580 km for m of 2 and 4 respectively, representing approximately 50% performance improvement.

In electronic signal processing, ADC resolution is always an essential issue to balance the performance and electronic computation complexity. $2^{\text{Quantisation Level}}$ is the number of levels available to approximate the analogue signal in the digital domain. Figure 109 depicts the performance as a function of quantisation resolution, and it is clear from the figure that 5-bit resolution used in the simulation resulted in less than 1dB penalty compared to the 7-bit reference. This is achievable using modern microelectronic technologies and the state-of-art ADCs can have a resolution of 6-8 bit at 30~56 Gsamples/s, with extendibility to higher sampling rate in interleaving mode.
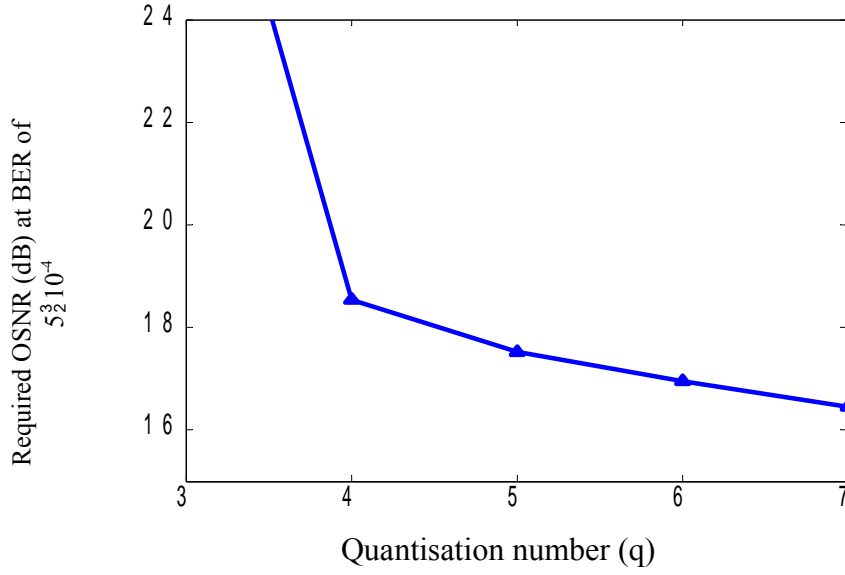
Figure 109: Required OSNR versus the ADC quantization resolution at 480km using 4-state full-field MLSE.

6.5 Experimental FF-MLSE

The experimental set-up was described in section 5.13 . The FD-MLSE inputs were re-sampled to two samples per bit and A/D converted with 5-bit resolution. The MLSE algorithm has four states. The high-pass filter (HPF) in FD-MLSE has a 3dB cut-off frequency of 0.42GHz. The DD-MLSE uses $V_y(t)$ only. The DD-MLSE uses the output of the amplitude detector only. Figure 110 depicts $\log_{10}$(BER) versus OSNR following transmission over (a) 248 km and (b) 372 km of field-installed SMF. It can be seen from the figure that by using conventional DD 4-state MLSE, the required OSNR to achieve the FEC limit for 248 km is 25.5 dB while 372 km transmission is unachievable. FD-MLSE without the high-pass filter exhibits worse performance compared to DD-MLSE due to impairments from low-frequency component amplification. By using FD-MLSE with a high-pass filter, however, a significant performance improvement is obtained. In Figure 110(b), it is observed

that FD-MLSE should enable a BER of $3.5*10^{-4}$ for 372 km SSMF transmission at an OSNR of 25.4 dB, representing a 50% increase in transmission reach over DD-MLSE. It should be noted that in this experiment some parameters, e.g. bias of $V_x(t)$, scaling of $V_y(t)$, etc., are not optimised. Furthermore, due to relatively high thermal noise of the balanced detector and the limited amplifier gain, the receiver was also degraded by thermal noise.
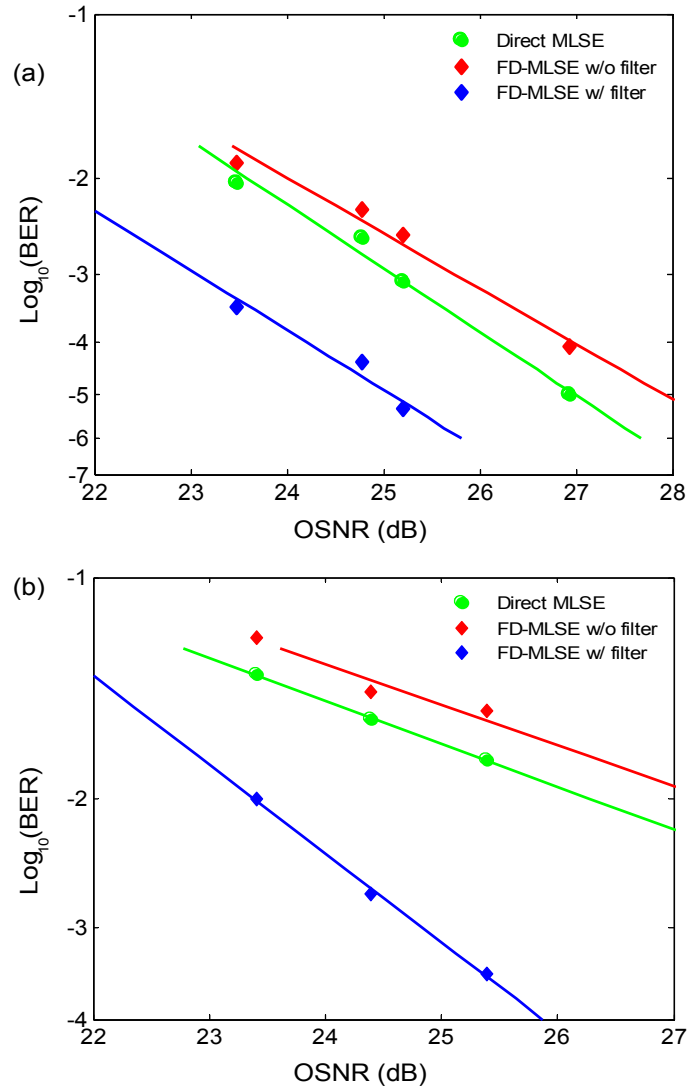
Figure 110: BER vs OSNR comparing MLSE implementations (a) 242km and (b) 372km

The evolution of the probability of '010' with transmission distance is shown in Figure 111. This shows the probability of this sequence having been sent given the

sampled real and imaginary received bits. The plots show how the probability function changes from 0 km transmission to 500 km transmission. It can be observed that the shape is still reasonably Gaussian at this transmission distance. This indicates that the real and imaginary components of the received signal may not be strongly correlated at these distances and could be treated independently. This is illustrated in Figure 112.
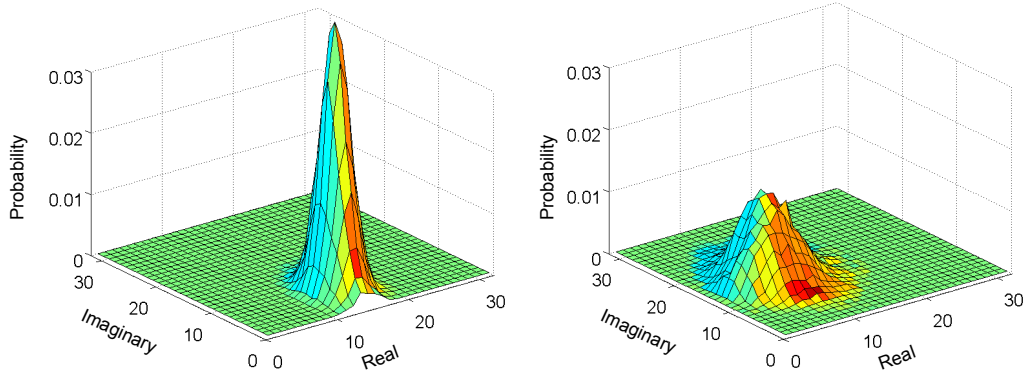
Figure 111: Evolution of Probability as transmission increases for '010' bit sequences and q=5

6.6 Simplified FD-MLSE [xv]

A FD-MLSE based system can achieve a 50% greater transmission reach than DD-MLSE at the expense of an increased lookup table size. This increased lookup table size increases the electronic complexity of the solution, requiring more memories as well as an associated increase in searching time and the time for lookup table set-up and update. This section proposes a novel metric for full-field MLSE with significantly reduced complexity while introducing negligible system penalties.

The recovered full-field information (phase and amplitude) was used to obtain the real and imaginary components of the optical field, which were synchronously re-sampled with two samples per bit and analogue-to-digital (ADC) converted with resolution of q bits. Full-field MLSE exploited the real and imaginary components

simultaneously in channel training and metric computation.

The required memory for $\ln p(\Re(v_k(t)), \Im(v_k(t))|I_{L-k}, ..., I_k)$ is proportional to 2^{2q+L+2} with two samples per bit, while the complexities of metric computation and Viterbi decoding were the same as those of a DD-MLSE with the same number of states. To reduce the required complexity for the lookup table, a novel metric is proposed:

$$PM_k(\boldsymbol{I_k}) = ...$$
$$\sum_i \ln p(\Re(v_k(t))|I_{L-k}, ..., I_k) \ln p(\Im(v_k(t))|I_{L-k}, ..., I_k) + PM_{k-1}(\boldsymbol{I_{k-1}}) \qquad (84)$$

under the assumption that the probability distributions for real and imaginary signals are independent. Compared to the original metric or combined metric (83), the independent metric (84) significantly reduces the required memory, and associated searching time, and time for initial lookup table set-up and update from 2^{2q+4} to 2^{q+5} at 4 states. It might be anticipated that this assumption is valid because the noise on the real and imaginary parts are only slightly correlated, and there is little apparent correlation in the joint probability distribution.
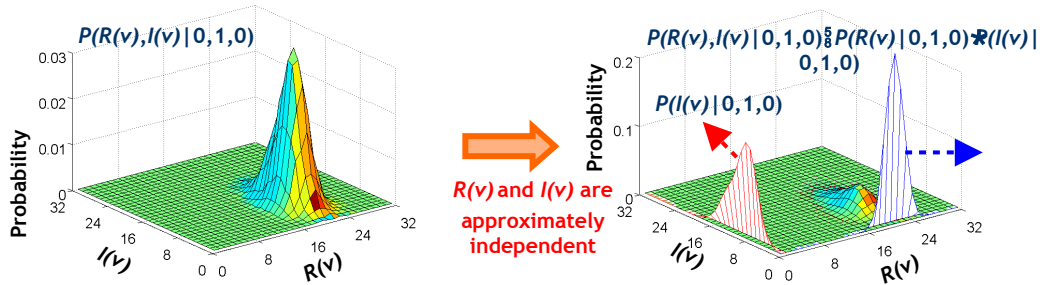
Figure 112: (a) is joint metric 0 km transmission and (b) shows joint metric after 480km and superimposed independent metrics

Figure 113 depicts $\log_{10}(BER)$ versus OSNR following transmission over 372 km of field-installed SMF. It can be seen from the figure that by using conventional 4-state DD MLSE, 372 km transmission is unachievable. In contrast, full-field MLSE

exhibits a significant performance improvement compared to DD-MLSE, with a BER of $2.8*10^{-4}$ and $3.2*10^{-4}$ for 372 km SMF transmission at an OSNR of 26dB for metric combined and independent respectively. The comparison between circles and triangles in Figure 113 shows that combined metric exhibits negligible performance degradation although it significantly reduces the size of lookup table from 2^{2q+4} to 2^{q+5}. It should be noted that the component parameters have not been optimized in this experiment and the system may be degraded by thermal noise of the receiver and digital oscilloscope.

Whilst the use of a high-pass filter to suppress low-frequency component amplification is essential to improve the quality of phase estimation, it also introduces distortion to $V_f(t)$. This distortion has the potential to restrict the ability to reconstruct the optical field. However, full-field MLSE was found to be robust to such signal distortion. The variation in BER at 26 dB OSNR as a function of the filter bandwidth is illustrated in Figure 114. It is observed that when the low-frequency component amplification is suppressed (above 0.5 GHz bandwidth), the newly proposed independent metric and the combined metric perform equally well (BER<10^{-3}). However, when the system is dominated by low-frequency component amplification, a correlation in the noise statistics of the real and imaginary components may be expected, breaking the assumption leading to the independent metric, and the performance is degraded more severely.
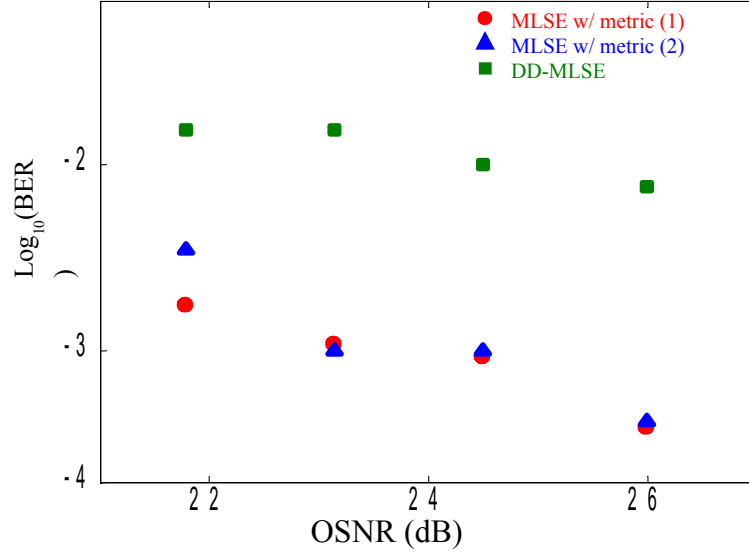
Figure 113: log10(BER) versus OSNR for 272km transmission using 4-state MLSE

Finally, the benefits of the proposed technique are shown in Figures 115 and 116 which illustrate $\log_{10}$(BER) versus complexity of lookup table, and length of training sequence after 372 km SMF at 26 dB OSNR respectively. It can be observed from the figures that BER is greatly reduced as the complexity or the length of training sequence increases, and full-field MLSE exhibits much better maximum achievable performance than DD MLSE. The minimum required memory and training sequence length for the proposed independent to achieve FEC limit (BER of $1*10^{-3}$) are around one order less than that using the original combined metric, confirming the benefit of the proposed method.

6.7 FF-EDC with Extended State Number

A 16-state MLSE chip is commercially available [63]. It shows a theoretical reach of 5000 ps/nm of dispersion compensation for 15dB OSNR which approximates to 315.5 km using our assumption of dispersion (16 ps/nm/km). Section 6.4 shows a theoretical reach of 580km for the same OSNR using a 16 state MLSE with access to the full field. It should be noted that the [63] uses a 3-bit resolution and this work

assume 5. Figure 117 presents the off-line processed experimental results for 496 km using a 16 state MLSE. It plots the results for both the full combined metric and for the simplified independent metric and show that the FEC limit can be reached with a reasonable margin for both.
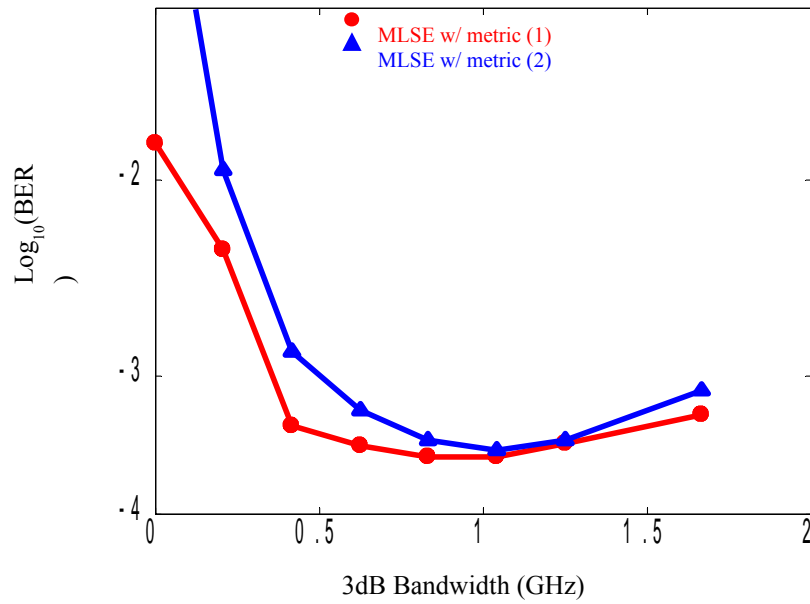
Figure 114: log₁₀(BER) versus bandwidth of high-pass filter
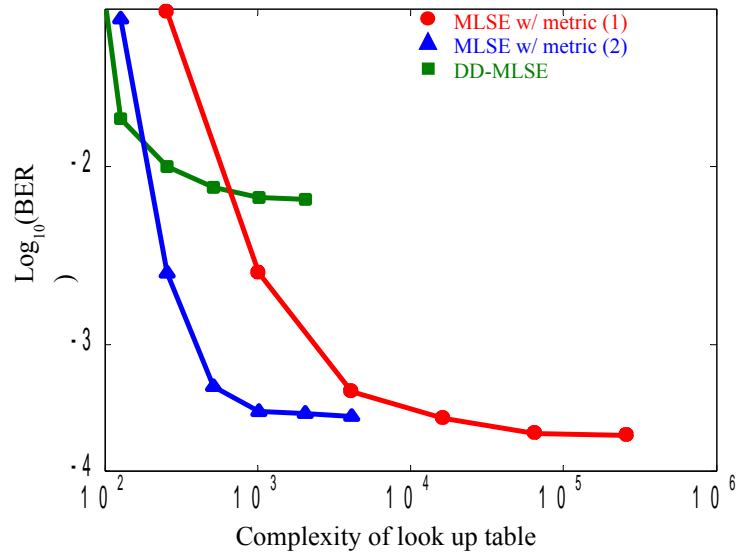
Figure 115:Performance as a function of complexity of lookup table (required memory and an associated searching time) after 372km transmission at 26dB OSNR length of training sequence is 500,000 bits;3dB bandwidth of high-pass filter is 1GHz.
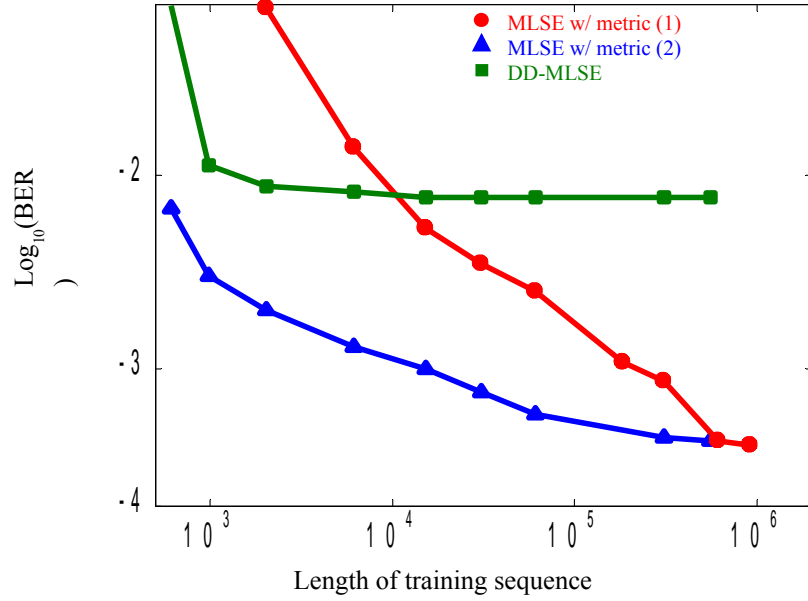
Figure 116: Performance as a function of length of training sequence after 372km transmission at 26dB OSNR; quantization resolution is 5 bits;3dB bandwidth of high-pass filter is 1GHz.
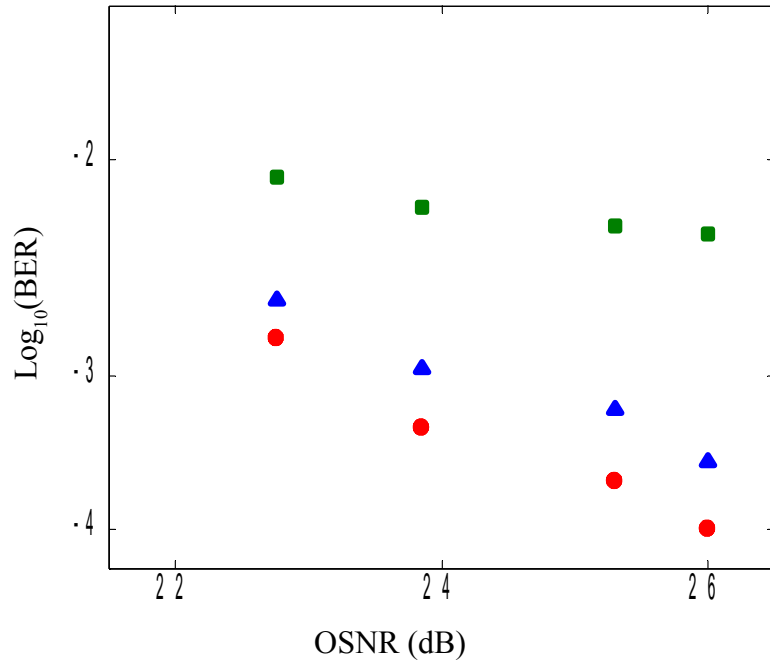
Figure 117: Performance versus received OSNR for 496 km using 16-state MLSE. Squares, triangles and circles represent DD MLSE(green), full-field MLSE based on independent metric (blue) and combined metric (red) respectively. High-pass filter bandwidth was optimized.

Figure 118 shows the achievable BER using off-line processing for various distances

174

presented in this chapter for 4- and 16-state MLSE using the combined metric. The 4- state MLSE is used for distances less than 400 km and 16 state for 480 km reach.
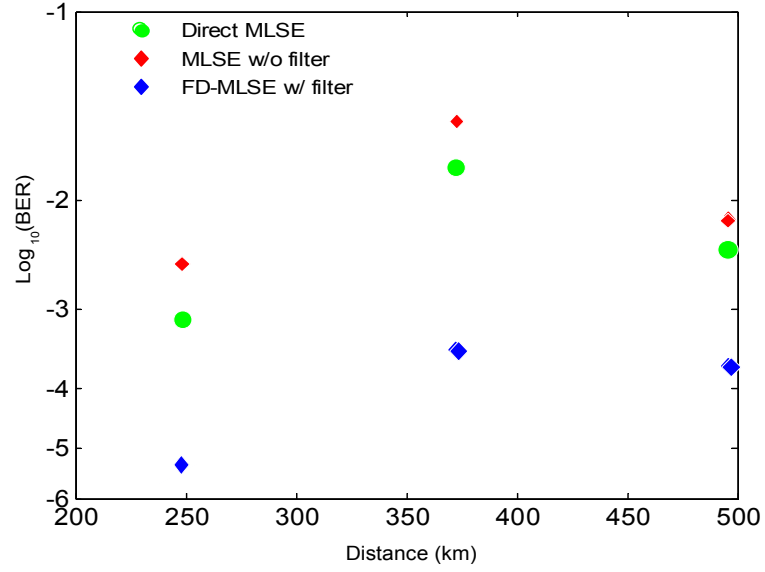
Figure 118: BER at 25dB OSNR for experimental distances 4state MLSE (full line) and 16 state MLSE (dashed line) for DD-MLSE and FD-MLSE with and with filter

6.8 Conclusion

This chapter introduces a novel MLSE metric calculation scheme which utilises the access to full field. This has given a 50% increase in transmission reach compared to direct detection MLSE. Then, by attempting to reduce the cost of larger high speed look up tables, but maintaining the same performance, it has been shown that by considering the real and imaginary parts of the field as being uncorrelated similar performance can be achieved. This reduces the amount of high speed memory significantly. This MLSE technique has been experimentally verified using the phase estimation technique but it could also be used with coherent detection as this also allows for access to the full received optical field.

7 Future Work and Discussions

7.1 Introduction

This chapter will summarize the technical achievements of this thesis. It will compare the two DSP methods presented and gives a summary of their strong and weak points. It will mention on-going patents and invention disclosures whose work has not been included in this thesis as their publication date is pending. A comparison will be drawn between the full-field receiver and digital coherent detection with a view to describing the advantages and disadvantages for various applications.

7.2 Summary of Technical Findings and Contributions

The interest in simple optics and cheap electronics has led to development of signal processing in the electrical domain. Previous and in parallel with this thesis work, FEC and E-FEC have become standard, effective and trusted technologies (Section 1.3). This has opened the door to the possibility of applying other post-processing techniques to combat dispersion effects. The performance enhancement that can be achieved using only the information from the received amplitude has led to interest in what could be achieved if the entire optical field could be down-converted into electrical domain cost effectively. This allows for access to whole area of RF approaches to combat transmission impairments and introduce advanced modulation techniques.

This thesis has investigated a novel receiver structure, the phase estimation receiver, which enables access to the full optical field, for use specifically in this work for

electronic dispersion compensation but can be extended to any detection which requires access to the phase and amplitude information. This section will review and emphasis the technical findings of this work.

1. It was shown in theory and in preliminary simulations that by using a frequency sensitivity filter, the instantaneous frequency of the incoming optical signal can be estimated in the electrical domain. An example of a frequency sensitive filter is an Asymmetric Mach-Zehnder Interferometer biased at quadrature. Combining this with standard amplitude detection or using the sum of the outputs of the AMZI, the optical field can be reconstructed in the optical domain.

2. This practical ability of the receiver to reconstruct the phase of an incident signal was demonstrated. An opto-electric DPSK wavelength converter was reported with a 1.8 dB penalty using phase estimation and modulation of a NEL laser in Chapter 4

3. It has been shown that this receiver structure can be used for Mid span spectral inversion (MSSI). Theoretical and simulation results are presented in Chapter 2 and 240 km transmission was reported using 120km of field installed fibre in Chapter 4.

4. The effect of low frequency amplification in phase estimation path is shown to be a critical factor in the effectiveness of the field reconstruction and the subsequent dispersion compensation in Chapter 5. This is also illustrated experimentally. The use of an electrical high pass filter and relatively low optical extinction ratio is shown to combat this effect. The theoretical reach is extended to 2000 km using this adaptation.

177

5. The receiver is thoroughly characterised using MATLAB simulation in the presence of fibre non-linearity, thermal noise, filter misalignment, sampling misalignment, sampling rate, OBPF bandwidth and AMZI length. It has been shown -3dB is the optimum launch power; a V_{bias} in the amplitude path combats thermal noise; ∓10 degree misalignment is tolerable in AMZI for 1dB penalty; a 20ps window for the same penalty for sample misalignment; 2 Gsamples/sec has a 2 dB penalty compared to 5 Gsamples/s and above this the benefit is negligible; OBPF less than the ITU grid offers significant improvement and this narrows with distance with a 0.1 nm filter being optimum for 600 km transmission; an AMZI delay has an optimum between 25-50 ps.

6. The first transmission beyond the dispersion limit using FF-EDC which utilises the phase estimation receiver and off-line dispersion compensation to 248 km is demonstrated.

7. The condition for failure of all receiver side based dispersion compensation in recovering an isolated '1' bit preceded and followed by a number of '0's is illustrated. An adaptive threshold decoding is proposed. Alternatively ,a statistical investigation of the susceptible patterns is presented. This could be used to develop a line code which would be improve the performance of receiver-side EDC

8. Transmission reach up to 496 km over 4 loops of 120km field installed fibre was demonstrated using a 0.3 nm filter, 6 dB extinction ratio and 85 GHz spectral range AMZI with a 0.8 dB margin to the FEC limit at 20.84 dB OSNR . This is consistent with MATLAB and VPI simulations for the

same transmission conditions.

9. Maximum Likelihood Sequence Estimation with Multi-input-Single-Output structure is presented in Chapter 6 to utilise the real and imaginary information of the received optical field. It is shown in simulation that a 4-state FD-MLSE has a reach of 420 km for a back-to-back penalty of 5 dB and 16 states has a reach of 580 km. This offers a 50% improvement in transmission reach compared to conventional MLSE. An off-line experiment reach is shown of 372 km for 4-state FD-MLSE and 496 km reach for 16-states.

10. A simplified FD-MLSE metric is presented, based on the observed noncorrelated nature of the real and imaginary field components for distances suitable for MANs. This results in a negligible loss of performance compared to point (9) but requires merely twice the high-speed memory compared to DD-MLSE.

7.3 Frequency Domain Compensation and MLSE

This thesis has presented two digital signal processing methods to act as the dispersion compensation when implementing the proposed phase estimation receiver where the DSP to have access to the full down converted electrical field. This section will compare the two methods.

The frequency domain or transmission line compensation is the more theoretically obvious way to compensate for dispersion compensation as it implements the transfer function of the fibre and takes advantage of the fact, that by having access to the entire field, chromatic dispersion can be compensated as a linear impairment. It

would require the implementation of Fast-Fourier transform (FFT) and inverse transform (IFFT) but with the widespread interest in OFDM, this is a subject of widespread research. This work present results with 50 Gsamples/sec and have shown that reducing this to 20 Gsamples/sec gives a 2 dB penalty (Section 5.10). The results with respect to distance are shown in Figure 119 (blue). This required OSNR remains constant which is consistent with Section 5.4 and as shown In section 5.18 for the configuration, this is approximately the predicted required OSNR. This technique requires the optimisation of 3 off-line parameters.
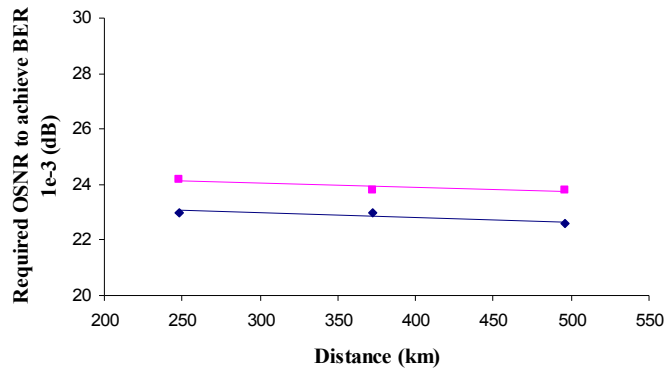
Figure 119: Required OSNR vs Distance for FF-EDC(blue) and FD-MLSE (pink)

The other DSP dispersion compensation that is presented in this thesis is Maximum likelihood sequence estimation which utilises the full detection optical field. The MSLE uses 2 samples/bit and 5-bit resolution. This is restricted compared to the FF-EDC as increasing these numbers results in exponential increase in the size of the high speed memory that is required. A commercially available product has implemented both 4 and 16 state MLSE. Using this as bench mark for achievable ASIC capabilities, it should be possible to achieve 372 km and 496 km transmission using 4 and 16 states respectively. Two possible metrics have been presented for implementing FD-MLSE, one of which requires square as much high speed memory

180

as the equivalent DD-MLSE but with 50% increase in reach. A method has also been presented which requires only twice as much memory but provides the same improvement in performance. This should be a realisable implementation using currently available technologies. Figure 119 shows the required OSNR vs distance and see that it has approximately 1 dB penalty across the range considered in this thesis. It has shown that the achievable distance for FD-MLSE even with extended AMZI for 16 states is 580 km for 5 dB penalty 0 km transmission and 80 km spans. The FF-EDC has been shown to able to achieve much longer transmission distances if AMZI and filter bandwidths are optimised. However in terms of the application area of interest for this thesis, metropolitan area networks, FD-MLSE as a more mature technology and, having been shown to achieve suitable reach, may be of more immediate interest.

7.4 Comparison of Electronic Dispersion Compensation Methods

Digital pre-distortion of the signal for dispersion compensation as described in section 1.6.2 was first suggested in 2004 [13] and demonstrated using DAC generated from individual components and FPGA processing [64,129-130] and a commercial product was demonstrated [16,65] with reaches up 3840 km. This is shown in pink in Figure 120. This technique provides outstanding performance and has been shown to be sufficiently robust to be generated using an FPGA and individual components in the laboratory. It is a commercially available but it has a number of draw backs which make its less suitable for metropolitan networks. It requires that information about the link be available at the transmitter to allow the

correct transmitted signal to be generated. The signal is also only available at a limited window about the target distance (this is indicated by the dashed nature of the "visibility" arrow). This is undesirable in MANs were multi-broadcast signal may be being used and switching of transmission paths may occur frequently.

At the time of writing, digital coherent detection products are available in the market. Real time measurements are presented in [62] and have achieved experimental reaches of 6400 km using offline processing. This is shown in yellow in Figure 120. This provides excellent reach and sensitivity. There has been significant research effort into this receiver type in the last number of years [62,68,88-96,132-133] and it shows great promise for detecting multilevel formats and Optical Frequency Division Modulation (OFDM). This receiver requires a local laser, an optical hybrid, 4 detectors and a large DSP effort. While this will be certainly the technology of choice for long haul networks for shorter reaches, the simplicity of the direct detection or full-field detection using only one extra optical element may be a more cost effective solution.

MLSE has been used in wireless and RF communications extensively. It was introduced as a possible solution for dispersion compensation for optical fibres in 2004/5 [134-136] and an integrated solution was presented the following year [137]. Theoretical results for many thousands of states were shown to have a limit reach of 700 km with a 3 dB penalty [74]. In practice the number of states which can be realised in limited to 16 [63] and this has a reach of 315 km. Using a square root metric estimation, this can be extended to 550 km and 64 states [138] - this will not be physically realisable in the near future but has been included as the most likely experimental reach in the near to medium term.

FIR and IIR filters [139] can be used for dispersion compensation in conjugation with direct detection but while they offer an improvement in reach, it is insufficient for MAN networks and will not be included here. They can and are used in combination with pre-distortion, coherent detection and could also be used with full-field detection. In fact, [62] uses an FIR filter as the dispersion compensation method.

The visibility or reach of the proposed receiver is shown in green. This shows that it has a reach which exceeds amplitude only MLSE but has shorter reach compared with coherent detection. FF-EDC offers a reach which is greater than MLSE using amplitude alone. FF-EDC offers an optically simpler approach than coherent detection. The cost of the increased digital processing to generate the real and imaginary parts should be significantly less than those required for coherent detection. Thus FF-EDC is particularly suited to applications which are cost sensitive and require a reach of 500 km-700 km reach.
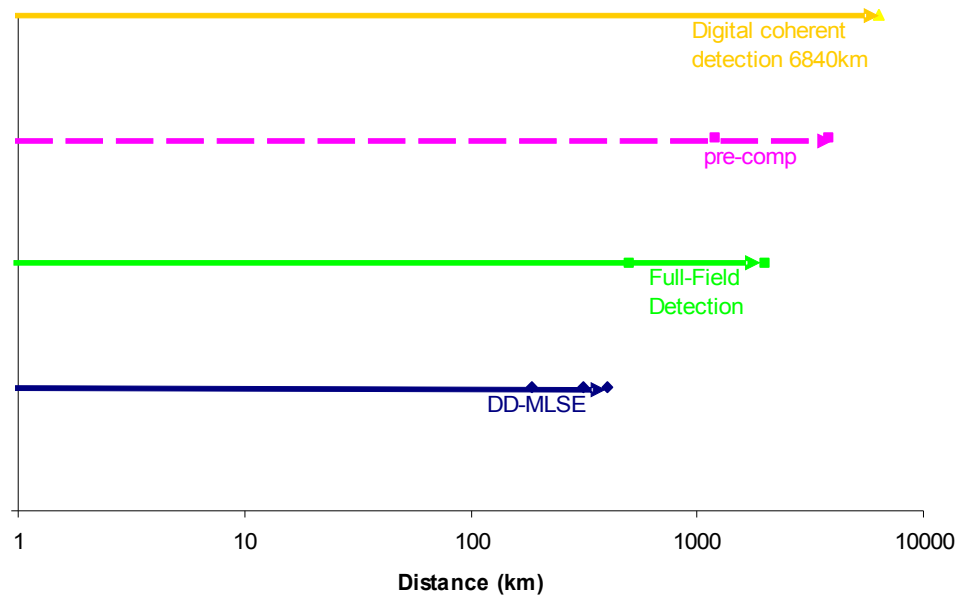
Figure 120: Schematic Comparison of the visibility of Electronic Dispersion methods where visibility is the reach where a receive node can be placed without adjustment of the transmitted signal

7.5 Future Work and Plans

This section considers some of the areas of future work which could be carried out in relation to full-field detection and digital signal processing

7.5.1 Real Time Demonstration

In order to confirm the findings of the theoretical examination and off-line processing, to confidently detect lower error rates and consider longer PRBS sequence, and to tweak the system to its optimum performance, a real time demonstrate must be developed. This would consist of two time aligned ADC chips which in the last twelve months have begun to become commercially available and state of the art FPGA from Xilinx or Alterra which have many high-speed inputs. This is a very challenging project as demonstrated by the accreditation of 107

184

engineers in one of the reported real-time demonstration of a similar approach [62].

The implementation of a demonstrator would allow for real-time monitoring and correction of many parameters considered in this thesis as possible sources of error in this technique (bias at quadrature of AMZI, time alignment of samples, sampling phase) and allow for algorithms to be developed and tested to optimise these. This should allow for improvement in performance and speed up the investigation of this approach.

7.5.2   Other Modulation Formats and Transmission Impairments

Only chromatic dispersion compensation of non-return to zero signal was considered in this thesis. This allowed for a standard simple receiver to be used and MAN-type reach to be achieved. There are many other modulation formats and transmission impairments that can be considered depending on the reach and line rate that is required, that having access to the phase and amplitude of the signal would allow for easy detection and reconstruction. Two areas of interest would be the use of full-field detection for use with OFDM signals which would allow for this technology to be employed in lower cost networks. Another is the compensation of non-linear impairment which while MLSE allows for compensation of a certain amount due to its statistical nature, when distance and power are increased, these will become more and more significant.

7.5.3   Evolution of the Phase-Estimation Receiver [vii]

A European patent has been filed this year with regard to extension of this work (EP09163524.3) which will consider the use of multi-step transmission

compensation using phase estimation receiver. This should lead to some very interesting findings and broaden the network types that the phase estimation receiver can be considered for use. The patent is particular to utilising full-field reconstruction a slowly adapting or fixed dispersion compensation mechanism followed by a fast adapting section all of which utilise phase and amplitude or real and imaginary processing.

7.6 Conclusion

The primary conclusion of this thesis is that the phase estimation or full-field receiver is a viable method of converting the phase and amplitude of the received optical signal into the electrical domain. It can be combined with conventional electronic dispersion compensation methods to achieve metropolitan type reaches cost effectively.

The development of electronic dispersion compensation in recent times has been fuelled by previous delay in deploying 40 Gbit/s networks, which has allowed for Analogue-Digital and Digital-Analogue Converter technologies to catch up with the 10GHz installed networks [59-61]. This has opened the door to utilising digital signal processing to compensate for transmission impairments. Much interest has been placed in using square law detection in conjunction with EDC techniques such as FIR, IIR and MLSE. These have a fundamental limitation in that the phase information of the signal is lost. This limits the amount of transmission compensation which can be achieved. The obvious next step in the development of EDC is to gain access to the phase information as well. The novel receiver structure in this thesis allows for this without the complexity of coherent detection. This specifically lends

this technology towards metropolitan area networks, where square-law detection schemes have insufficient reach and coherent detection is too costly and complex. It has been demonstrated that this design can achieve 496 km reach using off-line processing and FF-MLSE in installed fibre using high loss long spans. This shows that it is practical for either cabinet skipping or for challenging metropolitan networks. This confirms the potential of FD-EDC as a possibility for MANs.

In summary, FD-EDC has shown itself to be an appropriate technology for employment in MAN networks which require dispersion compensation. It has show the possibility of extended reach using optimised parameters to be able to detect the full field and utilise digital signal processing far beyond this up to 2000 km. Using a FF-MLSE which uses information from the real and imaginary fields, the reach of 4-state MLSE has been extended to 450 km (372 km experimentally) using 2 samples/bit which is a 50% increase in reach for the same number of states compared to using amplitude alone. In short, a phase-estimation receiver has been demonstrated as an enabling technology for digital signal processing and as a competent alternative to coherent detection.

A   Technical Acknowledgements

The topic of this work was a work package within the group's research activity. Consequently the work presented in this thesis is the result of collaboration. The original concept was presented by Dr. Andrew D. Ellis who supervised all of this work. The development of the FF-MLSE is a collaboration led by Dr. Jian Zhao who joined the project half-way through this thesis. Certain sections have direct contribution specifically:

- Andrew D. Ellis

    - 3.4 Simple Description of Theory;

    - 3.5.1-2 System Simulations

- Jian Zhao -

    - 5.4 Suppression of Low-Frequency Component Amplification;

    - 6.4.1 Full Field MLSE

B　　　Publications

B.1　　　Journal Publications

i　M. McCarthy and A. Ellis,"Electronic Dispersion Compensation Utilising Full Optical Field Estimation" *Mediterranean Journal of Electronics and Communications*, vol 3, no 4, 2007, pp144-151

ii　M. McCarthy and A. Ellis,"Wavelength conversion for 10.7 Gbit/s DPSK without differential decoding," *Electronics Letters*, vol. 43, 2007, p. 993–994.

iii　J. Zhao, M.E. McCarthy, and A.D. Ellis, "Electronic dispersion compensation using full optical-field reconstruction in 10Gbit/s OOK based systems," *Optics Express*, vol. 16, 2008, p. 15353-15365.

iv　J. Zhao, M. McCarthy, P. Gunning, and A. Ellis, "Mitigation of Pattern Sensitivity in Full-Field Electronic Dispersion Compensation," *Photonics Technology Letters,* IEEE, vol. 21, 2009, p. 48–50

v　M. McCarthy, J. Zhao,P. Gunning, and A. Ellis,"Full-Field Electronic Dispersion Compensation of a 10Gbit/s OOK Signal over 4x124km Field-Installed Single-Mode Fibre ", *Journal of Lightwave Technologies, ,* 2009 *(May 2009)*

B.2　　　Patents and Invention Disclosures

vi　A. Ellis and M. McCarthy/University College Cork-National University of

189

Ireland, Cork [EI/IE], "Dispersion Compensation", World Patent WO 2006/131904, June 8,2006

vii   J. Zhao and M. McCarthy/University College Cork-National University of Ireland, Cork [EI/IE],"Hybrid Full-Field Electronic Dispersion Compensation" European Patent EP09163524.3, June 22, 2009

B.3   Conference Presentations

viii   M. McCarthy and A. Ellis, "Low-cost receiver side electronic dispersion compensation of the full optical field," *Optical Fibre Communications and Electronic Signal Processing, 2005. The IEE Seminar on (Ref. No. 2005-11310)*, 2005, p. 0_16-3/6.

ix M.E. McCarthy, A.D. Ellis,"Electronic Dispersion Compensation Utilising Full Optical Field Estimation", *Communication Systems, Networks and Digital Signal Processing 2006,CSNDSP 2006, Fifth International Symposium on,* P199, ISBN 960-89282-0-6, p 679-692

x Andrew D. Ellis and Mary E. McCarthy, "Receiver-Side Electronic Dispersion Compensation Using Passive Optical Field Detection for Low Cost 10Gbit/s 600 km-Reach Applications," *Optical Fiber Communication Conference and Exposition and The National Fiber Optic Engineers Conference, Optical Society of America, OFC* 2006, OTuE4

xi M.E. McCarthy, A.D. Ellis,"Electronic Dispersion Compensation Utilising Full Optical Field Estimation" 2007, *Photonics Ireland* 2007

xii   J. Zhao, M. McCarthy, P. Gunning, and A. Ellis, "Dispersion

Tolerance Enhancement in Electronic Dispersion Compensation using Full Optical-Field Reconstruction," *Optical Fiber communication/National Fiber Optic Engineers Conference,* 2008. OFC/NFOEC 2008. Conference on, 2008

xiii   M. McCarthy, J. Zhao, A. Ellis, and P. Gunning, "Full field receiver side processing for electronic dispersion compensation," *IEEE/LEOS Summer Topical Meetings,* 2008 Digest of the, 2008, p. 171–172.

xiv   M. McCarthy, J. Zhao, P. Gunning, and A. Ellis, "A novel field-detection maximum-likelihood sequence estimation for chromatic-dispersion compensation," *Optical Communication, 2008. ECOC 2008. 34th European Conference on,* 2008,

xv   J. Zhao, M.E. McCarthy, P. Gunning, and A.D. Ellis, "Chromatic Dispersion Compensation Using Full Optical-Field Maximum Likelihood Sequence Estimation," *Optical Fiber Communication , 2009. OFC 2009. Conference on,*2009, OthE6

.

B.4   Other Publications

xvi   Cuenot, B.; Gunning, F.C.G.; McCarthy, M.; Healy, T.; Ellis, A.D.;"Transmission Impairments for 298.2Gbit/s Coherent WDM over 600km of Standard Single Mode Fibre", *Lasers and Electro-Optics, 2007 and the International Quantum Electronics Conference. CLEOE-IQEC 2007. European Conference on,* 2007

C   References

[1]   F.P. Kapron and D.B. Keck, "Pulse Transmission Through a Dielectric Optical Waveguide," *Applied Optics*, vol. 10, 1971, p. 1519-1523.

[2]   K. Kao and G. Hockham, "Dielectric-fibre surface waveguides for optical frequencies,"*Journal of Optoelectronics*, vol. 133, 2008, p. 191-198.

[3]   T.H. Maiman, "Stimulated Optical Radiation in Ruby," *Nature*, vol. 187, 1960, p. 493-494.

[4]   D. Gloge and T. Li, "Multimode-fiber technology for digital transmission," *Proceedings of the IEEE*, vol. 68, 2005, p. 1269-1275.

[5]   J. Yamada, et al., "2 Gbit/s optical transmission experiments at 1.3 um with 44 km single-mode fibre," *Electronics Letters*, vol. 17, 1981, p. 479-480.

[6]   R.A. Linke and A. Gnauck, "High-capacity coherent lightwave systems," *Journal of Lightwave Technology*, vol. 6, 1988, p. 1750-1769.

[7]   E. Desurvire, "Erbium-doped fiber amplifiers : device and system developments", *J. Wiley & Sons*, 2002.

[8]   S. Bergano, "Wavelength division multiplexing in long-haul transmission systems," *Journal of Lightwave Technology*, 1996, p. 1996.

[9]   R. Stolen, "Fiber Raman lasers," *Fiber and Integrated Optics*, vol. 3, 1980, p. 21-51.

[10]   J. Winters and R. Gitlin, "Electrical signal processing techniques in long-haul fiber-optic systems," *IEEE Transactions on Communications,* vol. 38, 1990, p. 1439–1453.

[11]   H. Bulow and G. Thielecke, "Electronic PMD mitigation-from linear equalization to maximum-likelihood detection," *Optical Fiber Communication Conference,. OFC 2001*, 2001, vol 3, WAA3

[12]   H. Bulow, "PMD mitigation by optic and electronic signal processing," *Lasers and Electro-Optics Society, 2001. LEOS 2001,* 2001, vol 2, p. 602–603

[13]   R. Killey, et al. "Electronic dispersion compensation by signal predistortion

using a dual-drive Mach-Zehnder modulator," *Optical Fiber Communication Conference,. OFC 2005,* 2005, Vol. 4.

[14] M. McCarthy and A. Ellis, "Low-cost receiver side electronic dispersion compensation of the full optical field," *Optical Fibre Communications and Electronic Signal Processing, 2005. The IEE Seminar on*, 2005

[15] D. McGhan et al. "5120 km RZ-DPSK transmission over G652 fiber at 10 Gb/s with no optical dispersion compensation," *Optical Fiber Communication Conference, OFC 2005* , Vol. 5, 2005.

[16] J. McNicol et al "Electrical domain compensation of optical dispersion" *Optical Fiber Communication Conference, OFC 2005*, Vol. 4., 2005

[17] T. Nielsen and S. Chandrasekhar, "OFC 2004 Workshop on Optical and Electronic Mitigation of Impairments," *Journal of Lightwave Technology*, 2005, vol. 23, p. 131.

[18] R. Killey et al "Electronic dispersion compensation by signal predistortion using digital Processing and a dual-drive Mach-Zehnder Modulator," *Photonics Technology Letters, IEEE*, vol. 17, 2005, p. 714–716.

[19] P. Schvan, "A 24GS S 6b ADC in 90nm CMOS," *Digest of Technical Papers - IEEE International Solid-State Circuits Conference*, vol. 51, 2008, p. 544-545.

[20] J.P. Elbers et al. , "Measurement of the Dispersion Tolerance of Optical Duobinary with an MLSE-Receiver at 10.7 Gb/s,"*Optical Fiber Communication Conference,. OFC 2005*, 2005.

[21] T. Mizuochi et al. "Forward error correction based on block turbo code with 3-bit soft decision for 10-Gb/s optical communication systems," *IEEE Journal of selected topics in quantum electronics*, vol. 10, 2004, p. 376-386.

[22] H.D. Kidorf et al, "Forward error correction techniques in long-haul optical transmission systems," *Laser and Electro-Optics Society*, vol. 2, Nov. 2001, p. 477-478.

[23] C.E. Shannon, "A Mathematical Theory of Communication," *Bell Systems Technical Journal*, vol. 27,. 1984, p. 379 – 423.

[24] R. Hamming, "Error Detecting and Correcting Codes," *Bell Systems Technical Journal*, vol. 29, 1950, p. 147-160.

[25]   I. Reed and G. Solomon, "Polynomial Codes over Certain Finit Fields," *Society of Industrial and Applied Mathematics*, vol. 8, 1960, p. 300-304.

[26]   C. Berrou et al., "Near Shannon limit error-correcting coding and decoding," IEEE *International Conference on Communications,*1993 , pp1064-1071.

[27]   O.A. Sab and V. Lemaire, "Block turbo code performances for long-haul DWDM optical transmission systems," *Optical Fiber Communication Conference,. OFC 2000*, 2000, p. ThS5.

[28]   I. Djordjevic et al "Regular and irregular low-density parity check codes for ultra long haul high-speed optical communications: construction and performance analysis," *Optical Fiber Communication Conference,. OFC 2008,* p. WM4.

[29]   C. Lin et al. , "Optical-pulse equalization of low-dispersion transmission in single-mode fibers in the 1.3-1.7Mu m spectral region," *Optics Letters*, vol. 5, 1980, p. 476.

[30]   A. Antos and D. Smith, "Design and characterization of dispersion compensating fiber based on the LP01 mode," *Journal of Lightwave Technology*, vol. 12, 1994, p. 1739-1745.

[31]   M. Onishi, et al.,Y. Koyano, M. Shigematsu, H. Kanamori, and M. Nishimura, "Dispersion compensating fibre with a high figure of merit of 250 ps/nm/dB," *Electronics Letters*, vol. 30, 1994, p. 161-163.

[32]   M. Onishi, et al., "Third-order dispersion compensating fibres for non-zero dispersion shifted fibre links," *Electronics Letters*, vol. 32, 1996, p. 2344-2345.

[33]   L. Gruner-Nielsen, et al., "Dispersion-Compensating Fibers," *Journal of Lightwave Technology*, vol. 23, Nov. 2005, p. 3566.

[34]   M. Eguchi, et al., "Dispersion compensation based on dual-mode optical fiber with inhomogeneous profile core," *Journal of Lightwave Technology*, vol. 14, 1996, p. 2387–2394.

[35]   C. Poole, et al., "Helical-grating two-mode fiber spatial-mode coupler," *Journal of Lightwave Technology*, vol. 9, 1991, p. 598–604.

[36]   C. Poole et al., "Optical fiber-based dispersion compensation using higher order modes near cutoff," *Journal of Lightwave Technology*, vol. 12, 1994, p.

1746–1758.

[37]   P. Kirstensen, et al., "Dispersion and Slope Compensating Module for G.652 Fiber with x4 Reduced Physical Dimensions," *European Conference on Optical Communication, ECOC 2003,* 2003.

[38]   R. Kashyap, *Fiber bragg gratings*, San Diego Academic Press, 2004.

[39]   T. Stephens, et al., "257 km transmission at 10 Gbit/s in non-dispersion-shifted fibre using an unchirped fibre Bragg grating dispersion compensator," *Electronics Letters*, vol. 32, 1996, p. 1599–1601.

[40]   F. Ouellette, "Dispersion cancellation using linearly chirped Bragg grating filters in optical waveguides," *Optics Letters*, vol. 12, Oct. 1987, p. 847-849.

[41]   L. Ranzani et al., "Microwave-Domain Analog Predistortion Based on Chirped Delay Lines for Dispersion Compensation of 10-Gb/s Optical Communication Signals," *Journal of Lightwave Technology,* vol. 26, 2008, p. 2641–2646.

[42]   S. Chandrasekhar et al., "Repeaterless transmission with negative penalty over 285 km at 10 Gb/s using a chirp managed laser," *Photonics Technology Letters, IEEE*, vol. 17, 2005, p. 2454–2456.

[43]   S. Chandrasekhar et al., "Flexible transport at 10-Gb/s from 0 to 675 km (11,500 ps/nm) using a chirp-managed laser, no DCF, and a dynamically adjustable dispersion-compensating receiver," *Optical Fiber Communication Conference,. OFC 2005*, 2005.

[44]   S. Chandrasekhar et al., "Chirp-managed laser and MLSE-RX enables transmission over 1200 km at 1550 nm in a DWDM environment in NZDSF at 10 gb/s without any optical dispersion compensation," *Photonics Technology Letters*, vol. 18, Jul. 2006, p. 1560–1562.

[45]   X. Zheng et al., "Performance demonstration of 300-km dispersion uncompensated transmission using tunable chirp-managed laser and EDC integratable into small-form-factor XFP," *IEEE/LEOS Summer Topical Meetings 2008* , 2008, p. 225–226.

[46]   S. Chandrasekhar et al., "Evaluation of Chirp-Managed Lasers in a Dispersion Managed DWDM Transmission over 24 Spans," *Optical Fiber Communication Conference,. OFC 2007.* 2007, p. 1–3.

[47]   N. Henmi et al., "Prechirp technique as a linear dispersion compensation for ultrahigh-speed long-span intensity modulation directed detection optical communication systems," *Journal of Lightwave Technology,* vol. 12, 1994, p. 1706–1719.

[48]   T.L. Koch, and R. Alferness, "Dispersion Compensation by active predistorted signal synthesis," *Journal of Lightwave Technology,* vol. 3, 1985, p. 800-805.

[49]   G.P. Agrawal and N.A. Olsson, "Amplification and compression of weak picosecond optical pulses by using semiconductor-laser amplifiers," *Optics Letters,* vol. 14, May. 1989, p. 500–502.

[50]   G.P. Agrawal and M.J. Potasek, "Nonlinear pulse distortion in single-mode optical fibers at the zero-dispersion wavelength," *Physical Review A,* vol. 33, Mar. 1986, p. 1765.

[51]   K. Iwashita and N. Takachio, "Chromatic dispersion compensation in coherent optical communications," *Journal of Lightwave Technology,* vol. 8, 1990, p. 367–375.

[52]   N. Takachio and K. Iwashita, "Compensation of fibre chromatic dispersion in optical heterodyne detection," *Electronics Letters,* vol. 24, 1988, p. 108–109.

[53]   Govind P. Agrawal, "Fiber-optic communication systems", *John Wiley & Sons Inc*, 2002.

[54]   K. Iwashita and N. Takachio, "Compensation of 202 km single-mode fibre chromatic dispersion in 4 Gbit/s optical CPFSK transmission experiment," *Electronics Letters,* vol. 24, 1988, p. 759–760.

[55]   J. Winters, "Equalization in coherent lightwave systems using a fractionally-spaced equalizer," *Global Telecommunications Conference, 1990, and Exhibition. 'Communications: Connecting the Future', GLOBECOM '90., IEEE,* 1990, p. 784–788 vol.2.

[56]   Tektronix Digital Phosphor Oscilloscopes / Digital Serial Analyzers (DPO/DSA70000B) Series Data Sheet,2008,[ref num 55W-23032-3] www.tek.com [accessed 11 October 2009]

[57]   Infiniium 90000A DSO Series high-performance Windows-based oscilloscopes,2009,[ref num 5989-7819EN] www.agilent.com [accessed 11

October 2009]

[58]   T. Ellermeyer et al., "DA and AD converters for 25 GS/s and above," *IEEE/LEOS Summer Topical Meetings, 2008* , 2008, p. 117-118.

[59]   P. Schvan et al., "A 24GS/s 6b ADC in 90nm CMOS," *Solid-State Circuits Conference, 2008. ISSCC 2008.* 2008, p. 544-634.

[60]   Yuan Yao et al., "A 3-bit 20GS/s interleaved flash analog-to-digital converter in SiGe technology," *Solid-State Circuits Conference, 2007. ASSCC '07. IEEE Asian*, 2007, p. 420-423.

[61]   S. Halder et al., "A 20GS/s 8-Bit Current Steering DAC in 0.25um SiGe BiCMOS Technology," *Microwave Integrated Circuit Conference, 2008. EuMIC 2008. European*, 2008, p. 147-150.

[62]   H. Sun et al., "Real-time measurements of a 40 Gb/s coherent system," *Optics Express*, vol. 16, 2008, p. 873–879.

[63]   T. Kupfer et al., "Measurement of the Performance of 16-States MLSE Digital Equalizer with Different Optical Modulation Formats," *Optical Fiber Communication Conference,. OFC 2008*, 2008, PDP13.

[64]   P. Watts, et al. "An FPGA-Based Optical Transmitter Design Using Real-Time DSP for Advanced Signal Formats and Electronic Predistortion," *Journal of Lightwave Technology* 2007, p. 3089–3099.

[65]   K. Roberts et al., "Electronic precompensation of optical nonlinearity," *IEEE Photonics Technology Letters*, vol. 18, 2006, p. 403–405.

[66]   R.-. Essiambre and P.J. Winzer, "Fibre nonlinearities in electronically pre-distorted transmission," *European Conference on Optical Communication, ECOC 2005*, 2005, p. 191–192.

[67]   R.-. Essiambre et al., "Electronic predistortion and fiber nonlinearity," *IEEE Photonics Technology Letters*, vol. 18, Sep. 2006, p. 1804–1806.

[68]   G. Goldfarb and Guifang Li, "Chromatic Dispersion Compensation Using Digital IIR Filtering With Coherent Detection," *Photonics Technology Letters, IEEE*, vol. 19, 2007, p. 969-971.

[69]   G. Goldfarb and G. Li, "Dispersion Compensation of up to 25,200ps/nm Using IIR Filtering," *Optical Fiber Communication Conference, OFC 2008.*, 2008, p. 1–3.

[70]   T. Kupfer et al., "Digital equalisation at 10.7Gb/s using maximum likelihood sequence estimation- a present and future technology," *Optical Fibre Communications and Electronic Signal Processing, 2005. The IEE Seminar on* , London: 2005, p. 20–5.

[71]   H. Bae et al.,"An MLSE receiver for electronic-dispersion compensation of OC-192 fiber links," *Solid-State Circuits Conference, 2006. ISSCC 2006. Digest of Technical Papers. IEEE International*, 2006, p. 874–883.

[72]   A. Napoli et al.,"Limits of Maximum-Likelihood Sequence Estimation in Chromatic Dispersion Limited Systems," *Optical Fiber Communication Conference,. OFC 2006*, 2006, JthB36.

[73]   S.J. Savory et al., "IMDD Transmission over 1,040 km of Standard Single-Mode Fiber at 10Gbit/s Using a One-Sample-per-Bit Reduced-Complexity MLSE Receiver," *Optical Fiber Communication Conference,. OFC 2007*, 2007, OthK2.

[74]   G. Bosco and P. Poggiolini, "Long-distance effectiveness of MLSE IMDD receivers," *Photonics Technology Letters, IEEE*, vol. 18, 2006, p. 1037-1039.

[75]   A.F. Elrefaie et al., "Chromatic dispersion limitations in coherent optical fibre transmission systems," *Electronics Letters*, vol. 23, Jul. 1987, p. 756–758.

[76]   A.F. Elrefaie et al., "Chromatic dispersion limitations in coherent lightwave transmission systems," *Journal of Lightwave Technology*, vol. 6, May. 1988, p. 704–709.

[77]   M.G. Taylor, "Coherent detection method using DSP for demodulation of signal and subsequent equalization of propagation impairments," *Photonics Technology Letters, IEEE*, vol. 16, 2004, p. 674-676.

[78]   D. Ly-Gagnon et al., "Unrepeatered optical transmission of 20 Gbit/s quadrature phase-shift keying signals over 210 km using homodyne phase-diversity receiver and digital signal processing," *Electronics Letters*, vol. 41, 2005, p. 206–207.

[79]   N. Kikuchi et al., "Proposal and First Experimental Demonstration of Digital Incoherent Optical Field Detector for Chromatic Dispersion Compensation," *European Conference on Optical Communication, ECOC 2006*, 2006.

[80]   J. Savory, "Digital Equalisation of 40Gbit/s per Wavelength Transmission

over 2480km of Standard Fibre without Optical Dispersion Compensation," *European Conference on Optical Communication, ECOC 2006*,2006.

[81] S.J. Savory, "Optimum electronic dispersion compensation strategies for nonlinear transmission," *Electronics Letters*, vol. 42, Mar. 2006, p. 407–408.

[82] C. Laperle et al., "Wavelength Division Multiplexing (WDM) and Polarizationpolarisation Mode Dispersion (PMD) Performance of a Coherent 40Gbit/s Dual-Polarization Quadrature Phase Shift Keying (DP-QPSK) Transceiver," *Optical Fiber Communication Conference,. OFC 2007*, 2007, PDP16.

[83] A. Leven et al., "Coherent Receivers for Practical Optical Communication Systems," *Optical Fiber Communication Conference,. OFC 2007*, 2007, OthK4.

[84] K. Roberts, "Electronic Dispersion Compensation Beyond 10 Gb/s," *IEEE/LEOS Summer Topical Meetings, 2007*, 2007, p. 9–10.

[85] S.J. Savory et al., "Transmission of 42.8Gbit/s Polarization Multiplexed NRZ-QPSK over 6400km of Standard Fiber with no Optical Dispersion Compensation," *Optical Fiber Communication Conference,. OFC 2007*, 2007, OtuA1.

[86] M.G. Taylor, "Coherent Detection for Optical Communications using Digital Signal Processing," *Optical Fiber Communication Conference,. OFC 2007.* 2007, p. 1–3.

[87] S.J. Savory et al., "Electronic compensation of chromatic dispersion using a digital coherent receiver," *Optics Express*, vol. 15, Mar. 2007, p. 2120-2126.

[88] S. Bigo, "Coherent Detection : A Key Enabler for Next-Generation Optical Transmission Systems ?," *Transparent Optical Networks, 2007. ICTON '07. 9th International Conference on*, 2007, p. 332–335.

[89] G. Charlet et al., "Transmission of 81 channels at 40Gbit/s over a transpacific-distance erbium-only link, using PDM-BPSK modulation, coherent detection, and a new large effective area fibre.," *European Conference on Optical Communication, ECOC 2008*, 2008, p. 1-2

[90] C. Fludger et al., "Coherent Equalization and POLMUX-RZ-DQPSK for Robust 100-GE Transmission," *Journal of Lightwave Technology*, vol. 26,

2008, p. 64–72.

[91]   E. Ip et al., "Coherent detection in optical fiber systems," *Optics Express*, vol. 16, 2008, p. 753–791.

[92]   K. Kikuchi, "Coherent optical communications —History, state-of-the-art technologies, and challenges for the future," *Opto-Electronics and Communications Conference, 2008 and the 2008 Australian Conference on Optical Fibre Technology. OECC/ACOFT 2008. Joint conference of the*, 2008, p. 1–4.

[93]   S.J. Savory, "Digital filters for coherent optical receivers," *Opt. Express*, vol. 16, 2008, p. 804–817.

[94]   C. Wree et al., "Repeaterless 10.7-Gb/s DPSK Transmission Over 304 km of SSMF Using a Coherent Receiver and Electronic Dispersion Compensation," *IEEE Photonics Technology Letters*, vol. 20, 2008, p. 407–409.

[95]   P. Poggiolini et al., "Evaluation of the computational effort for chromatic dispersion compensation in coherent optical PM-OFDM and PM-QAM systems," *Optics Express*, vol. 17, 2009, p. 1385-1403.

[96]   G. Charlet, "Coherent detection associated with digital signal processing for fiber optics communication," *Comptes Rendus Physique*, vol. 9, 2008, p. 1012-1030.

[97]   J.C. Palais "Fibre Optical Communications",*Pearson Edication,* 5ed, 2004

[98]   J Senior "Optical Fibre Communications: Principles and Practice (Prentice Hall International series in optoelectronics)" *Prentice Hall*, 2ed, 1992

[99]   D Walshe et al "Practical Bit Error Rate Measurements on Fibre Optic Communications Links in Student Teaching Laboratories," ETOP 2005. http://spie.org/etop/ETOP2005_021.pdf, 2005

[100]   B. Wedding and B. Franz, "Unregenerated optical transmission at 10 Gbit/s via 204 km of standard singlemode fibre using a directly modulated laser diode," *Electronics Letters*, vol. 29, 1993, p. 402–404.

[101]   B. Wedding et al., "Repeaterless optical transmission at 10 Gbit/s via 182 km of standard singlemode fibre using a high power booster amplifier," *Electronics Letters*, vol. 29, 1993, p. 1498–1500.

[102]   A. Price et al., "210 km repeaterless 10 Gb/s transmission experiment through

nondispersion-shifted fiber using partial response scheme," *Photonics Technology Letters, IEEE*, vol. 7, 1995, p. 1219–1221.

[103] G. Agrawal, "Nonlinear fiber optics", *Elsevier/Academic Press*, 2007.

[104] R. Essiambre, "Capacity Limits of Fiber Optic Communication Systems," *European Conference on Optical Communication, ECOC 2008*, 2008.

[105] J. Proakis, *Digital signal processing : principles, algorithms, and applications*, Upper Saddle River N.J.: Prentice Hall, 1996.

[106] M. Jeruchim, "Techniques for Estimating the Bit Error Rate in the Simulation of Digital Communication Systems," *Selected Areas in Communications, IEEE Journal on*, vol. 2, 1984, p. 153-170.

[107] F. Devaux et al., "Simple measurement of fiber dispersion and of chirp parameter of intensity modulated light emitter," *Journal of Lightwave Technology*, vol. 11, 1993, p. 1937-1940.

[108] C. Incorporated, *Corning SMF-28e Optical Fiber Product Information*, http://www.corning.com/assets/0/433/573/583/09573389-147D-4CBC-B55F-18C817D5F800.pdf 2008.

[109] N. Olsson, "15,000 km fibre-optic transmission using a linear repeater," *Electronics Letters*, vol. 23, 1987, p. 659–660.

[110] D. Malyon et al., "Demonstration of optical pulse propagation over 10000 km of fibre using recirculating loop," *Electronics Letters*, vol. 27, 1991, p. 120–121.

[111] N. Bergano and C. Davidson, "Circulating loop transmission experiments for the study of long-haul transmission systems using erbium-doped fiber amplifiers," *Journal of Lightwave Technology*, vol. 13, 1995, p. 879–888.

[112] D. Malyon, et al., "Assessment of the polarisation loss dependence of transoceanic systems using a recirculating loop," *Electronics Letters*, vol. 29, 1993, p. 207–208.

[113] C. Mazzali and H. Fragnito, "Recirculating loop for experimental evaluation of EDFA saturated regime effects on optical communication systems," *Microwave Theory and Techniques, IEEE Transactions on*, vol. 46, 1998, p. 253–257.

[114] Q. Yu et al., "Loop-Synchronous Polarization Scrambling Technique for

Simulating Polarization Effects Using Recirculating Fiber Loops," *Journal of Lightwave Technology,* vol. 21, 2003, p. 1593.

[115] S. Walklin and J. Conradi, "Multilevel Signaling for Increasing the Reach of 10 Gb/s Lightwave Systems," *Journal of Lightwave Technology,* vol. 17, 1999, p. 2235.

[116] J.D. Bull et al. "40 Ghz Electro-optic Polarization Modulator for Fiber Optic Communications Systems", *SPIE Photonics North*, 2004.

[117] S. Ramachandran, "Fiber based dispersion compensation", *New York: Springer,* 2007.

[118] P. Winzer et al., "40-Gb/s return-to-zero alternate-mark-inversion (RZ-AMI) transmission over 2000 km," *Photonics Technology Letters, IEEE,* vol. 15, 2003, p. 766–768.

[119] O.E. Agazzi et al., "Maximum-Likelihood Sequence Estimation in Dispersive Optical Channels," *Journal of Lightwave Technology,* vol. 23, 2005, p. 749.

[120] G. Forney, "Maximum-likelihood sequence estimation of digital sequences in the presence of intersymbol interference," *Information Theory, IEEE Transactions on,* vol. 18, 1972, p. 363-378.

[121] G. Forney, "The Viterbi algorithm," *Proceedings of the IEEE,* vol. 61, 1973, p. 268-278.

[122] B. Sklar, "How I learned to love the trellis," *Signal Processing Magazine, IEEE,* vol. 20, 2003, p. 87–102.

[123] A. Viterbi, "Error bounds for convolutional codes and an asymptotically optimum decoding algorithm," *Information Theory, IEEE Transactions on,* vol. 13, 1967, p. 260–269.

[124] A. Viterbi, "Convolutional Codes and Their Performance in Communication Systems," *Communication Technology, IEEE Transactions on,* vol. 19, 1971, p. 751–772.

[125] J. Hayes, "The Viterbi algorithm applied to digital data transmission," *Communications Society: A Digest of News and Events of Interest to Communications Engineers,* vol. 13, 1975, p. 15–20.

[126] J.G. Proakis, *Digital communications*, McGraw-Hill, New York :, 1989.

[127] J. Heller and I. Jacobs, "Viterbi Decoding for Satellite and Space

Communication," *Communication Technology, IEEE Transactions on*, vol. 19, 1971, p. 835–848.

[128] A. Viterbi et al., "A pragmatic approach to trellis-coded modulation," *Communications Magazine, IEEE*, vol. 27, 1989, p. 11–19.

[129] R.I. Killey et al., "Electronic Dispersion Compensation by Signal Predistortion," *Optical Fiber Communication Conference,. OFC 2006*, 2006, p. OWB3.

[130] P. Watts et al., "Techniques for long haul transmission without optical dispersion compensation," *2005. The IEE Seminar on Optical Fibre Communications and Electronic Signal Processing*, 2005, p. 24–7.

[131] S. Savory, "Digital Signal Processing Options in Long Haul Transmission," *Optical Fiber Communication Conference,. OFC 2008*, 2008, p. 1–3.

[132] M. Taylor, "Coherent detection method using DSP for demodulation of signal and subsequent equalization of propagation impairments," *Photonics Technology Letters, IEEE*, vol. 16, 2004, p. 674–676.

[133] K. Kikuchi and S. Tsukamoto, "Evaluation of Sensitivity of the Digital Coherent Receiver," *Journal of Lightwave Technology*, vol. 26, 2008, p. 1817–1822

[134] A.J. Faebert, "Performance of 10.7 Gb/s receiver with digital Equaliser using Maximum-Likelihood Sequence Estimation," *European Conference on Optical Communication, ECOC 2004,2004,*PD Th4-1-5

[135] T. Kupfer et al.,"Digital equalisation at 10.7Gb/s using maximum likelihood sequence estimation- a present and future technology," *Optical Fibre Communications and Electronic Signal Processing, 2005. The IEE Seminar on* , 2005, p. 0_20–5/12.

[136] S. Savory et al.,"Robust optical systems using maximum likelihood sequence estimators," *Optical Fibre Communications and Electronic Signal Processing, 2005. The IEE Seminar on* , 2005, p. 0_33–11/10.

[137] H. Bae et al., "An MLSE Receiver for Electronic Dispersion Compensation of OC-192 Fiber Links," *Solid-State Circuits, IEEE Journal of*, vol. 41, 2006, p. 2541–2554.

[138] G. Bosco et al., "Optimization of Branch Metric Exponent and Quantization

Range in MLSE Receivers for Duobinary Systems," *Photonics Technology Letters, IEEE*, vol. 20, 2008, p. 924–926.

[139] P. Watts et al., "Performance of single-mode fiber links using electronic feed-forward and decision feedback equalizers," *Photonics Technology Letters*, vol. 17, 2005, p. 2206–2208.